Fall 12-16-2021

Intracavity Phase Interferometry Based Fiber Sensors

Luke Jameson Horstman
University of New Mexico - Main Campus

Luke Jameson Horstman

Candidate

Optical Science and Engineering

Department of Physics and Astronomy, The University of New Mexico

This dissertation is approved, and it is acceptable in quality and form for publication:

Approved by the Dissertation Committee:

Dr. Jean-Claude M. Diels, Chair

Dr. Tara Drake

Dr. Steven R.J. Brueck

Dr. R. Jason Jones

Intracavity Phase Interferometry Based Fiber Sensors

by

Luke Jameson Horstman

B.S., Bethel University, 2016
M.S., University of New Mexico, 2018

DISSERTATION

Submitted in Partial Fulfillment of the
Requirements for the Degree of

Doctor of Philosophy
Optical Science and Engineering

The University of New Mexico

Albuquerque, New Mexico

May 2022

https://orcid.org/0000-0002-0649-3235

Dedication

For my wife, Rachel, who stood by my side as I struggled with the mental illness that is a physics addiction. May I support you in the future as you have supported me. These words are for you.

Acknowledgments

No accomplishment is the product of a sole actor. Hard work and willpower alone are not sufficient for success; there is always a bit of luck required. But, I have been lucky enough to be surrounded by wonderful colleagues, mentors, friends, and family. Without these incredible people, the following pages would not have been possible.

First, many thanks to my academic advisor Dr. Jean-Claude Diels for teaching me how to be a true scientific thinker. I am honored to join the extensive community of your graduates and hope to one day make you as proud to be my mentor as I am to be your mentee. Shout out to my Midwestern companion Max Aiello. Through hot wings, board games, ping pong, and golf – somehow we maintained together. Good friends are the only way through. Thanks to my colleagues Ali, Ning, Hanieh, and James who struggled in the trenches with me and who gave me invaluable guidance during my first years. To the man pulling the strings, Dr. Chad Hoyt, who lured me into optics, aided my acceptance into grad school, and then got me a job: I will be forever grateful to you.

I owe a special thanks to my in-laws, Fred and Mavis Flemig. As frequent visitors, they not only kept Rachel in high spirits but always seemed to show up at the opportune moment to whisk us away on a trip. Without your support (financial, and emotional) I never would have kept my sanity. Special recognition goes to my editor-in-chief behind the scenes, Fred. I have always appreciated your genuine interest in the abstract topics I have explored. You would have made a great scientist. My deepest thanks to Mavis, who kept me fed and my house clean as I neglected basic bodily functions. She is, as I type this, vacuuming my house. Many thanks to the rest of the Flemigs - David, Ernie, Alison, and Cara - for their love and support.

To my wonderful parents, Joey and Leah Horstman: You instilled in me a work ethic and curiosity which drove me to science. You taught me to believe in myself and convinced me that grad school was an achievable goal. Few are as lucky as I am to have such wonderful parents. Gabe and Ben, it's a gift that I get to call you brothers and best friends. New Mexico wouldn't have been as fun, nor physics as satisfying, without the adventures and conversations we shared. A constant motivation is the feeling of impressing my brothers. I can't wait to see what the future holds for us.

To my friend, travel buddy, and partner, Rachel: You took my desire to move across the country to pursue a dream with excitement and intrigue. Without your constant love and support, I never would have stuck it out. What an adventure we have had. I must also acknowledge my unborn baby boy, who I can't wait to soon meet! Know that you were the final spark that I needed to push me through.

Thanks to the numerous others who I haven't listed, but who have nonetheless contributed to this moment. *This achievement is not mine but ours.*

Intracavity Phase Interferometry Based Fiber Sensors

by

Luke Jameson Horstman

B.S., Bethel University, 2016
M.S., University of New Mexico, 2018

Ph.D., Optical Science and Engineering, University of New Mexico, 2022

Abstract

Intracavity Phase Interferometry (IPI) is a detection technique that exploits the inherent sensitivity of a laser's frequency to the parameters of its cavity. Intracavity interferometry is orders of magnitude more sensitive than its extracavity alternatives. This dissertation improves on previous free-space proof-of-concept designs. By implementing the technique in fiber optics, using optical parametric oscillation, and investigating non-Hermitian quantum mechanics and dispersion tailoring enhancement techniques, IPI has become more applicable and sensitive.

Ring and linear IPI configurations were realized in this work, both operating as bidirectional fiber optical parametric oscillators. The benefit of using externally pumped synchronous optical parametric oscillation is the removal of the sensor dead band region and simplification of the sensing cavity. These two lasers, along with the theoretical work found in this Dissertation, will facilitate future fundamental studies of sensor noise and sensitivity enhancement.

Contents

List of Figures

List of Symbols

Presented in the order of appearance.

τ_{rt}	Round-trip time
$\mathcal{F}$	Fourier Transform
f_0	Carrier-envelope-offset frequency
ν_{rep}	Repetition frequency
ϕ_p	Pulse to pulse phase shift
E_{tr}	Train of gaussian pulses
$\tilde{\mathcal{E}}(t)$	Complex Electric field amplitude
t_g	Gaussian width
$\mathrm{III}(t)$	Shah or comb function
$\delta()$	Delta function
$\mathcal{F}\{\}$	Fourier transform
ω	Central optical frequency (angular)
Ω	Fourier transform variable (angular frequency)
$\circledast$	Convolution
c	Speed of light
n	Index of refraction
ρ_f	Free electric charge
J_f	Free electric current
D	Electric auxiliary displacement field
B	Magnetic field

H	Magnetic auxiliary field
∇	Del or Nabla operator (vector differential operator)
μ	Magnetic permeability (μ_0 vacuum permeability)
ϵ	Electric permittivity (ϵ_0 of free space)
P	Material polarization density (P_{NL} nonlinear; P_L linear)
χ	Electric susceptibility (χ_m magnetic; χ_r real; χ_i imaginary)
k	Wavenumber of propagation constant
β	Effective propagation constant
v	Light velocity (v_p phase; v_g group)
$\tilde{\mathcal{A}}$	Complex electric field amplitude
α	Saturable gain ($\hat{\alpha}$ small signal; α_L linear loss)
$\tilde{\kappa}$	Conservative coupling
s	Non-conservative coupling
Δ	Frequency detuning
D_b	Beat signal
$\tilde{\psi}$	Complex electric field amplitude
ω_a	Average frequency
W_s	Saturation energy density
$\Delta\phi$	Angular round-trip phase detuning
W_i	Pulse energy
τ_p	Phase round-trip time
$\otimes$	Cross-correlation

List of Acronyms

Presented in the order of appearance.

IPI	Intracavity Phase Interferometry
cw	Continuous Wave
CEO	Carrier Envelope Offset
FT	Fourier Transform
CME	Coupled-Mode Equation
GVD	Group Velcity Dispersion
FP	Fabry-Perot
OPO	Optical Parametric Oscillation
Yb:YAG	Ytterbium-doped Yttrium Aluminum Garnet
BiFOPO	Bidirectional Fiber Optical Parametric Oscillator
PM	Polarization Maintaining
PANDA	PANDA polarization rods
WDM	Wavelength Division Multiplexor
PCF	Photonic Crystal Fiber
HNLF	Highly Nonlinear Fiber
FC/APC	A specific type of fiber connector i.e. angled FC/PC
ISO	Isolator
CNT	Carbon nanotubes
FWHM	Full Width Half Max
PBS	Polarizing Beam Splitter

EP	Exceptional Point
PT	Parity-Time
NHQM	Non-Hermitian Quantum Mechanics
DP	Diabolical Point
GA	Genetic Algorithm
DEGA	Differential Evolution Genetic Algorithm
CaNIS	Cascaded Nonlinearity Inside a Spectrometer
MC	Mutation Chromosome
Ti:Sapph	Titanium-dope Sapphire
Nd:YAG	Neodymium-doped Yttrium Aluminum Garnet
HeNe	Helium Neon

Chapter 1

Introduction

The work covered in this thesis has been carried out during historic times that included 2 laboratory moves, a pandemic, and nationwide riots. Despite these worldwide and local challenges I am happy to present the following representation of my work as a researcher working under the direction of Dr. Jean-Claude Diels. My time in the group began as that of a utility researcher. I aided my colleagues on projects of filamentation, titanium-sapphire laser development, Ultrafast metrology, software development, and data analysis. The majority of that work has been documented elsewhere [2–5]. This dissertation will focus on the work I completed, largely, alone.

The research summarized here revolves around the ultrafast metrological method termed "Intracavity Phase Interferometry" (IPI). This method is an active interferometry method that uses a single cavity for common noise rejection. Additionally, by using pulses instead of continuous wave (cw) fields, the frequency locking caused dead band is eliminated. This thesis starts with a general overview of frequency combs in chapter 2. While the topic of frequency combs is not new, it is imperative to the understanding of IPI and will be developed in a fairly novel way. Chapter 3 introduces the measurement technique and gives it a solid theoretical foundation, while chapter 4 outlines the experimental realization of the technique as a bidirectional fiber optic parametric oscillator. Chapter 5 reviews the theoretical work that was completed surrounding sensitivity enhancement of IPI. Finally, chapter 6 discusses a Genetic

Algorithm that was developed as a software resource.

The scientific advancements represented by this dissertation can be broken into three categories: experimental, theoretical, and numerical. Experimentally, IPI was successfully realized in fiber using optical parametric oscillation in both ring and linear configurations. Theoretically, IPI was analyzed in a novel way that allowed consideration of sensor enhancement. The lasers and corresponding theory that has been developed will facilitate future studies of IPI enhancement that include quantum squeezing and intracavity dispersion tailoring. There are also fundamental questions of laser noise and instability that are developed in the theoretical sections that the experimental apparatuses are primed to explore. Finally, the software tools developed throughout this work including the genetic algorithm, frequency comb simulations, and noise analysis, will be invaluable to future studies.

Chapter 2

Frequency Combs

2.1 Introduction

In order to fully understand the method of Intracavity Phase Interferometry (IPI), the optical phenomenon of frequency combs must be well understood. Thus, a proper introduction is required. It should be noted that a frequency comb is a special form of pulsed lasing that involves the interference of laser modes and therefore has unique characteristics. There are other forms of pulsed lasing, such as Q-switching, that operate under different principles and therefore do not share the same properties or derivations described here.

A frequency comb, as the name implies, is an optical signal which has equally spaced frequency components (like the teeth of a hair comb). One of the important characteristics of such a comb is that these frequency teeth are **rigorously** equally spaced so that they can be used as a very precise ruler in frequency space [6]. The qth frequency tooth of a comb with a round trip time of τ_{rt} can be expressed as,

$$\nu_q = f_0 + q\nu_{rep}, \tag{2.1}$$

where $f_0 = \phi_p/2\pi\tau_{rt}$ is known as the carrier-to-envelope offset (CEO) frequency and can be interpreted as the offset from zero of the first frequency tooth of the virtual extended comb. Note that ϕ_p is the pulse to pulse phase shift which will be described

in detail in section 2.3. Each subsequent tooth, q, is separated by a distance (in frequency space) defined by the repetition rate $\nu_{rep} = 1/\tau_{rt}$.

To create such a signal in frequency a repetitive series of light pulses in time, termed a pulse train, must be made. A simple method to show this relationship mathematically is to first create a train of Gaussian pulses in time, $E_{tr}(t)$, by convoluting a Gaussian pulse, $\tilde{\mathcal{E}}(t) = e^{-(t/t_g)^2}$, with the Shah (comb) function, $\mathrm{III}(t) = \sum_{n=-\infty}^{\infty} \delta(t - n/\nu_{rep})$ [7, 8], such that,

$$E_{tr}(t) = \tilde{\mathcal{E}}(t) \circledast \mathrm{III}(t). \tag{2.2}$$

The Gaussian width parameter, t_g, is related to the full width half max by $2\sqrt{\ln(2)}t_g = t_{1/2}$. To observe this pulse train in the frequency domain, the Fourier transform (FT), $\mathcal{F}\{\}$, is taken:

$$E_{tr}(\Omega) = \mathcal{F}\{E_{tr}(t)\}. \tag{2.3}$$

The convolution property states that the FT of a convolution is equivalent to the multiplication of the FTs of each individual distribution,

$$\mathcal{F}\{E_{tr}(t)\} = \mathcal{F}\{\tilde{\mathcal{E}}(t) \circledast \mathrm{III}(t)\} = \mathcal{F}\{\tilde{\mathcal{E}}(t)\} \cdot \mathcal{F}\{\mathrm{III}(t)\} = \tilde{\mathcal{E}}(\Omega) \cdot \mathrm{III}(\Omega). \tag{2.4}$$

Since the FT of a Gaussian is just another Gaussian and the FT of the Shah function is another Shah function, it is easy to see that Eq. (2.4) describes a comb of delta functions that are modulated by a Gaussian envelope. While this method easily displays how a pulse train leads to a frequency comb, it hides a lot of the important specifics. In particular, it gives no insight into what defines the width of each frequency tooth.

2.2 From a pulse to a comb

A more rigorous approach involves doing away with the Shah function and building up the pulse train from scratch. A single Gaussian pulse with a center carrier frequency,

ω, can be written $\tilde{E}(t) = \tilde{\mathcal{E}}(t)e^{i\omega t}$. Where $\tilde{\mathcal{E}}(t) = e^{-(t/t_g)^2}$ is the same Gaussian amplitude described previously. The pulse train is then expressed as a sum,

$$E_{tr}(t) = \sum_{q=0}^{p} \tilde{\mathcal{E}}(t - q\tau_{rt})e^{i\omega(t-q\tau_{rt})}. \tag{2.5}$$

This is a train of p identical pulses that are separated in time by τ_{rt}. To calculate the FT, the convolution theory is invoked again but in reverse (from product to convolution),

$$E_{tr}(\Omega) = \mathcal{F}\{E_{tr}(t)\} = \mathcal{F}\left\{e^{i\omega t}\sum_{q=0}^{p} \tilde{\mathcal{E}}(t - q\tau_{rt})e^{-iq\omega\tau_{rt}}\right\} \tag{2.6}$$

$$= \mathcal{F}\{e^{i\omega t}\} \circledast \mathcal{F}\left\{\sum_{q=0}^{p} \tilde{\mathcal{E}}(t - q\tau_{rt})e^{-iq\omega\tau_{rt}}\right\}. \tag{2.7}$$

The sum rule of integration allows the FT integral to be applied individually to each summation component such that,

$$E_{tr}(\Omega) = \delta(\Omega - \omega) \circledast \sum_{q=0}^{p} e^{-iq\omega\tau_{rt}}\mathcal{F}\left\{\tilde{\mathcal{E}}(t - q\tau_{rt})\right\}. \tag{2.8}$$

The FT can be solved analytically by completing the square in the exponent and carrying out a Gaussian integral. The result is,

$$E_{tr}(\Omega) = \delta(\Omega - \omega) \circledast t_g\sqrt{\pi}e^{-\left(\frac{t_g\Omega}{2}\right)^2}\sum_{q=0}^{p} e^{-iq\tau_{rt}(\Omega-\omega)}. \tag{2.9}$$

Applying the sifting property of the convolution leads to the pulse train taking the form [1],

$$E_{tr}(\Omega) = t_g\sqrt{\pi}e^{-\left(\frac{t_g(\Omega-\omega)}{2}\right)^2}\sum_{q=0}^{p} e^{-iq\tau_{rt}(\Omega-2\omega)}. \tag{2.10}$$

The sum can be simplified with a finite geometric series so that,

$$E_{tr}(\Omega) = \left[t_g\sqrt{\pi}e^{-\left(\frac{t_g(\Omega-\omega)}{2}\right)^2}\right]\frac{1 - \left[e^{-i\tau_{rt}(\Omega-2\omega)}\right]^{p+1}}{1 - e^{-i\tau_{rt}(\Omega-2\omega)}}. \tag{2.11}$$

[1] The convolution is commutative so Eq. (2.9) can be written as, $f(\Omega) \circledast \delta(\Omega - \omega) = \int f(\tau)\delta(\Omega - \omega - \tau)\partial\tau = f(\Omega - \omega)$, such that the delta function convolution is replaced with the variable substitution of $\Omega \to \Omega - \omega$, where, $f(\Omega) = t_g\sqrt{\pi}e^{-\left(\frac{t_g\Omega}{2}\right)^2}\sum_{q=0}^{p} e^{-iq\tau_{rt}(\Omega-\omega)}$.

As can be seen in the numerical evaluation of Eq. (2.11) displayed in Fig. 2.1, this expression describes a series of pulses with widths that are inversely related to the length of the sum p. This series of frequency pulses is modulated by a Gaussian envelope centered at ω with a width of $2/t_g$. This approach shows explicitly that

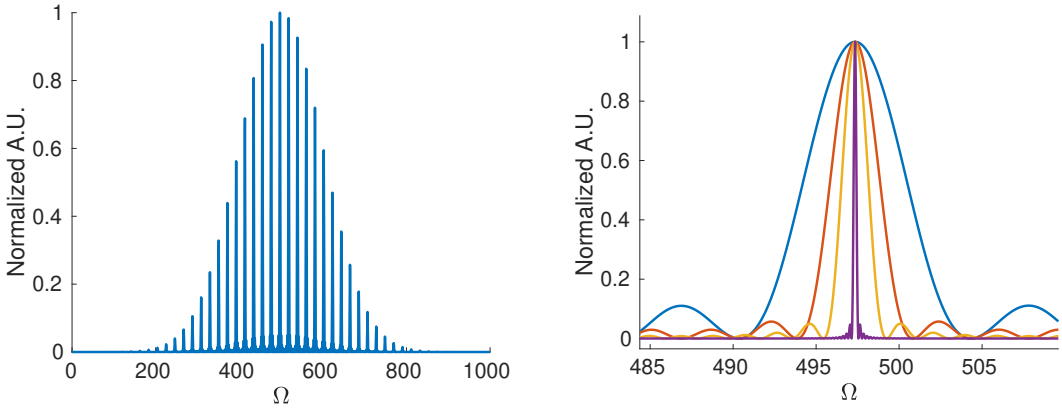

Figure 2.1: Left: Plot of a frequency comb using Eq. 2.11 with $t_g = 0.01$, $\omega = 500$, $\tau_{rt} = 0.3$, and $p = 10$. Right: Plot of a single frequency tooth using the same parameters, but with different numbers of round-trips: $p = 2$(blue), $p = 5$(orange), $p = 10$(yellow), $p = 100$(purple).

the frequency bandwidth is inversely proportional to the pulse width in time, the frequency tooth spacing is inversely proportional to the round-trip time, and the width of each frequency tooth is inversely proportional to the length of the pulse train, which is typically set by the coherence length of the laser.

Even this approach, however, is not rigorously correct in terms of a true laser system. In fact, most of the nuances have been hidden away by describing the pulse train in the form of Eq. (2.5). To explain this we need to think more explicitly about how a laser creates a circulating pulse in its cavity.

2.3 Including dispersion

A laser cavity has a specific number of longitudinal modes that are allowed to oscillate according to the resonant condition, $\omega_q = 2\pi qc/nL$, where q is an integer which has a

range defined by the gain bandwidth, c is the speed of light and nL is the optical path length (index of refraction, n, multiplied by the cavity length, L). In order to create a pulse in time, all of these oscillating modes need to have a fixed phase relationship such that they constructively interfere in one location and deconstructively interfere everywhere else. This is known as mode-locking. If the index of refraction is the same for all frequencies then each longitudinal mode and the resultant pulse propagate together i.e. the group (pulse) and phase (longitudinal mode) velocities are equal. This is not generally the case in a physical laser. In a typical laser, the index of refraction (and therefore the optical path length) is dependent on frequency. This is known as dispersion. What this means is not only does the pulse envelope walk-off from the underlying frequency phases, but the longitudinal modes are no longer equally spaced. There is a contradiction here. In order to have a pulse train, one needs a comb of equally spaced frequency modes, and I have just explained that in a real laser the allowed longitudinal modes do not follow this restriction. But, it has been experimentally proven that pulse trains and frequency combs exist. It turns out that a complicated dance between dispersion and nonlinear effects occurs within the gain and mode-locking elements to maintain a single coherent optical pulse, known as a soliton [6, 9].

Instead of trying to describe all of the complicated dynamics involved, let's work backwards from the experimental fact that a frequency comb exists. Ideally the spectral domain is described by Eq. (2.1), which converting to angular frequency leads to,

$$\omega_q = 2\pi f_0 + 2\pi q/\tau_{rt}, \tag{2.12}$$

Again, these are **resultant** frequency modes that have no relation to the cold cavity longitudinal modes. The phase picked up by each mode at every round-trip is then,

$$\omega_q \tau_{rt} = 2\pi \tau_{rt} f_0 + 2\pi q. \tag{2.13}$$

This means that at every round-trip the underlying modes slip from the pulse envelope by an amount of,

$$\phi_p = 2\pi \tau_{rt} f_0. \tag{2.14}$$

This also means we need to update the pulse train Eq. (2.5) to reflect the phase slippage,

$$E_{tr}(t) = \sum_{q=0}^{p} \tilde{\mathcal{E}}(t - q\tau_{rt}) e^{i(\omega t - q\phi_p)}. \tag{2.15}$$

This represents an underlying central frequency mode, ω, that is regularly sampled with a Gaussian envelope such that the underlying mode slips from the peak of the envelope by an amount, ϕ_p, each pulse. This is why f_0 has been termed the carrier-to-envelope offset frequency. This phase slippage can also be interpreted as caused by the difference between the average phase and group velocity. To see this let's rearrange Eq. (2.12) to be,

$$f_0 = \frac{\omega_q}{2\pi} - \frac{q}{\tau_{rt}}. \tag{2.16}$$

The propagating pulse by definition reconstructs itself every round trip so that the average group velocity is defined as,

$$v_g = L/\tau_{rt}. \tag{2.17}$$

It is again important to emphasize that this group velocity is not the textbook $\partial\Omega/\partial k$ quantity, but an effective velocity governed by nonlinear cavity effects. The phase velocity is defined as $v_p = \lambda\nu$ [2], where $2\pi\nu = \omega$. The qth resonant mode of a cavity has a wavelength of $\lambda_q = L/q$, so that the phase velocity becomes,

$$v_p = L\omega_q/2\pi q. \tag{2.18}$$

Rearranging clearly shows the relationship between the CEO and dispersion:

$$f_0 = \frac{\omega_q}{2\pi} - \frac{q}{\tau_{rt}} = \frac{q}{L}\left(v_p - v_g\right). \tag{2.19}$$

Note that this definition is solely for demonstration purposes as it depends on which mode is chosen to calculate the phase velocity, while Eq. (2.14) is independent of this choice. Nonetheless, Eq. (2.19) clearly shows that the CEO frequency is sensitive to changes in the phase velocity of light. As will be explained in the next chapter, It is this sensitivity on which the method of IPI is based.

[2] This λ is the wavelength in the material. In other words, if λ_0 is the vacuum wavelength, then $\lambda = \lambda_0/n_p$, where n_p is the average phase index.

Chapter 3

Intracavity Phase Interferometry: Theoretical Background

3.1 Introduction

Intracavity Phase Interferometry (IPI) is a sensing technique that involves implementing an interferometer inside of a laser cavity. Thorough descriptions and theoretical analysis of the technique have been carried out previously [10], so only a brief description will be given here. Most measurement techniques use the laser as a black box and simply use the output radiation to investigate some external phemonenon. By placing the measurement inside of the laser cavity itself, the sensitivity can be increased by orders of magnitude. Instead of reading the measurement out as an amplitude fringe that is vulnerable to environmental noise, IPI interference occurs inside of the laser cavity which is realized as a frequency shift that can be read out as a beat frequency.

To implement IPI, there must be two counter-propagating electric fields lasing inside of a single cavity. One field is affected by the natural phenomenon to be investigated while the other serves as a reference. Because the two fields observe different optical paths, they will have slightly different lasing frequencies. By extracting each

field from the cavity and interfering them on an external detector (the fields must have the same repetition rate), their frequency difference can be observed as a beat frequency.

Due to coupling based injection locking, a laser has difficultly sustaining two continuous-wave (cw) lasing fields that are slightly detuned from one another [11–13]. To avoid this difficulty, pulsed electric fields are used in place of cw. The method can then be understood in the framework of frequency combs.

Two counter-propagating pulses of light can be represented in the frequency domain as two frequency combs. Because they are propagating in the same cavity, they have correlated noise and when no measurement is taking place each frequency comb is identical. When the phenomenon to be measured is introduced into the cavity such that it only affects one of the pulses, that frequency comb's CEO frequency is shifted causing the measurement to become the interference of two shifted (but same repetition rate) frequency combs (see Fig. 3.1). The beat frequency can then be

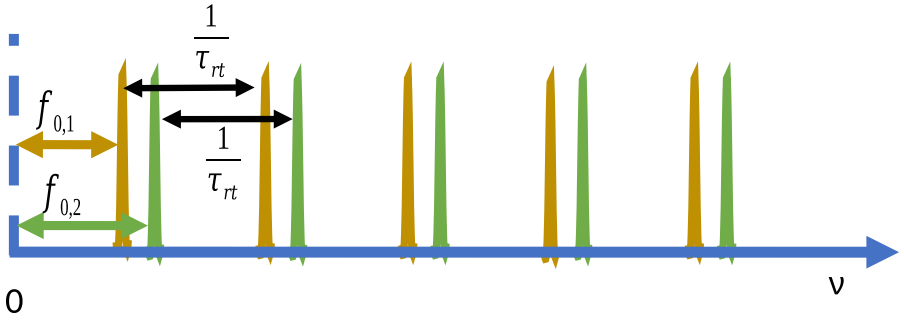

Figure 3.1: An intracavity differential phase shift between two lasing pulses causes their CEO frequencies, $f_{0,1}$ and $f_{0,2}$, to be slightly shifted from each other. Nonlinear effects within the cavity leaves their repetition rates, $\nu_{rep} = 1/\tau_{rt}$, unchanged such that interfering the pulses in time on an extracavity detector displays a beat frequency equal to the difference in their CEO frequencies.

interpreted as the frequency difference between the two CEO frequencies, and thus proportional to the external perturbation that caused the shift.

3.2 The laser as a 2-level system

In order to more fully understand how this sensing technique operates, a model of how the electric fields develop inside of the cavity can be developed from first principles. A system of two counter-propagating electric fields in a laser can be described by their so called coupled-mode equation (CME) [14]. This can be developed from first principles i.e. Maxwell's equations governing all electric fields:

$$\nabla \cdot D = \rho_f \qquad \text{Gauss' Law} \tag{3.1}$$

$$\nabla \cdot B = 0 \qquad \text{Gauss' Magnetism Law} \tag{3.2}$$

$$\nabla \times E = -\frac{\partial B}{\partial t} \qquad \text{Faraday's Law} \tag{3.3}$$

$$\nabla \times H = \frac{\partial D}{\partial t} + J_f \qquad \text{Ampere's Law} \tag{3.4}$$

Applying the curl ($\nabla\times$) to both sides of Faraday's law and simplifying (distributive property and curl of curl identity) leads to,

$$\nabla(\nabla \cdot E) - \nabla^2 E = -\nabla \times \frac{\partial B}{\partial t}. \tag{3.5}$$

Since the curl and time derivative operators commute (as any mixed partial derivative should), they can be interchanged on the right-hand-side:

$$\nabla(\nabla \cdot E) - \nabla^2 E = -\frac{\partial}{\partial t}\left(\nabla \times B\right). \tag{3.6}$$

The constitutive relation between the magnetic flux density, B, and the magnetic field strength (or magnetic auxiliary field), H, is,

$$\begin{aligned} B &= \mu_0(H + M) \\ &= \mu_0(H + \chi_m H) \\ &= \mu_0(1 + \chi_m)H \\ &= \mu H. \end{aligned} \tag{3.7}$$

As an aside, keep in mind that H is the magnetic field in vacuum and B is the total magnetic field. This seems to be opposite of the electric field where E is the field in vacuum and the auxiliary displacement field, D, is the total field. In a non-magnetic

material like the one we will consider here, $\mu = \mu_0$. Also, since it can be assumed that the light will propagate in a dielectric, free current can be ignored, $J_f = 0$. This allows us to plug Ampere's law into Eq. 3.6:

$$\nabla(\nabla \cdot E) - \nabla^2 E = -\mu_0 \frac{\partial}{\partial t}\frac{\partial D}{\partial t}. \tag{3.8}$$

The constitutive relations for the displacement and electric field are,

$$\begin{aligned} D &= \epsilon_0 E + P \\ &= \epsilon_0 E + P_L + P_{NL} \\ &= \epsilon_0 E + \epsilon_0 \chi^{(1)} E + P_{NL} \\ &= \epsilon_0 (1 + \chi) E + P_{NL} \\ &= \epsilon E + P_{NL}. \end{aligned} \tag{3.9}$$

Here we consider a linear medium so that $P_{NL} = 0$. This means, since $\rho_f = 0$ in the dielectric, that $\nabla \cdot D = \nabla \cdot \epsilon E = 0$. Using the second equality of Eq. 3.9 results in Eq. 3.8 taking the form,

$$\nabla^2 E - \mu_0 \epsilon_0 \frac{\partial^2 E}{\partial t^2} = \mu_0 \frac{\partial^2 P_L}{\partial t^2}. \tag{3.10}$$

Finally, $\mu_0 \epsilon_0 = 1/c^2$, which leads to the wave equation,

$$\boxed{\nabla^2 E - \frac{1}{c^2}\frac{\partial^2 E}{\partial t^2} = \mu_0 \frac{\partial^2 P_L}{\partial t^2}}. \tag{3.11}$$

Other relations that may be useful include,

$$\epsilon_r = \epsilon/\epsilon_0 = 1 + \chi \tag{3.12}$$

$$\mu_r = \mu/\mu_0 = 1 + \chi_m \tag{3.13}$$

$$n^2 = \epsilon_r \mu_r. \tag{3.14}$$

From here the slowly-varying mode equation can be derived by starting with the 1-Dimensional Ansatz,

$$E(z,t) = \frac{1}{2}\tilde{\mathcal{E}}(z,t) e^{i(kz - \omega t)}, \tag{3.15}$$

so that $\nabla \to \frac{\partial}{\partial Z}$ in the wave equation (plane-wave approximation). From Eq. 3.9 we know that $P_L = \epsilon_0 \chi E$. The wave equation is now,

$$\frac{\partial^2 E}{\partial z^2} - \frac{1}{c^2}\frac{\partial^2 E}{\partial t^2} = \frac{\chi}{c^2}\frac{\partial^2 E}{\partial t^2}. \tag{3.16}$$

One thing not mentioned in the section above is the fact that since we are in an absorbing medium, χ is actually complex. In this case we will specify that n be the index of refraction, or the real part of χ. The constitutive relations can be refined (inserting $\mu_r = 1$ since the dielectric considered here is non-magnetic),

$$\chi = \chi_r + i\chi_i \tag{3.17}$$

$$\epsilon_r = \epsilon/\epsilon_0 = 1 + \chi_r \tag{3.18}$$

$$n^2 = \epsilon_r. \tag{3.19}$$

Eq. 3.16 can be rearranged,

$$\begin{aligned} \frac{\partial^2 E}{\partial z^2} - \frac{1+\chi_r}{c^2}\frac{\partial^2 E}{\partial t^2} &= i\frac{\chi_i}{c^2}\frac{\partial^2 E}{\partial t^2} \\ \frac{\partial^2 E}{\partial z^2} - \frac{n^2}{c^2}\frac{\partial^2 E}{\partial t^2} &= i\frac{\chi_i}{c^2}\frac{\partial^2 E}{\partial t^2}. \end{aligned} \tag{3.20}$$

Using the Ansatz of Eq. 3.15 and the chain rule results in (dropping the explicit z and t amplitude dependence for brevity of notation),[1]

$$\frac{\partial^2 E}{\partial t^2} = \frac{1}{2}\frac{\partial^2 \tilde{\mathcal{E}}}{\partial t^2}e^{i(kz-\omega t)} - i\omega\frac{\partial \tilde{\mathcal{E}}}{\partial t}e^{i(kz-\omega t)} - \frac{1}{2}\omega^2\tilde{\mathcal{E}}e^{i(kz-\omega t)} \tag{3.21}$$

$$\frac{\partial^2 E}{\partial z^2} = \frac{1}{2}\frac{\partial^2 \tilde{\mathcal{E}}}{\partial z^2}e^{i(kz-\omega t)} + ik\frac{\partial \tilde{\mathcal{E}}}{\partial z}e^{i(kz-\omega t)} - \frac{1}{2}k^2\tilde{\mathcal{E}}e^{i(kz-\omega t)}. \tag{3.22}$$

Invoking the slowly varying envelope approximation (SVEO) means that $\partial^2\tilde{\mathcal{E}}/\partial t^2 = \partial^2\tilde{\mathcal{E}}/\partial z^2 = 0$ so Eq. 3.20 becomes,

$$ik\frac{\partial \tilde{\mathcal{E}}}{\partial z} + i\frac{n^2\omega}{c^2}\frac{\partial \tilde{\mathcal{E}}}{\partial t} + \left(\frac{n^2\omega^2}{2c^2} - \frac{1}{2}k^2\right)\tilde{\mathcal{E}} = \frac{\omega\chi_i}{c^2}\frac{\partial \tilde{\mathcal{E}}}{\partial t} - i\frac{\omega^2\chi_i}{2c^2}\tilde{\mathcal{E}}. \tag{3.23}$$

Setting the wavenumber (also known as the propagation constant) to be $k = n\omega/c$, causes the first order term on the left-hand-side to become zero such that we must

[1] There is a shortcut that can be used by noticing that the LHS of Eq. 3.16 can be decomposed into left and right propogating waves: $\frac{\partial^2 E}{\partial z^2} - \frac{1}{c^2}\frac{\partial^2 E}{\partial t^2} = \left(\frac{\partial E}{\partial z} - \frac{1}{c}\frac{\partial E}{\partial t}\right)\left(\frac{\partial E}{\partial z} + \frac{1}{c}\frac{\partial E}{\partial t}\right)$. This significantly simplifies the math and leads to the same Eq. 3.26.

keep the second order $\partial\mathcal{E}/\partial t$ term. This is not the case on the right-hand-side where the first order term remains and suppresses the effect of the second-order term i.e. $(\omega\chi_i/c^2)(\partial\tilde{\mathcal{E}}/\partial t) \ll (i\omega^2\chi_i/2c^2)\tilde{\mathcal{E}}$. Rearranging leads to,

$$ik\frac{\partial\tilde{\mathcal{E}}}{\partial z} + ik\frac{n}{c}\frac{\partial\tilde{\mathcal{E}}}{\partial t} = -i\frac{k^2\chi_i}{2n^2}\tilde{\mathcal{E}} \tag{3.24}$$

$$\frac{\partial\tilde{\mathcal{E}}}{\partial z} + \frac{n}{c}\frac{\partial\tilde{\mathcal{E}}}{\partial t} = \frac{k\chi_i}{2n^2}\tilde{\mathcal{E}}. \tag{3.25}$$

In order to avoid explicitly calculating χ, we will define an effective propogation constant $\beta = k\chi_i/n^2$ in addition to recalling that $n = c/v$.

$$\boxed{\frac{\partial\tilde{\mathcal{E}}}{\partial z} + \frac{1}{v}\frac{\partial\tilde{\mathcal{E}}}{\partial t} = \frac{\beta}{2}\tilde{\mathcal{E}}}. \tag{3.26}$$

This is known as the slowly varying wave equation since the fast varying phase term has been removed such that the equation describes the evolution of the slowly varying complex amplitude, $\tilde{\mathcal{E}}$.

Many recent publications display a coupled-mode equation in time such that an equivalence can be made to the Schrödinger equation [15–22]. In order to convert Eq. 3.55 to depend only on time, the spatial derivative must be converted to a time derivative through,

$$\partial z = v\partial t = \frac{c}{n}\partial t. \tag{3.27}$$

Such that,

$$\frac{\partial\tilde{\mathcal{E}}}{\partial z} = \frac{n}{c}\frac{\partial\tilde{\mathcal{E}}}{\partial t} = \frac{1}{v}\frac{\partial\tilde{\mathcal{E}}}{\partial t}. \tag{3.28}$$

Eq. 3.26 then becomes,

$$\frac{\partial\tilde{\mathcal{E}}}{\partial t} = \frac{\beta}{2}\tilde{\mathcal{E}}, \tag{3.29}$$

where the constants have been absorbed into the propagation constant so that now $\beta = vk\chi_i/2n^2$. Typically Eq. 3.29 is written not in terms of the slowly varying amplitude, $\tilde{\mathcal{E}}$, but the full optical electric field, E. Converting back to that model will make the inclusion of coupling more straighforward. Though, a phase convention must be chosen since, unlike Eq. 3.29, the result is dependent on the chosen notation.

Engineers typically take the phase to be $e^{+i\omega t}$, such that the electric field Ansatz takes the form of,

$$E = \frac{1}{2}\tilde{\mathcal{E}}(t,z)e^{i\omega t}. \tag{3.30}$$

Note that this E is then slightly different from the Ansatz of Eq. 3.15 as the spatial e^{-ikz} phase has been absorbed into the slowly varying amplitude. With this in mind both sides of Eq. 3.29 can be multiplied by $\frac{1}{2}e^{i\omega t}$ to achieve,

$$\frac{1}{2}e^{i\omega t}\frac{\partial\tilde{\mathcal{E}}}{\partial t} = \frac{\beta}{2}E. \tag{3.31}$$

By way of the chain rule,

$$\frac{\partial E}{\partial t} = \frac{1}{2}e^{i\omega t}\frac{\partial\tilde{\mathcal{E}}}{\partial t} + i\omega E, \tag{3.32}$$

so that Eq. 3.31 becomes,

$$\boxed{\frac{\partial E}{\partial t} = \frac{\beta}{2}E + i\omega E,} \tag{3.33}$$

Where we again emphasize that E is slowly varying in spatial frequency, but quickly varying in optical frequency i.e. this E is different from previous sections.

3.2.1 The slowly varying amplitude coupled-mode equations

The equations above are true for lone electric fields, however, to consider a two-level coupled-mode system we require equations that include coupling between two fields. This step is straight forward due to our choice to convert back to the full optical field.

In order to create a coupled-mode equation, we will define two separate electric fields, $E_{1,2}$, that each follow their own mode equation defined by Eq. 3.33. Coupling between the two optical fields is then introduced through the use of a simple complex constant, $K_{1,2}$. Where K_1 is coupling of the second electric field, E_2, into the first electric field, E_1, and K_2 is the opposite. Additionally, since we are considering a laser system, the propogation constant is replaced with a saturable gain term such that,

$$\frac{\beta_{1,2}}{2} = \alpha_{1,2} = \frac{\hat{\alpha}_{1,2}}{1+\theta I_{1,2}+\gamma I_{2,1}} - \alpha_L. \tag{3.34}$$

Here, $\hat{\alpha}_{1,2}$ is the small signal gain, α_L is the loss, and the self/cross saturation coefficiants are θ and γ, respectively. The generic coupled-mode equations are then

$$\frac{\partial E_1}{\partial t} = (\alpha_1 + i\omega_1)E_1 + K_1 E_2 \tag{3.35}$$

$$\frac{\partial E_2}{\partial t} = (\alpha_2 + i\omega_2)E_2 + K_2 E_1. \tag{3.36}$$

To account for experimental realities the coupling constant is split into conservative, $\tilde{\kappa}$, and non-conservative, s, parts such that,

$$K_{1,2} = s_{1,2} + \tilde{\kappa}_{1,2}. \tag{3.37}$$

Conservative coupling means that $\tilde{\kappa}_1 = -\tilde{\kappa}_2^* = \tilde{\kappa}$ (this is a limiting case as shown in section 3.3).

We will observe the slowly-varying, engineering-phase-notation amplitudes from a reference frame that oscillates at an average frequency. Many know this form as changing to the rotating frame. In this case the Ansatz takes the form of,

$$E_{1,2} = \frac{1}{2}\tilde{\mathcal{E}}_{1,2}e^{i\omega_a t}, \tag{3.38}$$

where $\omega_a = (\omega_1 + \omega_2)/2$. Plugging Eq. 3.38 into Eqs. 3.35 and 3.36, leads to (using $s_1 = s_2 = s$, and $\tilde{\kappa}_1 = -\tilde{\kappa}_2^* = \tilde{\kappa}$ in Eq. 3.37):

$$\boxed{\begin{aligned}\frac{\partial \tilde{\mathcal{E}}_1}{\partial t} &= \alpha_1\tilde{\mathcal{E}}_1 - i\frac{\Delta}{2}\tilde{\mathcal{E}}_1 + (s+\tilde{\kappa})\tilde{\mathcal{E}}_2 \\ \frac{\partial \tilde{\mathcal{E}}_2}{\partial t} &= \alpha_2\tilde{\mathcal{E}}_2 + i\frac{\Delta}{2}\tilde{\mathcal{E}}_2 + (s-\tilde{\kappa}^*)\tilde{\mathcal{E}}_1.\end{aligned}} \tag{3.39}$$

Note that teh detuning has been defined as, $\Delta = 2(\omega_2 - \omega_a) = 2(\omega_a - \omega_1) = \omega_2 - \omega_1$. The lab frame beat signal is calculated to be,

$$D_b(t) = |E_1 + E_2|^2 = \frac{1}{4}\left(|\tilde{\mathcal{E}}_1|^2 + |\tilde{\mathcal{E}}_2|^2 + \tilde{\mathcal{E}}_1\tilde{\mathcal{E}}_2^* + \tilde{\mathcal{E}}_1^*\tilde{\mathcal{E}}_2\right). \tag{3.40}$$

Eq. 3.39 can be solved analytically by casting it into a matrix equation,

$$\begin{pmatrix}\dot{\tilde{\mathcal{E}}}_1 \\ \dot{\tilde{\mathcal{E}}}_2\end{pmatrix} = \begin{bmatrix}\alpha_1 - i\Delta/2 & (s+\tilde{\kappa}) \\ (s-\tilde{\kappa}^*) & \alpha_2 + i\Delta/2\end{bmatrix}\begin{pmatrix}\tilde{\mathcal{E}}_1 \\ \tilde{\mathcal{E}}_2\end{pmatrix}, \tag{3.41}$$

which has a characteristic equation of the form,

$$\begin{vmatrix} \alpha_1 - i\Delta/2 - i\lambda & (s+\tilde{\kappa}) \\ (s-\tilde{\kappa}^*) & \alpha_2 + i\Delta/2 - i\lambda \end{vmatrix} = 0, \tag{3.42}$$

and eigenvalues of,

$$\lambda_\pm = -i\frac{\alpha_1+\alpha_2}{2} \pm \frac{\zeta}{2}. \tag{3.43}$$

where $\zeta = \sqrt{4|\tilde{\kappa}|^2 - (\alpha_1 - \alpha_2 - i\Delta)^2 - 4s^2 - 4s(\tilde{\kappa} - \tilde{\kappa}^*)}$. Recalling that to find the eigenvectors we plug the eigenvalue back into the eigenvalue equation,

$$\boldsymbol{H}\,|v_\pm\rangle = \lambda_\pm\,|v_\pm\rangle \tag{3.44}$$

$$\boldsymbol{H} - \lambda_\pm\,|v_\pm\rangle = 0, \tag{3.45}$$

this leads to,

$$\begin{pmatrix} \alpha_1 - i\Delta/2 - i\lambda_\pm & s+\tilde{\kappa} \\ s-\tilde{\kappa}^* & \alpha_2 + i\Delta/2 - i\lambda_\pm \end{pmatrix} \begin{pmatrix} v_{1\pm} \\ v_{2\pm} \end{pmatrix} = 0. \tag{3.46}$$

The eigenvectors are then,

$$|v_\pm\rangle = \begin{bmatrix} 1 \\ \frac{\alpha_2-\alpha_1+i\Delta\pm i\zeta}{2(s+\tilde{\kappa})} \end{bmatrix} \tag{3.47}$$

which means that the two circulating electric fields take the form of,

$$\tilde{\mathcal{E}}_1(t) = c_+ e^{i\lambda_+ t} + c_- e^{i\lambda_- t} \tag{3.48}$$

$$\tilde{\mathcal{E}}_2(t) = c_+ \left(\frac{\alpha_2-\alpha_1+i\Delta+i\zeta}{2(s+\tilde{\kappa})}\right) e^{i\lambda_+ t} + c_- \left(\frac{\alpha_2-\alpha_1+i\Delta-i\zeta}{2(s+\tilde{\kappa})}\right) e^{i\lambda_- t}. \tag{3.49}$$

Using the initial conditions $\tilde{\mathcal{E}}_{1,2}(0)$ allows us to solve for the coefficients,

$$c_- = \frac{i}{2\zeta}\left[2(s+\tilde{\kappa})\tilde{\mathcal{E}}_2(0) - (\alpha_2-\alpha_1+i\Delta+i\zeta)\tilde{\mathcal{E}}_1(0)\right] \tag{3.50}$$

$$c_+ = \mathcal{E}_1(0) - c_-. \tag{3.51}$$

3.2.2 Time-domain simulation

Solving the time domain two-level coupled-mode equations numerically (or algebraically if the saturable gain is assumed to have reached steady-state) gives a

theoretical curve for any IPI laser. Fig. 3.2 shows such a result. The circles are calculated by solving Eq. 3.39 numerically, and then obtaining a beat frequency by extracting the largest Fourier component of Eq. 3.40. The red dotted lines correspond to the analytic solution for the beat frequency, which in this case (using Eq. 3.43) leads simply to a frequency of 2ζ. The solutions plotted in Fig. 3.2 are assumed to be at lasing threshold with a non-saturable gain such that $\alpha_{1,2} = 0$ in Eq. 3.39.

Notice that when conservative and non-conservative coupling are balanced (equivalent to no coupling at all), a linear response is observed (yellow circles). This is the expected ideal IPI response where coupling is minimized [1]. When non-conservative coupling dominates (purple and green circles), there exists an area of zero response at low detunings. These curves are equivalent to a typical gyroscope response with dead-band [12]. The conservative coupling curves (blue and orange circles) are interesting in that they have never been observed due to the experimental challenge that adding strong conservative coupling in a cavity typically destroys lasing.

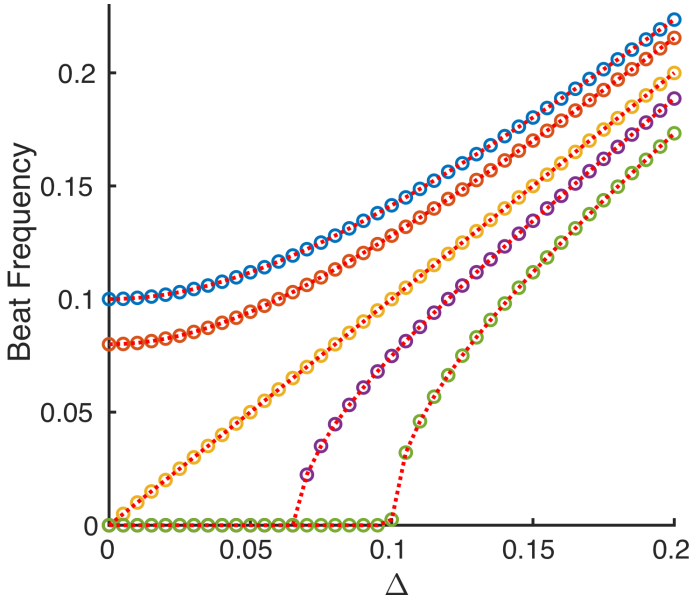

Figure 3.2: The IPI beatnote response curve changes with $\tilde{\kappa}$ and s. All large circles are beat frequencies numerically solved from Eq. (3.39) with $\tilde{\kappa} = 0.05$ and $s = 0$ (blue), $s = 0.03$ (orange), $s = 0.05$ (yellow), and $s = 0.06$ (purple). The green circles are with $\tilde{\kappa} = 0$ and $s = 0.05$. The red dashed curves correspond to the eigenvalue beat frequency 2ζ determined from Eq. (3.43). An example of data matching the $\tilde{\kappa} = 0$ case can be found in [1].

3.2.3 Pulsed time domain model

The time domain model described in previous sections has included no pulse inducing process, and thus the analysis up till now has been valid for continuous wave (cw) lasers. Because a lot of the benefit of IPI comes from the fact that it is an ultrafast technique, a proper analysis including mode-locking should be developed. Instead of forcing the coupled-mode equation to be a time derivative, it seems more straight forward to solve the equations while keeping time and space distinct. A pulse can then be assumed in time and propagated by stepping through space (removing the need to model complicated mode-locking dynamics).

Instead of removing the time derivative from the plane-wave slowly-varying-envelope approximation of the wave equation from Eq. 3.26, a more common transformation is to observe the fields from a frame of reference that moves with the electric fields in time. To accomplish this, a change of coordinates is made such that,

$$\begin{aligned} z' &= z \\ t' &= t - \frac{z}{v}. \end{aligned} \tag{3.52}$$

Propogating this through,

$$\begin{aligned} \tilde{\mathcal{E}}(z,t) &\rightarrow \tilde{\mathcal{E}}(z'(z), t'(z,t)) \\ \frac{\partial \tilde{\mathcal{E}}}{\partial z} &= \frac{\partial \tilde{\mathcal{E}}}{\partial z'}\frac{\partial z'}{\partial z} + \frac{\partial \tilde{\mathcal{E}}}{\partial t'}\frac{\partial t'}{\partial z} \\ &= \frac{\partial \tilde{\mathcal{E}}}{\partial z'} - \frac{1}{v}\frac{\partial \tilde{\mathcal{E}}}{\partial t'} \\ \frac{\partial \tilde{\mathcal{E}}}{\partial t} &= \frac{\partial \tilde{\mathcal{E}}}{\partial z'}\frac{\partial z'}{\partial t} + \frac{\partial \tilde{\mathcal{E}}}{\partial t'}\frac{\partial t'}{\partial t} \\ &= \frac{\partial \tilde{\mathcal{E}}}{\partial t'}. \end{aligned} \tag{3.53}$$

Which means,

$$\begin{aligned} \frac{\partial \tilde{\mathcal{E}}}{\partial z} + \frac{1}{v}\frac{\partial \tilde{\mathcal{E}}}{\partial t} &= \frac{\partial \tilde{\mathcal{E}}}{\partial z'} - \frac{1}{v}\frac{\partial \tilde{\mathcal{E}}}{\partial t'} + \frac{1}{v}\frac{\partial \tilde{\mathcal{E}}}{\partial t'} \\ &= \frac{\partial \tilde{\mathcal{E}}}{\partial z'}. \end{aligned} \tag{3.54}$$

Using the change of coordinates of Eq. 3.54 in Eq. 3.26 leads to,

$$\frac{\partial \tilde{\mathcal{E}}(z',t')}{\partial z'} = \frac{\beta}{2}\tilde{\mathcal{E}}(z',t'). \tag{3.55}$$

This form of the plane-wave slowly-varying-envelope wave equation is commonly referred to as written in the retarded frame of reference.

We now proceed almost identically to the process in section 3.2, but with a spatial derivative instead of time. First, the engineering Ansatz,

$$E(z,t) = \frac{1}{2}\tilde{\mathcal{E}}e^{-i(kz-\omega t)}, \tag{3.56}$$

is used to convert Eq. 3.55 back to the full optical electric field expression resulting in (dropping the primes for brevity):

$$\frac{\partial E(z,t)}{\partial z} = \frac{\beta}{2}E(z,t) - ikE(z,t). \tag{3.57}$$

Next coupling is added to create a coupled-mode equation,

$$\frac{\partial E_1(z,t)}{\partial z} = \frac{\beta_1}{2}E_1(z,t) - ik_1E_1(z,t) + K_1E_2(z,t) \tag{3.58}$$

$$\frac{\partial E_2(z,t)}{\partial z} = \frac{\beta_2}{2}E_2(z,t) - ik_2E_2(z,t) + K_2E_1(z,t). \tag{3.59}$$

The rotating frame engineering phase convention will be used such that,

$$E_{1,2}(z,t) = \frac{1}{2}\tilde{\mathcal{E}}_{1,2}e^{i(\omega_a t - k_a z)}, \tag{3.60}$$

where $\omega_a = (\omega_1 + \omega_2)/2$ and $k_a = n\omega_a/c$ are based on average frequencies. This leads to a coupled-mode equation of,

$$\frac{\partial \tilde{\mathcal{E}}_1(z,t)}{\partial z} = \frac{\beta_1}{2}\tilde{\mathcal{E}}_1(z,t) - i\frac{n\Delta}{2c}\tilde{\mathcal{E}}_1(z,t) + K_1\tilde{\mathcal{E}}_2(z,t) \tag{3.61}$$

$$\frac{\partial \tilde{\mathcal{E}}_2(z,t)}{\partial z} = \frac{\beta_2}{2}\tilde{\mathcal{E}}_2(z,t) + i\frac{n\Delta}{2c}\tilde{\mathcal{E}}_2(z,t) + K_2\tilde{\mathcal{E}}_1(z,t), \tag{3.62}$$

where we again have made use of $\Delta = \omega_2 - \omega_1$. In order for this differential equation to accurately model an IPI laser it needs to step forward one cavity round trip at a time. Thus, a model describing an IPI laser with a cavity length of, L, results in,

$$\boxed{\begin{aligned}\frac{\partial \tilde{\mathcal{E}}_1(x,t)}{\partial x} &= \alpha_1\tilde{\mathcal{E}}_1(x,t) - i\frac{\Delta\varphi}{2}\tilde{\mathcal{E}}_1(x,t) + s\tilde{\mathcal{E}}_2(x,t)\\ \frac{\partial \tilde{\mathcal{E}}_2(x,t)}{\partial x} &= \alpha_2\tilde{\mathcal{E}}_2(x,t) + i\frac{\Delta\varphi}{2}\tilde{\mathcal{E}}_2(x,t) + s\tilde{\mathcal{E}}_1(x,t),\end{aligned}} \tag{3.63}$$

where $x = z/L$ is the round-trip index, $\alpha_i = \beta_i L/2$ is the round-trip gain/loss, $\Delta\varphi = n\Delta L/c = \Delta\tau_p$ is the angular round-trip phase detuning, and s is the non-conservative round-trip coupling parameter. If the pulses are shorter than the energy relaxation time of the gain medium, the net saturable gain is given by (assuming no cross saturation if the pulses do not meet in the gain medium),

$$\alpha_i = \frac{\alpha_0}{1 + \frac{W_i}{W_s}} - \alpha_L, \tag{3.64}$$

where, now, W_s is the saturation energy density and the pulse energy is given by, $W_i = \int(|\tilde{\mathcal{E}}_i|^2 dt)$.

An initial Gaussian pulse is assumed in time, which can then be stepped through the laser cavity one round-trip at a time according to Eq. 3.63. To give a concrete example, Fig. 3.3a shows the resultant pulse train after taking the inset initial Gaussian pulse and solving Eq. 3.63 with a 7th order butcher predictor-corrector differential solving algorithm. Taking the Fourier transform of each pulse train clearly

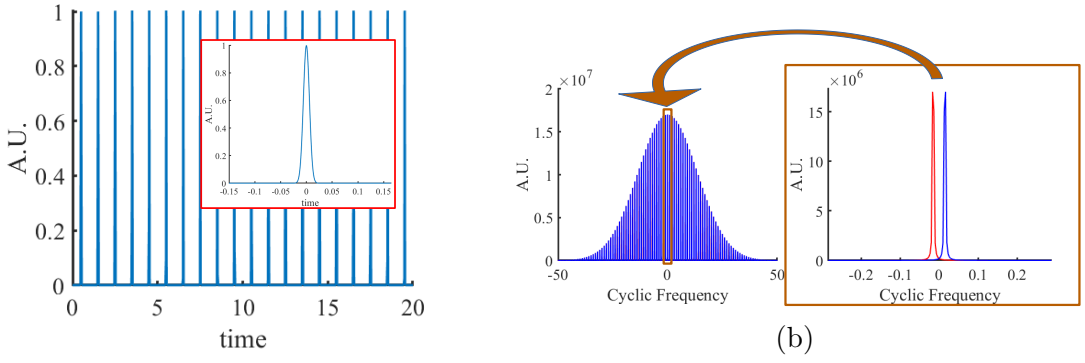

(a) (b)

Figure 3.3: Resultant pulse train (a) and corresponding frequency comb (b) after solving Eq. 3.63 with $\alpha_{1,2} = 0$, $\Delta\varphi = 0.03/(2\pi)$, and $s = 0$. The solution was calculated using 300 round-trips and the repetition rate was set by the zero padding around the intial pulse in time which extended from $[-0.5, 0.5]$ with steps of 0.001. In (a) the two pulse trains are exactly overlapped in time, while (b) shows that the two frequency combs have CEO frequencies that are offset by the applied detuning.

shows that this can be described by two frequency combs with CEO frequencies offset by the detuning (see Fig. 3.3b). The beat signal that would be recorded by a detector

in time is calculated according to Eq. 3.40 where $\tilde{\mathcal{E}}_1$ and $\tilde{\mathcal{E}}_2$ are the full pulse trains in time calculated from Eq. 3.63. The beat signal corresponding to the pulse trains in Fig. 3.3a is shown in Fig. 3.4a where the envelope has a frequency of $\Delta\varphi = 0.03/(2\pi)$. An interesting observation is that when coupling is added ($s = 0.02$) to the model

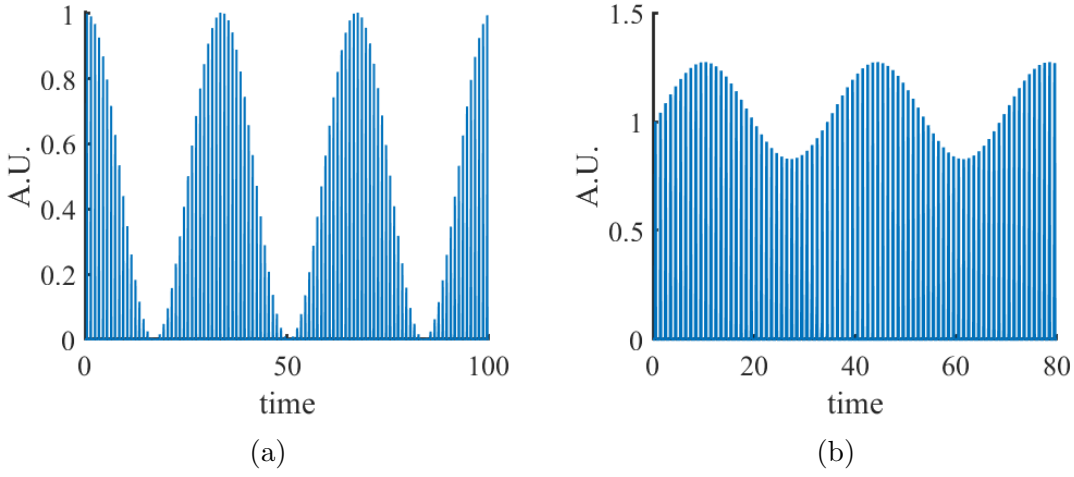

(a) (b)

Figure 3.4: The beat signals observed by a detector as predicted by the model of Eq. 3.63. In a typical experiment a slow detector would be used to extract just the envelope and an RF spectrum analyzer would be used to extract the beat frequency. When the signal is in the linear response region of the detector, the beat frequency is equivalent to the detuning which in the case of (a) is $\Delta\varphi = 0.03/(2\pi)$. If a coupling of $s = 0.02$ is added such that the same detuning places the system near the dead band edge, the pulse trains become amplitude modulated such that the beat frequency is not equal to the applied detuning.

of Eq. 3.63, and the detuning is set such the system is within the dead band curve ($\Delta\varphi = 0.03/(2\pi)$), the pulse trains become amplitude modulated due to the coupling. This effect can be seen in Fig. 3.4b and results in a distortion of the beat signal in time as discussed in [20] [2].

3.2.4 Pulsed frequency domain simulation

For many things, including implementing sensor enhancement (as will be explained in Chapter 5.4), a model of IPI in the frequency domain is required. While one could

[2] We call it a distortion of the beat signal because not only is the beat frequency different than without coupling, but the modulation depth is no longer 100% either

simply take the model in time and Fourier transform into the frequency domain, this method would require several computationally intense fast Fourier transforms to be calculated every round-trip. Additionally, in order to obtain the frequency resolution required, large data arrays in time would be necessary. These computational hurdles can be avoided entirely by creating a model that operates entirely in the frequency domain. The resultant frequency comb will be built by assuming an oscillating intracavity signal that picks up a specified round-trip phase.

If $E(t,z)$ is some unspecified electric field (say, for instance, random noise) confined to the single z spatial direction, it can be propagated forward in space and time using Maxwell's equations,

$$\left[\nabla^2 - \frac{n^2}{c^2}\frac{\partial^2}{\partial t^2}\right] E(t,z) = 0. \tag{3.65}$$

Considering that only one spatial dimension is accounted for and taking the Fourier transform in order to obtain a propagation relation in the frequency domain gives,

$$\left[\frac{\partial^2}{\partial z^2} - \frac{n^2}{c^2}\Omega^2\right] E(\Omega,z) = \left[\frac{\partial}{\partial z} - i\frac{n}{c}\Omega\right]\left[\frac{\partial}{\partial z} + i\frac{n}{c}\Omega\right] E(\Omega,z) = 0, \tag{3.66}$$

where we have defined $\mathcal{F}\{E(t,z)\} = E(\Omega,z)$. The second expression shows this is equivalent to applying both a forward and backward propagation operator. Without loss of generality we can consider just the forward propagation term,

$$\left[\frac{\partial}{\partial z} + i\frac{n}{c}\Omega\right] E(\Omega,z) = 0, \tag{3.67}$$

which can be solved exactly as,

$$E(\Omega,z) = E(\Omega,0)e^{-i\frac{n}{c}\Omega z}. \tag{3.68}$$

$E(\Omega,0)$ is some unspecified field which may or may not peak at some frequency $\Omega = \omega$, c is the speed of light in vacuum, and $n = n(\Omega)$ is the index of refraction which is, in general, a function of frequency.

If this field is placed inside of a resonator of length L, Eq. (3.68) states that each round-trip the field will pick up a phase of $\exp(-in\Omega L/c)$ just by the nature of

propagation. The internal cavity electric field spectrum can then be represented by summing each round-trip as,

$$E(\Omega, N_{rt}) = \sum_{N=0}^{N_{rt}} E(\Omega, 0) e^{-i\frac{n}{c}\Omega N L}, \tag{3.69}$$

where N_{rt} is the total number of round-trips inside of the laser cavity. Defining the round-trip time as $\tau = nL/c$, and simplifying the sum as a finite geometric series leads to,

$$E(\Omega, N_{rt}) = E(\Omega, 0) \sum_{N=0}^{N_{rt}} \left[e^{-i\Omega\tau}\right]^N \tag{3.70}$$

$$= E(\Omega, 0) \frac{1 - \left[e^{-i\Omega\tau}\right]^{N_{rt}+1}}{1 - e^{-i\Omega\tau}}. \tag{3.71}$$

This describes a frequency comb with teeth separated by $\nu_{rt} = 1/\tau$, that have a linewidth inversely proportional to N_{rt}.

In order to simulate a more realistic situation we must include the fact that the index of refraction is dependent on frequency. We can include this effect in our model by Taylor expanding the index around some unspecified frequency, ω.

$$n(\Omega) = n_0 + (\Omega - \omega) \left.\frac{dn}{d\Omega}\right|_\omega + \frac{(\Omega - \omega)^2}{2} \left.\frac{d^2 n}{d\Omega^2}\right|_\omega + \dots \tag{3.72}$$

To save on computing power, we will shift the x-axis to zero frequency with the substitution $\Delta\Omega = \Omega - \omega \Rightarrow \Omega = \Delta\Omega + \omega$. For brevity we will also use $E(\Omega, z) = E(\omega + \Delta\Omega, z) = \tilde{\mathcal{E}}(\Delta\Omega, z)$. Making these substitutions in Eq. (3.68) leads to,

$$E(\Omega, z) = E(\omega + \Delta\Omega, z) = \tilde{\mathcal{E}}(\Delta\Omega, z) = \tilde{\mathcal{E}}(\Delta\Omega, 0) e^{-i\frac{\Omega z}{c} n(\Omega)} \tag{3.73}$$

$$= \tilde{\mathcal{E}}(\Delta\Omega, 0) e^{-i\frac{(\omega+\Delta\Omega)z}{c} n(\omega+\Delta\Omega)}. \tag{3.74}$$

The phase factor can be simplified as (keeping only the first 3 terms of the Taylor expansion),

$$\phi = \frac{\Omega L}{c} n(\Omega) \tag{3.75}$$

$$= \frac{(\omega + \Delta\Omega)L}{c} \left[n_0 + \Delta\Omega \left.\frac{dn}{d\Omega}\right|_\omega + \frac{\Delta\Omega^2}{2} \left.\frac{d^2 n}{d\Omega^2}\right|_\omega\right] \tag{3.76}$$

$$= L\left[\frac{\omega n_0}{c} + \frac{\Delta\Omega}{c}\left(n_0 + \omega\frac{dn}{d\Omega}\Big|_\omega\right) + \frac{\Delta\Omega^2}{c}\left(\frac{dn}{d\Omega}\Big|_\omega + \frac{\omega}{2}\frac{d^2n}{d\Omega^2}\Big|_\omega\right)\right] \tag{3.77}$$

$$= L\left[\frac{\omega}{v_p} + \frac{\Delta\Omega}{v_g} + \frac{\Delta\Omega^2}{2}\mathrm{GVD}\right]. \tag{3.78}$$

where the higher order $\Delta\Omega^3$ term has been thrown out, GVD is the group velocity dispersion parameter, v_p is the phase velocity, and v_g is the group velocity (all of which are defined at the expansion frequency ω). However, by shifting the first frequency tooth to zero frequency, we have inherently set the carrier-to-envelope offset frequency to zero. In other words, there is no dispersion in the cavity (GVD=0, leading to rigorously evenly spaced teeth) and the group and phase velocities are equivalent ($v_g = v_p$). Taking that into consideration and defining the phase round-trip time as $\tau_p = L/v_p$ leads to:

$$\phi = \tau_p(\omega + \Delta\Omega). \tag{3.79}$$

In a lasing cavity without perturbation $\omega\tau_p = 2\pi q$, (q =integer) and thus the comb is centered at zero.

The principle of IPI stems from a differential measurement between two shifted frequency combs. For the specific example of a laser gyroscope, the shift is caused by the optical path length difference between two counterpropagating electric fields in a rotating cavity. To account for this we add a length perturbation to the cavity as $z = L \pm \ell/2$ in Eq. (3.78) where ℓ is the difference in length travelled by the counterpropagating fields each round-trip,

$$\phi = (L + \frac{\ell}{2})\left[\frac{\omega}{v_p} + \frac{\Delta\Omega}{v_p}\right] \tag{3.80}$$

$$= \frac{\omega}{v_p}(L + \frac{\ell}{2}) + \frac{\Delta\Omega}{v_p}(L + \frac{\ell}{2}) \tag{3.81}$$

$$= 2\pi q + \frac{\omega\ell}{2v_p} + \Delta\Omega\frac{L}{v_p} \tag{3.82}$$

$$= \frac{\omega\ell L}{2v_pL} + \Delta\Omega\tau_p \tag{3.83}$$

$$= \frac{\omega\ell}{2L}\tau_p + \Delta\Omega\tau_p \tag{3.84}$$

$$= \left(\frac{\Delta\varphi}{2} + \Delta\Omega\right)\tau_p \tag{3.85}$$

This derivation has utilized the fact that in a lasing cavity $\omega L/v_p = 2\pi q$ (where q is an integer), $L \gg \ell/2$, and the round-trip differential phase shift, $\Delta\varphi = \omega\ell/L$ is the same as that defined in the time domain model. The $2\pi q$ term can be dropped due to the fact that this expression represents a phase. Plugging this phase into Eq. 3.71 leads to an expression describing two frequency combs offset from $\Delta\Omega = 0$ by an amount exactly corresponding to the applied detuning, $\Delta\varphi$. In order to measure this quantity, the two frequency combs are interfered on a detector in time and the beat signal, $D_b(\Delta\Omega)$, is measured. This frequency domain signal can be extracted as (taking the Fourier transform of $D_b(t)$ from Eq. 3.40),

$$\begin{aligned} D_b(\Delta\Omega) = \frac{1}{2\eta}\big|&\tilde{\mathcal{E}}_1(\Delta\Omega)\otimes\tilde{\mathcal{E}}_1(\Delta\Omega) + \tilde{\mathcal{E}}_2(\Delta\Omega)\otimes\tilde{\mathcal{E}}_2(\Delta\Omega)\ldots \\ &+ \tilde{\mathcal{E}}_1(\Delta\Omega)\otimes\tilde{\mathcal{E}}_2(\Delta\Omega) + \tilde{\mathcal{E}}_2(\Delta\Omega)\otimes\tilde{\mathcal{E}}_1(\Delta\Omega)\big|^2. \end{aligned} \tag{3.86}$$

where the cross-correlation function is defined as,

$$A(x)\otimes B(x) = \int_{-\infty}^{\infty} A^*(\tau)B(x+\tau)d\tau. \tag{3.87}$$

The frequency comb expression implementing Eq. 3.85 is slightly misleading. First it seems to imply that changing the phase delay, τ_p should change the frequency tooth spacing defined by the $\Delta\Omega\tau_p$ term. Second, we have been treating the phase and group velocity as equivalent to each other, which implies that the CEO frequency is 0. But, there is a detuning term that shifts the CEO frequency, and thus the velocities should now be different. These issues are resolved by the fact that we have not accounted for higher order dispersion terms, nonlinear kerr phase, and saturable absorption pulse shaping effects. Experimentally, we know that the nonlinear phase and chromatic dispersion are involved in a dance that results in a rigorously spaced dispersionless soliton circulating in the cavity. This leads to a tooth spacing (equivalent to round-trip time) that are not explicitly dependent on the v_p or v_g that were introduced above. Our model is therefore only accurate if it is limited to the middle frequency mode near $\Delta\Omega = 0$ since the tooth spacing is not defined properly. Luckily that is all that is needed to calculate the IPI response.

The frequency model can be extended to include saturable gain and coupling between the counter-propagating pulses ($\pm$) such that it is equivalent to the time

domain model. Since Fourier transformations are linear operations, the coupling can be simply introduced the same way as in the time domain. The coupling and gain prevents a neat closed form solution such that each round-trip must be stepped through numerically. We choose here a non-conservative coupling, s. To calculate the next round trip, $x+1$, from the current round trip, x, the two counter-propagating fields are first propagated around the cavity just as before,

$$\tilde{\mathcal{A}}_{\pm} = \tilde{\mathcal{A}}_{\pm,x} e^{-i\tau_p(\pm\Delta\varphi/2+\Delta\Omega)}. \tag{3.88}$$

Next the fields are injected into each other according to the coupling parameter,

$$\tilde{\mathcal{A}}c_{\pm} = \tilde{\mathcal{A}}_{\pm} + s\tilde{\mathcal{A}}_{\mp}. \tag{3.89}$$

Gain is then applied to these coupled amplitudes using the same gain parameter from Eq. 3.64 to obtain the field after a full round-trip,

$$\tilde{\mathcal{A}}_{\pm,x+1} = \tilde{\mathcal{A}}c_{\pm} + \alpha_{1,2}\tilde{\mathcal{A}}c_{\pm}. \tag{3.90}$$

This field is saved in memory and then used as the input for the next round-trip. The final measureable field is then found by summing all of the round trips,

$$\tilde{\mathcal{E}}_{\pm,N_{rt}} = \sum_{x=0}^{N_{rt}} \tilde{\mathcal{A}}_{\pm,x}. \tag{3.91}$$

Without saturable gain the non-conservative coupling will cause the system to diverge. Figure 3.5 shows the result of this coupled frequency domain calculation with and without coupling. This simulation used $N_{rt} = 100$, $\Delta\varphi = 0.27$, $\tau_p = 1$, and gain parameters of $\alpha_0 = 1$, $\alpha_L = 0.05$, and $W_s = 1$. The pulse time domain model gives the same solution, however, the frequency domain calculation includes no numerically messy Fourier transforms, and allows a more straightforward way to add the dispersion enhancement that will be introduced in chapter 5.

3.3 An Aside Regarding Coupling

This section came about due to the need to understand the conservative coupling relation $\kappa_1 = -\kappa_2^*$. It had been used in several places without explicit derivation

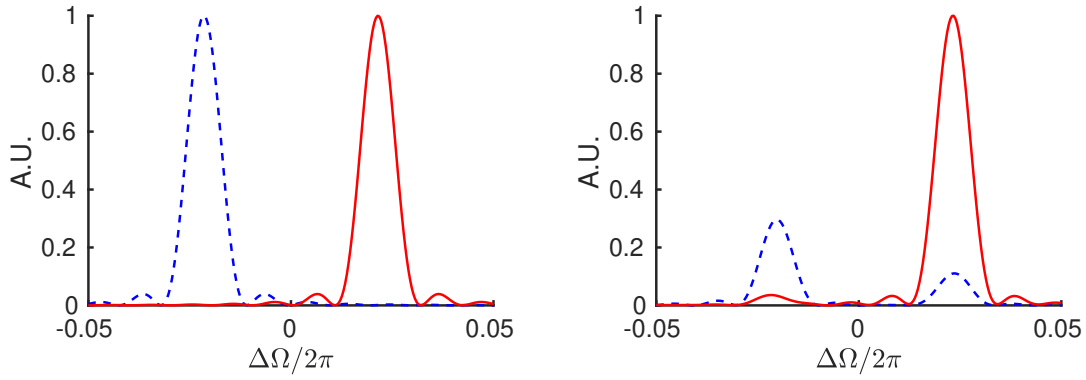

Figure 3.5: Numerical solution showing the first frequency comb tooth of the two electric fields (red,blue) defined by Eq. (3.91) after 100 round-trips with no coupling, $s = 0$,(a) and coupling, $s = 0.1e^{(1i)}$,(b). Both simulations were carried out with a detuning of $\Delta\varphi = 0.27$, gain of $\alpha_0 = 1$, $\alpha_L = 0.05$, and $W_s = 1$, and $\tau_p = 1$. When coupling is included, energy is passed back and forth between the two electric field such that which field is maximum depends on when the FT is truncated in time.

[13, 20, 23, 24], however, a much simpler relation, $\kappa_1 = -\kappa_2$ showed up in other places [16, 18, 19, 25]. While the former simplifies to the later in the limit of real coupling, in general, a complex coupling exists. Therefore a rigorous analysis was required and is summarized below.

3.3.1 Real Stokes Relations

The most basic interface is simply a change of index of refraction. The behavior of an electric field encountering such an interface is described by the Fresnel coefficients. At normal incidence the S and P polarized electric fields exhibit the same reflection and transmission such that,

$$\begin{aligned} r_{12} &= \frac{n_1 - n_2}{n_1 + n_2} \\ t_{12} &= 1 + r_{12}, \end{aligned} \tag{3.92}$$

where $r_{12}E_0$ and $t_{12}E_0$ describe the reflected and transmitted fields when the incident field, E_0, traverses from a medium with index n_1 to a medium with index n_2. Note that lossless homogenous media are being considered such that these relations are

real. An electric field that propagates in the opposite direction will then encounter Fresnel coefficients of,

$$\begin{aligned} r_{21} &= -\frac{n_1 - n_2}{n_1 + n_2} \\ t_{21} &= 1 + r_{21}, \end{aligned} \tag{3.93}$$

Equating and rearranging Eqs. 3.92 and 3.93 leads directly to the Stokes relations in their typical form:

$$\begin{aligned} r_{12} &= -r_{21} \\ t_{12}t_{21} + r_{12}^2 &= 1. \end{aligned} \tag{3.94}$$

Note that these relations can be derived without relying on the Fresnel coefficients by using a time-reversal argument that invokes energy conservation.

Since a negative reflection coefficient corresponds to a π phase shift through Euler's formula, $-r = re^{i\pi}$, the Stokes relations show that there is a π phase difference between fields reflecting off of opposite sides of the same interface. Though, to know which field actually gains the π phase shift (it is the one moving from low to high index), the Fresnel equations must be used. This fact can also be determined experimentally where it is known that laser damage occurs at interfaces that move from high to low, where the reflected wave adds in phase with the input wave (since there is no π phase shift).

Most interfaces that electric fields encounter are not simple interfaces as described above, but include thin films to control reflection. Macroscopic behavior of light reflecting off or transmitting through surfaces is typically due to thin film interference on the surface. In this case, the above Stokes relations are not necessarily valid.

3.3.2 Complex Stokes Relations

A coated optical surface can be modelled as a stack of simple thin interfaces separated by free-space propagation. When a right propagating electric field encounters such a multilayered optical surface, the reflected and transmitted fields are the result from

the interference from all of the layers. The right moving transmitted wave is the sum of every right moving field after the energy has been bounced around between the layers (and similarly with the left moving reflected wave being the sum of all left moving fields). To calculate these resultant fields, the right moving and left moving waves must be recorded at each interface. At each simple thin layer interface, the incoming fields (from each direction) are split according to the scattering, S, matrix defined as [26]:

$$\begin{bmatrix} E_2 \\ E_1' \end{bmatrix} = \begin{bmatrix} t_{12} & r_{21} \\ r_{12} & t_{21} \end{bmatrix} \begin{bmatrix} E_1 \\ E_2' \end{bmatrix}, \tag{3.95}$$

where E_2' is the left moving incoming wave on the right side of the interface and E_1 is the right moving incoming wave from the left side of the interface. Notice that the S matrix describes a set of two equations. The first equation, $E_2 = t_{12}E_1 + r_{21}E_2'$, states that the right moving outgoing wave on the right side of the interface, E_2, is a combination of the right moving incoming wave from the left that is transmitted through the interface, $t_{12}E_1$, and the left moving incoming electric field incoming from the right that is reflected, $r_{21}E_2'$. Similarly, the second equation, $E_1' = r_{12}E_1 + t_{21}E_2'$, shows that the left moving outgoing field, E_1', is a linear combination of the reflected right moving incoming wave, $r_{12}E_1$, and the transmitted left moving wave incoming from the right, $t_{21}E_2'$ (see Fig. 3.6 for clarity) [3].

The elements of the S matrix have real physical significance; they are the field reflection and transmission amplitudes of a layer. Unfortunately, the S matrix is not useful for building up multilayer surfaces as these matrices cannot be cascaded. What is needed is a matrix defining each layer that can be multiplied by the matrices corresponding to the other layers to create an effective total matrix for the whole surface. Instead of equations defining the relationship between incoming and outgoing fields at each layer, the equations need to define the relationship between the fields

[3] To summarize, the electric field subscripts $(1, 2)$ describe whether the field is on the left or right side of the interface, while the no prime and prime discern whether the field is right-propagating or left-propagating, respectively. The coefficients syntax is such that t_{12} and r_{12} describe the transmission and reflection coefficient of the wave starting on side 1 while t_{21} and r_{21} describe the coefficients of a field incoming from side 2.

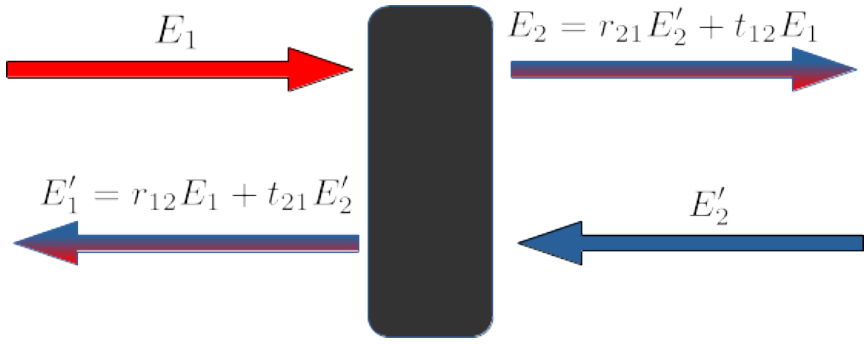

Figure 3.6: Thin simple interface incoming and outgoing wave equations.

on the left side of the layer and the right side of the layer (regardless of whether they are incoming or outgoing). In other words, in order to cascade the matrix layers, the matrix equation needs to move through the surface spatially (left to right) instead of causally (incoming to outgoing). Such a matrix is defined as the wave-transfer, M, matrix. This rearranged equation is,

$$\begin{bmatrix} E_2 \\ E_2' \end{bmatrix} = [M] \begin{bmatrix} E_1 \\ E_1' \end{bmatrix}, \tag{3.96}$$

where the relationship between the M and S matrices is,

$$M = \begin{bmatrix} A & B \\ C & D \end{bmatrix} = \frac{1}{t_{21}} \begin{bmatrix} t_{12}t_{21} - r_{12}r_{21} & r_{21} \\ -r_{12} & 1 \end{bmatrix} \tag{3.97}$$

$$S = \begin{bmatrix} t_{12} & r_{21} \\ r_{12} & t_{21} \end{bmatrix} = \frac{1}{D} \begin{bmatrix} AD - BC & B \\ -C & 1 \end{bmatrix}. \tag{3.98}$$

In order to use the cascaded matrix method, each layer is defined using its physical S matrix. Each S is converted into an M matrix, which are then multiplied together to give an effective total M_T matrix for the entire surface. This ultimate M_T matrix is converted back into a total S_T matrix to extract the effective physical parameters of the multilayer interface. Where the total effective scattering matrix, S_T, has elements that represent,

$$S_T = \begin{bmatrix} t & r' \\ r & t' \end{bmatrix}, \tag{3.99}$$

where t and r are the transmission and reflection coefficients for a beam incoming to the front surface, and t', r' are the similar coefficients for a beam incoming to the back surface.

Free-Space Propagation Matrix

The most simple layer is free-space propagation with no change of index. Since there is no reflection or transmission, such a layer does nothing but add a phase factor of $\phi = nkd$, where n is the refractive index, k the wavenumber of the electric field, and d the propagation distance. The scattering matrix of a free-space layer is then,

$$S_\phi = \begin{bmatrix} e^{-i\phi} & 0 \\ 0 & e^{-i\phi} \end{bmatrix}, \tag{3.100}$$

since the same phase factor is added regardles of propagation direction. Converting the scattering matrix to the wave-transfer matrix results in,

$$M_\phi = \begin{bmatrix} e^{-i\phi} & 0 \\ 0 & e^{i\phi} \end{bmatrix}. \tag{3.101}$$

Dielectric Interface Matrix

The scattering matrix of a dielectric interface can be defined using the Fresnel coefficients of Eqs. (3.92) and (3.93). If the right-propagating incoming electric field starts in index n_1 and propagates into n_2, then the S matrix is,

$$S_{12} = \frac{1}{n_1 + n_2} \begin{bmatrix} 2n_1 & n_2 - n_1 \\ n_1 - n_2 & 2n_2 \end{bmatrix}. \tag{3.102}$$

This corresponds to a wave-transfer matrix of,

$$M_{12} = \frac{1}{2n_2} \begin{bmatrix} n_2 + n_1 & n_2 - n_1 \\ n_2 - n_1 & n_2 + n_1 \end{bmatrix}. \tag{3.103}$$

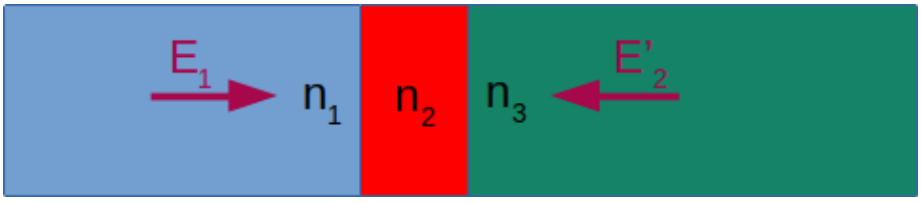

Figure 3.7: Multilayer surface of two interfaces separated by a propagation through material of index n_2.

Dielectric Stack Matrix

Any dielectric stack can then be built up using the propagation and interface matrices. As an example let us imagine a 3 layer dielectric stack as shown in Fig. 3.7. In this case the propagation through the end caps will not be considered such that the first matrix encountered is the interface. Because matrix multiplication requires multiplying in the reverse order, the total effective M matrix for this system is represented as,

$$\begin{aligned} M_T &= M_{23}M_{\phi_2}M_{12} \\ &= \frac{1}{4n_3n_2}\begin{bmatrix} n_3+n_2 & n_3-n_2 \\ n_3-n_2 & n_3+n_2 \end{bmatrix}\begin{bmatrix} e^{-i\phi_2} & 0 \\ 0 & e^{i\phi_2} \end{bmatrix}\begin{bmatrix} n_2+n_1 & n_2-n_1 \\ n_2-n_1 & n_2+n_1 \end{bmatrix} \\ &= \frac{1}{2n_3n_2}\begin{bmatrix} (n_3n_2+n_1n_2)\cos(\phi_2)-i(n_2^2+n_1n_3)\sin(\phi_2) & (n_3n_2-n_1n_2)\cos(\phi_2)-i(n_2^2-n_1n_3)\sin(\phi_2) \\ (n_3n_2-n_1n_2)\cos(\phi_2)+i(n_2^2-n_1n_3)\sin(\phi_2) & (n_3n_2+n_1n_2)\cos(\phi_2)+i(n_2^2+n_1n_3)\sin(\phi_2) \end{bmatrix}. \end{aligned}$$

Converting this to the scattering matrix using Eq. 3.98 results in,

$$S_T = \begin{bmatrix} \frac{2n_1n_2}{\alpha+i\beta} & \frac{\alpha'-i\beta'}{\alpha+i\beta} \\ \frac{-\alpha'-i\beta'}{\alpha+i\beta} & \frac{2n_2n_3}{\alpha+i\beta} \end{bmatrix}, \tag{3.104}$$

where $\alpha = (n_2n_3+n_1n_2)\cos(\phi_2)$, $\alpha' = (n_2n_3-n_1n_2)\cos(\phi_2)$, $\beta = (n_2^2+n_1n_3)\sin(\phi_2)$, and $\beta' = (n_2^2-n_1n_3)\sin(\phi_2)$. Separating each element of S_T into real and imaginary parts leads to,

$$S_T = \frac{1}{\alpha^2+\beta^2}\begin{bmatrix} 2\alpha n_1n_2 - i2\beta n_1n_2 & \alpha'\alpha-\beta'\beta-i(\alpha'\beta+\beta'\alpha) \\ -\alpha'\alpha-\beta'\beta+i(\alpha'\beta-\beta'\alpha) & 2\alpha n_2n_3 - i2\beta n_2n_3 \end{bmatrix}. \tag{3.105}$$

Taking the off-diagonals of Eq. 3.105 that represent r and r', and expanding leads

to,

$$(\alpha^2+\beta^2)r_{21} = [(n_1n_2)^2+(n_2n_3)^2]\cos^2(\phi_2) - [(n_2^2-(n_1n_3)^2)]\sin^2(\phi_2)... \\ ... + i[(n_1^2n_2n_3 - n_2^3n_3)\sin(2\phi_2)] \quad (3.106)$$

$$(\alpha^2+\beta^2)r_{12} = -[(n_1n_2)^2+(n_2n_3)^2]\cos^2(\phi_2) - [(n_2^2-(n_1n_3)^2)]\sin^2(\phi_2)... \\ ... + i[(n_1n_2n_3^2 - n_1n_2^3)\sin(2\phi_2)]. \quad (3.107)$$

It is easy to see that if $n_2 = \sqrt{n_1n_3}$, and $\phi_2 = n_2kd_2 = \pi/2$, that this interface acts as an anti-reflection coating i.e. $r = r' = 0$.

One might naively expect that energy conservation should lead to a tidy relationship between the reflections from either side of any interface. However, the result here implies that there is no general relationship that exists between r and r'. In order to recover a tidy relationship, the transfer matrix must begin and end in the same material.

Non-Reciprocal Submerged Dielectric Stack

If the AR coating system derived above is submerged in a material such that the light begins and ends in the same medium, the multilayer surface results in a more tidy relationship between the matrix elements. Fig. 3.8 represents the surface being modelled.

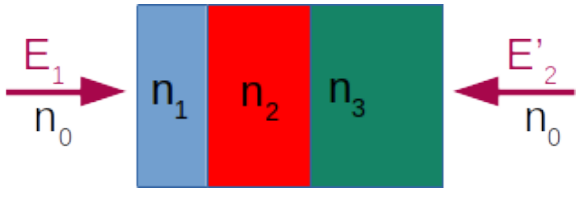

Figure 3.8: Submerged dielectric stack. This system is non-reciprocal, but begins and ends in the same medium.

The wave-transfer matrix for the surface is,

$$M_T = M_{30}M_{\phi_3}M_{23}M_{\phi_2}M_{12}M_{\phi_1}M_{01}. \quad (3.108)$$

The algebraic solution is much too complicated to calculate by hand, so I will show the results of a numerical calculation using $n_0 = 1$, $n_1 = 1.1$, $n_2 = 1.3$ $n_3 = 1.5$, $\phi_1 = 1$, $\phi_2 = 2$, and $\phi_3 = 3$. In this case the scattering matrix is,

$$S_T = \begin{bmatrix} 0.9387 + i0.29 & -0.1638 + i0.0884 \\ 0.0854 + i0.1654 & 0.9387 + i0.29 \end{bmatrix}. \tag{3.109}$$

The relations that are followed are,

$$\boxed{\begin{aligned} |t| &= |t'| && (3.110)\\ |r| &= |r'| && (3.111)\\ |t|^2 + |r|^2 &= 1 && (3.112)\\ \frac{t}{t'^*} &= -\frac{r}{r'^*}. && (3.113) \end{aligned}}$$

These relations are true for any index or phase values used for the layers. Thus, these relations are general for any dielectric system that begins and ends in the same medium where energy is conserved.

The basic stoke relation of $r = -r'$ is recovered if the phase of the transmission and reflection coefficients are zero. This is the case for a system where $\phi_1 = \phi_2 = \pi/2$ and $\phi_3 = \pi$ (using same index values as above), such that,

$$S_T = \begin{bmatrix} 0.9862 & -0.1655 \\ 0.1655 & 0.9862 \end{bmatrix}. \tag{3.114}$$

Notice that the relation mentioned at the beginning of the section is now present if the transmission coefficient phase is zero. In this case $r = -r'^*$, which can be seen when the phase values are set to $\phi_1 = 2.1283$, $\phi_2 = 1$, $\phi_3 = 0$ (again using the same indices),

$$S_T = \begin{bmatrix} -0.9902 & -0.1187 - i0.0737 \\ 0.1187 - i0.0737 & -0.9902 \end{bmatrix}. \tag{3.115}$$

Therefore, the relation $\kappa_1 = -\kappa_2^*$ is a limiting case of conservative coupling where the transmission phase is zero.

3.3.3 Fabry-Perot

The confusion about the conservative coupling equation that led to this analysis came from the derivation in [23] which uses the stokes relations of,

$$tt' - rr' = 1 \tag{3.116}$$

$$r = -r'^{*}. \tag{3.117}$$

Notice that these are particular representations of the more general relations (3.110)-(3.113). If t and t' are fully real, then Eq. (3.113) directly implies that Eq. (3.117) is true. Additionally, Eq. (3.116) is nothing more than Eq. (3.112) with the added assumption that t is fully real. To see this, rewrite Eq. (3.112) as, $tt^* + rr^* = 1$. If t is fully real then $t^* = t$ such that, $tt + rr^* = 1$. Using Eq. (3.110) it can be rewritten as, $tt' + rr^* = 1$. Now again since Eq. (3.117) is true when t is fully real, we land at $tt' - rr' = 1$. Thus, the reason that the textbook concludes that $r = -r'^{*}$ is due to the fact that t has been assumed to be fully real through the use of Eq. (3.116).

The fully general (including phase shifts induced by optical coatings) Fabry-Perot transmission and reflection equations can be derived using the matrix method. Fig. 3.9 shows the FP being modelled. While the interfaces are assumed to be coated, the FP can be broken up into 3 sections (X,Y,Z) that begin and end in the same medium such that the relations (3.110)-(3.113) can be used on each layer. Notice that the relations should also apply to the final relations between the overall transmission and reflection coefficients. The S matrices of the layers are,

$$S_X = \begin{bmatrix} t_{12} & r_{21} \\ r_{12} & t_{21} \end{bmatrix} \qquad S_Y = \begin{bmatrix} e^{-i\phi} & 0 \\ 0 & e^{-i\phi} \end{bmatrix} \qquad S_Z = \begin{bmatrix} t_{23} & r_{32} \\ r_{23} & t_{23} \end{bmatrix} \tag{3.118}$$

Rearranging these into corresponding M matrices and multiplying, results in a total wave-transfer matrix of,

$$M_T = \frac{1}{t_{21}t_{32}} \begin{bmatrix} t_{23}t_{32} - r_{23}r_{32} & r_{32} \\ -r_{23} & 1 \end{bmatrix} \begin{bmatrix} e^{-i\phi} & 0 \\ 0 & e^{i\phi} \end{bmatrix} \begin{bmatrix} t_{12}t_{21} - r_{12}r_{21} & r_{21} \\ -r_{12} & 1 \end{bmatrix} \tag{3.119}$$

$$= \frac{e^{i\phi}}{t_{21}t_{32}} \begin{bmatrix} \theta_1\theta_2 e^{-2i\phi} - r_{12}r_{32} & \theta_2 r_{21} e^{-2i\phi} + r_{32} \\ -\theta_1 r_{23} e^{-2i\phi} - r_{12} & 1 - r_{23}r_{21}e^{-2i\phi} \end{bmatrix}, \tag{3.120}$$

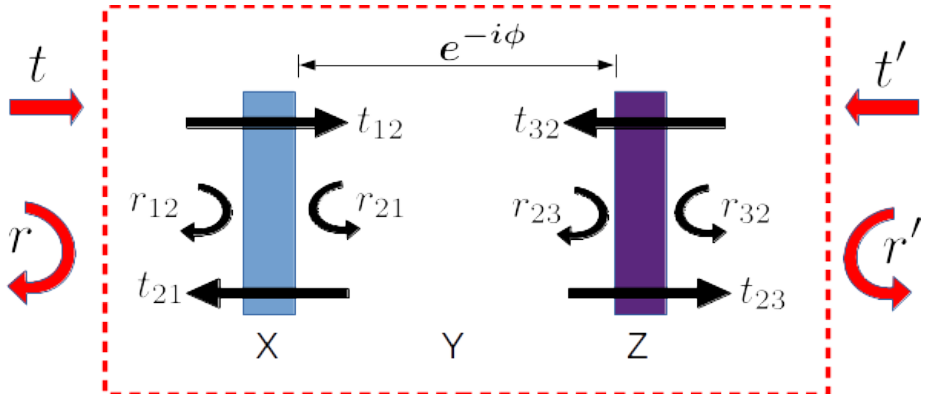

Figure 3.9: Fabry-Perot to be modeled. It is broken into 3 sections, X, Y, and Z that each have their own matrix. The end layers are assumed to be multilayer systems themselves such that the reflection and transmission coefficients are complex. The middle, Y, layer is simple propagation. It is assumed that each layer is lossless and begins and ends in the same media such that the relations (3.110)-(3.113) can be used. Once the matrices are cascaded, the FP can be treated as a black box with transmission and reflection coefficients of t,t',r and r' as shown in red.

where the placeholders, $\theta_1 = t_{12}t_{21} - r_{12}r_{21}$, and $\theta_2 = t_{23}t_{32} - r_{23}r_{32}$, have been used. Eq. (3.98) is used to convert to the final transmission, (t,t') and reflection coefficients, (r,r') for the fabry-perot.

$$r = -\frac{C}{D} = \frac{(t_{12}t_{21} - r_{12}r_{21})r_{23}e^{-2i\phi} + r_{12}}{1 - r_{21}r_{23}e^{-2i\phi}} \tag{3.121}$$

$$= r_{12} + \frac{t_{12}t_{21}r_{23}e^{-2i\phi}}{1 - r_{21}r_{23}e^{-2i\phi}} \tag{3.122}$$

$$r' = \frac{B}{D} = \frac{(t_{23}t_{32} - r_{23}r_{32})r_{21}e^{-2i\phi} + r_{32}}{1 - r_{21}r_{23}e^{-2i\phi}} \tag{3.123}$$

$$= r_{32} + \frac{t_{23}t_{32}r_{21}e^{-2i\phi}}{1 - r_{21}r_{23}e^{-2i\phi}} \tag{3.124}$$

$$t = \frac{t_{12}t_{23}e^{-i\phi}}{1 - r_{21}r_{23}e^{-i2\phi}} \tag{3.125}$$

$$t' = \frac{t_{21}t_{32}e^{-i\phi}}{1 - r_{21}r_{23}e^{-i2\phi}}. \tag{3.126}$$

These equations are fully general in the sense that no stokes relations have been used. These are sometimes referred to as Airy's summation formulas for a FP. Note that all of the variables are complex due to the end X,Y layers being made up of layered

media themselves.

Notice that, in this general case, there is nothing to force the relationship $|r|^2 = |r'|^2$. Experimentally this means, due to there being no explicit phase relationship between the reflection coefficients, that the orientation of a Gires-Tournois interferometer in relation to incoming light matters [4]. Whether the light encounters the high reflectivity face first, or last, effects the quantity and sign of aggregated transfer phase.

Repeated Element Fabry-Perot

If layers X and Z are identical, then $r_{12} = r_{23} = r_1$, $r_{21} = r_{32} = r_2$, $t_{12} = t_{23} = t_1$, and $t_{21} = t_{32} = t_2$. This simplifies Eqs. (3.121)-(3.126) to,

$$r = \frac{(t_1 t_2 - r_1 r_2) r_1 e^{-2i\phi} + r_1}{1 - r_1 r_2 e^{-2i\phi}} \tag{3.127}$$

$$= r_1 + \frac{t_1 t_2 r_1 e^{-2i\phi}}{1 - r_1 r_2 e^{-2i\phi}} \tag{3.128}$$

$$r' = \frac{(t_1 t_2 - r_1 r_2) r_2 e^{-2i\phi} + r_2}{1 - r_1 r_2 e^{-2i\phi}} \tag{3.129}$$

$$= r_2 + \frac{t_1 t_2 r_2 e^{-2i\phi}}{1 - r_1 r_2 e^{-2i\phi}} \tag{3.130}$$

$$t = \frac{t_1 t_1 e^{-i\phi}}{1 - r_1 r_2 e^{-i2\phi}} \tag{3.131}$$

$$t' = \frac{t_2 t_2 e^{-i\phi}}{1 - r_1 r_2 e^{-i2\phi}}. \tag{3.132}$$

These equations can be simplified further by separating each term into its amplitude and phase as $t_1 = |t_1| e^{i\phi_{t1}}$, $t_2 = |t_2| e^{i\phi_{t2}}$, $r_1 = |r_1| e^{i\phi_{r1}}$, and $r_2 = |r_2| e^{i\phi_{r2}}$. Relations (3.110)-(3.113) can be rewritten in terms of this updated notation as,

$$|r_1| = |r_2| \tag{3.133}$$

$$|t_1| = |t_2| \tag{3.134}$$

$$|t_1|^2 + |r_1|^2 = 1 \tag{3.135}$$

[4] A Gires-Tournios interferometer is simply a fabry-perot etalon interferometer with a single high reflectivity coated face.

$$e^{i\phi_{t1}+i\phi_{t2}} = -e^{i\phi_{r1}+i\phi_{r2}} \tag{3.136}$$

Using these simplications, r and t can be simplified to,

$$t = \frac{(1-|r_1|^2)e^{-i\phi+i2\phi_{t1}}}{1-|r_1|^2 e^{-i2\phi+i\phi_{r1}+i\phi_{r2}}} \tag{3.137}$$

$$r = \frac{r_1(1-e^{-2i\phi+i\phi_{r1}+i\phi_{r2}})}{1-|r_1|^2 e^{-i2\phi+i\phi_{r1}+i\phi_{r2}}}. \tag{3.138}$$

Substituting $\delta = -2\phi$ leads to,

$$t = \frac{(|r_1|^2-1)e^{i\delta/2+i2\phi_{r1}+i2\phi_{r2}-i2\phi_{t2}}}{1-|r_1|^2 e^{i\delta+i\phi_{r1}+i\phi_{r2}}} \tag{3.139}$$

$$r = \frac{r_1(1-e^{i\delta+i\phi_{r1}+i\phi_{r2}})}{1-|r_1|^2 e^{i\delta+i\phi_{r1}+i\phi_{r2}}}. \tag{3.140}$$

Now if it is assumed that $t1$ and $t2$ are fully real ($\phi_{t1} = \phi_{t2} = 0$), then through Eq. (3.136) we know that, $\phi_{r1} + \phi_{r2} = \pi$, which leads to a further simplication of,

$$t = \frac{(|r_1|^2-1)e^{i\delta/2}}{1+|r_1|^2 e^{i\delta}} \tag{3.141}$$

$$r = \frac{r_1(1+e^{i\delta})}{1+|r_1|^2 e^{i\delta}}. \tag{3.142}$$

Notice that the expression for r can be achieved directly by setting $(t_1t_2 - r_1r_2) = 1$ in Eq. (3.127).

Symmetric Fabry-Perot

A symmetric FP doesn't simply repeat the first matrix element, but flips it around such that light encounters the interfaces in the same order regardless of input propagation direction. In this case we set $r_{12} = r_{32} = r_1$, $r_{21} = r_{23} = r_2$, $t_{12} = t_{32} = t_1$, and $t_{21} = t_{23} = t_2$ in Eqs. (3.121)-(3.126). This simplifies to,

$$r = r' = \frac{(t_1t_2 - r_1r_2)r_2e^{-2i\phi} + r_1}{1-r_2^2e^{-2i\phi}} \tag{3.143}$$

$$= r_1 + \frac{t_1t_2r_2e^{-2i\phi}}{1-r_2^2e^{-2i\phi}} \tag{3.144}$$

$$t = t' = \frac{t_1 t_2 e^{-i\phi}}{1 - r_2^2 e^{-i2\phi}} \tag{3.145}$$

Eqs.(3.133)-(3.136) are still valid as written so using them as well as separating the terms into phasor notation and substituting $\delta = -2\phi$ leads to,

$$r = r' = \frac{r_1 - r_2 e^{i\delta + i\phi_{r1} + i\phi_{r2}}}{1 - r_2^2 e^{i\delta}} \tag{3.146}$$

$$= \frac{r_1(1 - e^{i\delta + i2\phi_{r2}})}{1 - r_2^2 e^{i\delta}} \tag{3.147}$$

$$t = t' = \frac{(1 - |r1|^2) e^{i\delta/2 + i\phi_{t1} + i\phi_{t2}}}{1 - r_2^2 e^{i\delta}}. \tag{3.148}$$

In order to recover the expressions shown in the textbook, we must simply assume that $\phi_{t1} = \phi_{t2} = 0$, which implies through Eq. (3.136) that

$$r = r' = \frac{r_1 + r_2 e^{i\delta}}{1 - r_2^2 e^{i\delta}} \tag{3.149}$$

$$= \frac{r_1(1 - e^{i\delta - 2i\phi_{r1}})}{1 - r_2^2 e^{i\delta}} \tag{3.150}$$

$$t = t' = \frac{(1 - |r1|^2) e^{i\delta/2}}{1 - r_2^2 e^{i\delta}}. \tag{3.151}$$

3.4 Conclusion

It has been shown that an IPI laser can succesfully be modelled as a coupled two-level system in time or frequency. These simulations clearly show how two circulating pulses in a cavity result in two shifted frequency combs that have CEO's shifted proportionally to the applied detuning. Further, it was shown that by removing coupling from such a system, the dead-band can be eliminated. Last, an explicit discussion was included of what it means to have conservative or non-conservative coupling in terms of the coupling (or reflection) parameter.

Note that much confusion seems to arise regarding the correct form of the coupled-mode equations. Most of this confusion is due to different forms of notation being used.

Thus, Appendix A has been included which reiterates the derivation of Section 3.2 while including the many different ways that equivalent mathematical representations can appear in different publications.

Chapter 4

Intracavity Phase Interferometry: Experimental Implementation

4.1 Introduction

The most familiar implementation of IPI is that of the ring laser gyroscope. When two electric-fields counter-propagate in a rotating ring, the Sagnac effect causes a frequency detuning to occur that is proportional to the ring rotation rate [27, 28]. All commercial gyroscopes today use cw light. The problem with cw light is that there exists coupling everywhere within the ring between the counter-propagating fields. This coupling leads to a dead-band where mutual injection scattering causes the two electric field frequencies to lock together at low rotation rates and destroy the measurement. With cw light, this coupling is unavoidable, and clever technological tricks have been created to curb the issue (for example mechanical dithering [29]). Pulsed light, however, has limited spatial extent and therefore will only overlap in two locations within the ring which limits coupling. By also cross-polarizing the light, the coupling between the fields is effectively removed which, in theory, leads to the holy grail of gyrosocopes: a highly sensitive, dead-band free, linear response rotation sensor. More importantly, switching to pulsed light allows the linear analog to a laser gyroscope to exist which extends the technique's measurement from just angular

acceleration to any physical phenomenon that can change the optical phase of light (linear acceleration, displacement, index of refraction, magnetic field, etc.). As can be seen in the linear configuration example of Fig. 4.1, this involves an intracavity Michelson interferometer where one lasing arm serves as a reference, while the other probes the physical parameter to be measured.

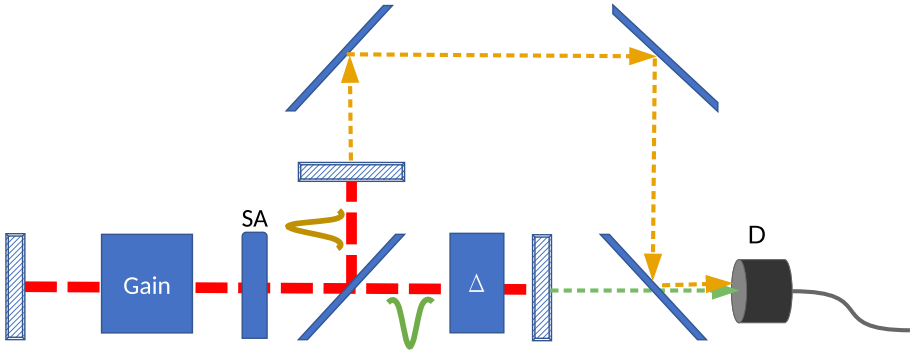

Figure 4.1: Linear IPI configuration. Two pulses (orange and green) are lasing in the cavity. Passive mode-locking is induced by the saturable absorber (SA). Because the physical parameter to be measure, Δ, only affects the green pulse, a beat frequency is observed when the pulses are overlapped in time on the external detector, D.

Free-space proof of concept IPI lasers have been successfully constructed in the past [30]. However, any viable sensor must be able to operate outside of a lab environment – an obvious difficulty for free-flowing carcinogenic dye-jet based lasers. Fiber lasers are an attractive solution as they are compact, scalable, and more easily shielded from environmental noise. The first fiber optic IPI laser was recently realized [4]. To improve on that design, it was decided to replace the gain mechanism with optical parametric oscillation (OPO). This allowed the ability to synchronously pump the IPI laser – removing the mode-locking element from the sensing cavity. This change reduces the number of scattering elements inside the laser cavity which removes the opportunity for injection locking and reduces the bias by allowing a more symmetric cavity. Due to the phase sensitive nature of degenerate parametric amplification, the choice of using OPO also primes the device for future quantum squeezing enhancement.

4.2 Optical Parametric Oscillation

An optical parametric oscillator is similar to a classic laser oscillator except that the gain medium has been replaced by a nonlinear parametric process which, in this case, happens to be partially degenerate four-wave mixing [1]. Partially degenerate four-wave mixing is a $\chi^{(3)}$ process where two identical pump photons of frequency, Ω_p, are converted into an up frequency shifted photon (sometimes called the idler, Ω_i) and a down frequency shifted photon (sometimes called the signal, Ω_s). Through conservation of energy,

$$2\Omega_p = \Omega_s + \Omega_i, \tag{4.1}$$

the signal and idler photons are equal distance from the pump in frequency space, $\Delta\Omega = \Omega_p - \Omega_s = \Omega_i - \Omega_p$. This process differs from Raman scattering in that it is mediated by quantum virtual levels and so is effectively instantaneous and not restricted to explicit material energy levels.

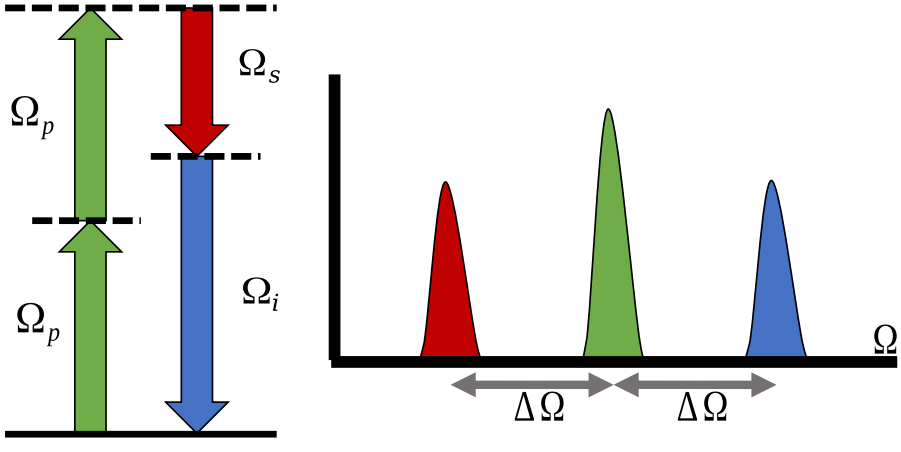

Figure 4.2: Left: Degenerate four-wave mixing converts two identical pump photons of frequency Ω_p into a down converted signal photon Ω_s, and an up-converted Ω_i photon. The dashed lines represent virtual energy levels. Right: Conservation of energy causes the signal and idler photons to be equidistant from the pump in frequency space.

[1] Confusingly, partially degenerate four-wave mixing used to be called three-wave mixing since only three distinct frequencies are involved [31], however three-wave mixing is now reserved for $\chi^{(2)}$ processes where three photons mediate the interaction.

4.2.1 General Considerations

Parametric four wave mixing has been described in detail elsewhere [32–34], so only an abbreviated description will be given here. The effect is caused by the nonlinear response of a material to an incoming electromagnetic field. How a material responds to an incoming electromagnetic field is summed up in a variable called the susceptibility, χ. Due to a material's symmetries and dispersion it is often convenient to expand χ in a power series, where the first order ($\chi^{(1)}$) is related to the index of refraction, and higher orders ($\chi^{(2)}$, $\chi^{(3)}$, etc.) define the nonlinear effects. Optical fiber is made from silica glass which is an isotropic material (it is symmetric along all 3 spatial axes). This fact leads to nonlinear optical fiber phenomena to be dominated by the $\chi^{(3)}$ process since the $\chi^{(2)}$ term vanishes in isotropic materials.

Instead of pumping a gain material and creating gain through stimulated emission, an OPO laser creates gain by directly converting 2 pump photons into a signal and idler photon. When the conversion occurs, if there is already signal (or idler) photons hanging around (either from vacuum fluctuations, or a seed laser), then the signal (or idler) beam experiences gain. In order for efficient energy transfer to occur, a specific phase relation between the photons must exist,

$$2k_p = k_s + k_i, \tag{4.2}$$

where k is the *effective* propagation constant. It is an effective parameter not exactly given by the sellmeier equations because in fiber there are additional terms from nonlinear and waveguiding dispersion[2]. The amplification factor for a non-depleted, single-frequency pump, four-wave mixing process is given by [32],

$$G_s = 1 + \left(\frac{\gamma P_0}{g}\right)^2 \sinh^2(gL), \tag{4.3}$$

where P_0 is the pump power, γ is the average nonlinear coefficient defined for the material, $g = \sqrt{(\gamma P_0)^2 - (\kappa/2)^2}$ is the parametric gain, and $\kappa = \Delta k + 2\gamma P_0$ is the

[2]To emphasize that this is an effective propagation constant the fiber community typically uses β in place of k.

effective phase mismatch between the pump, idler and signal waves with,

$$\Delta k = k_s + k_i - 2k_p. \tag{4.4}$$

Clearly, gain is maximized when $\kappa = 0$. The $2\gamma P_0$ term is caused by self and cross phase modulation and causes the phase mismatch to be affected by the pump power. If the pump depletes as it traverses the gain material, then the phase mismatch term changes along the length of the fiber which can cause energy to be passed back from the idler and signal to the pump. While energy conservation governs what frequencies are allowed to be created through $2\Omega_p = \Omega_s + \Omega_i$, it is the phase matching equation that governs how much energy flows from the pump to the signal and idler frequencies. L is the effective gain length and is more complicated to define than one might expect, as will be explained below.

Dispersion in the fiber results in different frequencies traveling at different velocities. Since we are dealing with short pulses in this case, the signal, idler, and pump all travel at slightly different velocities and thus are only overlapped in space for a specific amount of time (or equivalently length of gain fiber). This is known as temporal walk-off, and it means that the gain length is not always equal to the length of OPO gain fiber. By pumping the OPO near the zero-dispersion wavelength of a specific fiber, temporal walk-off is minimized. While dispersion also leads to chirp induced pulse broadening, this does not improve the pump and signal overlap since the underlying longitudinal modes are still walking off from one another.

The last consideration is that of synchronous pumping. Parametric gain only occurs when all three (pump, signal, and idler) pulses are overlapped in time. For lasing to occur, then, the parametric pulse must be timed such that it overlaps with a pump pulse in the gain medium every round-trip. In other words, the pump repetition rate must match (to within a pulse length [3]) the repetition rate of the parametric pulse in the OPO cavity. If this is achieved, then the parametric pulse will experience positive feedback and gain can lead to lasing. This precise matching

[3]For a 1ps pulse in air this correspond to about 300μm. A typical fiber splice requires the removal of at least 1-2cm of fiber, which is why the inclusion of a delay-line is necessary.

of fiber cavity lengths between the pump oscillator and OPO cavity is the most challenging experimental hurdle when developing synchronous OPO lasers.

4.2.2 Phase mismatch calculation

The calculation of Eq. 4.4 is not as straight forward as that notation suggests due to the fact fiber manufacturers do not typically publish curves of $k(\Omega)$. Thus, we pause here to describe how different estimations are carried out in practice given what information is provided.

Since there is a fixed relationship between the signal and idler (with the pump frequency being fixed), Eq. 4.4 can be rewritten as,

$$\Delta k(\omega_i) = k(\omega_i) + k(2\omega_p - \omega_i) - 2k(\omega_p), \tag{4.5}$$

assuming we are ultimately interested in oscillating the idler. Expanding k in a Taylor series around an arbitrary point ω_0 leads to,

$$k(\Omega)|_{\omega_0} = k_0 + (\Omega - \omega_0)k_1 + \frac{1}{2}(\Omega - \omega_0)^2 k_2 + \frac{1}{6}(\Omega - \omega_0)^3 k_3 + \frac{1}{24}(\Omega - \omega_0)^4 k_4 + \frac{1}{120}(\Omega - \omega_0)^5 k_5 + ..., \tag{4.6}$$

where $k_m = \frac{\partial^m k}{\partial \Omega^m}\Big|_{\omega_0}$ $(m = 0, 1, 2, ...)$ which means that the k_m's are a function of the chosen expansion frequency. This can then be plugged back into Eq. 4.5 (dropping higher order terms) which simplifies to,

$$\Delta k(\omega_i) = \frac{1}{2}\left[(\omega_i - \omega_0)^2 + (2\omega_p - \omega_i - \omega_0)^2 - 2(\omega_p - \omega_0)^2\right] k_2 + \frac{1}{6}\left[(\omega_i - \omega_0)^3 + (2\omega_p - \omega_i - \omega_0)^3 - 2(\omega_p - \omega_0)^3\right] k_3. \tag{4.7}$$

Note that the fiber community typically doesn't use the group velocity dispersion (GVD) parameter, k_2 [fs^2/mm], but the Dispersion, D [ps/(nm $*$ km], parameter instead. The D parameter was contrived to allow technicians laying fiber to more easily calculate the group delay ($\Delta\tau$) between pulses with a wavelength spacing of $\Delta\lambda$ as, $\Delta\tau = D\Delta\lambda L$, where L is the length of fiber under consideration. This results

in it being similar to the GVD parameter except that the last derivative is taken in terms of wavelength instead of frequency, $D = \frac{\partial}{\partial\lambda}\frac{\partial k}{\partial\Omega}$, and thus are related through,

$$k_2 = -\frac{\lambda_0^2}{2\pi c}D(\lambda_0). \tag{4.8}$$

The D parameter is then related to the third order dispersion term by [33],

$$k_3 = \left(\frac{\lambda_0^2}{2\pi c}\right)^2\left(\frac{2}{\lambda_0}D(\lambda_0) + \frac{\partial D}{\partial\lambda}\Big|_{\lambda_0}\right). \tag{4.9}$$

Implementing this adjustment in Eq. 4.7 results in,

$$\Delta k(\omega_i) = -\frac{\lambda_0^2}{2\pi c}(\omega_p-\omega_i)^2\left[D(\lambda_0) - \frac{\lambda_0^2}{2\pi c}\left(\frac{2}{\lambda_0}D(\lambda_0) + \frac{\partial D}{\partial\lambda}\Big|_{\lambda_0}\right)(\omega_p-\omega_0)\right], \tag{4.10}$$

or equivalently,

$$\Delta k(\nu_i) = -\frac{2\pi\lambda_0^2}{c}(\nu_p-\nu_i)^2\left[D(\lambda_0) - \frac{\lambda_0^2}{c}\left(\frac{2}{\lambda_0}D(\lambda_0) + \frac{\partial D}{\partial\lambda}\Big|_{\lambda_0}\right)(\nu_p-\nu_0)\right], \tag{4.11}$$

which converting to all wavelength notation results in,

$$\Delta k(\lambda_i) = -\frac{2\pi c\lambda_0^2}{\lambda_p^2\lambda_i^2}(\lambda_i-\lambda_p)^2\left[D(\lambda_0) - \frac{\lambda_0}{\lambda_p}\left(\frac{2}{\lambda_0}D(\lambda_0) + \frac{\partial D}{\partial\lambda}\Big|_{\lambda_0}\right)(\lambda_0-\lambda_p)\right]. \tag{4.12}$$

Care must be taken when converting between D and GVD notation as there seems to be some confusion as to what is the correct expression when comparing different papers [35–37], however, clarity can be found in [33]. Eq. 4.12 is useful because it allows the phase mismatch for a specific set of pump and idler (and therefore signal) wavelengths to be estimated based on only the dispersion parameter, D, and dispersion slope, $\partial D/\partial\lambda$, at a single operating wavelength, which are parameters typically published by fiber manufacturers. Eq. 4.3 can then be used to estimate where the OPO will see the highest gain.

One common way to simplify Eq. 4.12 is to assume that the expansion is done at the zero dispersion wavelength such that $D(\lambda_0) = 0$ [36–38]. This results in,

$$\Delta k(\lambda_i) = -\frac{2\pi c\lambda_0^3}{\lambda_p^3\lambda_i^2}(\lambda_p-\lambda_i)^2\frac{\partial D}{\partial\lambda}\Big|_{\lambda_0}(\lambda_p-\lambda_0), \tag{4.13}$$

where now all that is required to estimate the phase mismatch for a given idler, λ_i, and pump, λ_p, wavelength, is the zero dispersion wavelength, λ_0, and the dispersion

slope at that wavelength, $\partial D/\partial\lambda|_{\lambda_0}$. A different simplification is instead to expand around the pump wavelength such that, $\lambda_0 = \lambda_p$, which simplifies Eq. 4.12 to [33],

$$\Delta k(\lambda_i) = -\frac{2\pi c}{\lambda_i^2}(\lambda_i - \lambda_p)^2 D(\lambda_p). \tag{4.14}$$

If the idler frequency excursion from the pump is greater than a few nanometers, however, this equation becomes less accurate and higher order terms are needed in the expansion of Eq. 4.7. In fact, if one takes $\omega_0 = \omega_p$ in Eq. 4.7, all of the odd terms drop out such that,

$$\Delta k(\omega_i) = (\omega_p - \omega_i)^2 k_2 + \frac{1}{12}(\omega_p - \omega_i)^4 k_4 + \frac{1}{360}(\omega_p - \omega_i)^6 k_6 + ... \tag{4.15}$$

If one is lucky enough to posess a full dispersion curve, $D(\lambda)$, for a specific fiber, a sometimes more accurate calculation can be carried out by making a polynomial fit of the dispersion curve, and using Eq. 4.15 directly in Eq. 4.3. [39–44].

Describing this latter process more explicitly, one first digitizes the $D(\lambda)$ curve given by the fiber company. This dispersion parameter curve is then converted to the GVD parameter, $k_2(\omega)$. Next, a polynomial fit of $k_2(\omega)$ is made such that,

$$k_2(\omega) = a\omega^4 + b\omega^3 + c\omega^2 + d\omega + e. \tag{4.16}$$

All higher order dispersion coefficients can then be calculated by taking derivatives,

$$k_3(\omega) = \frac{\partial k_2}{\partial \omega} = 4a\omega^3 + 3b\omega^2 + 2c\omega + d \tag{4.17}$$

$$k_4(\omega) = \frac{\partial k_3}{\partial \omega} = 12a\omega^2 + 6b\omega + 2c \tag{4.18}$$

$$k_5(\omega) = \frac{\partial k_4}{\partial \omega} = 24a\omega + 6b \tag{4.19}$$

$$k_6(\omega) = \frac{\partial k_5}{\partial \omega} = 24a. \tag{4.20}$$

The even coefficients are then calculated at the chosen pump expansion frequency, ω_p, and plugged into Eq. 4.15 to obtain an estimation for the phase mismatch. Knowing the phase mismatch, an estimation of the OPO gain profile can be deduced from Eq. 4.3 by plugging in values for gain length, pump pulse peak intensity, and the nonlinear coefficient of the fiber. That gain profile is then used to choose a wavelength to lase so that fiber components can be purchased.

4.3 Ring cavity configuration

A free space OPO IPI has been successfully constructed in the past [45], however, the goal of this dissertation was to move that device into fiber similar to [46]. In order to design the laser cavity, it must be known which wavelengths will be involved. Initially it was assumed that it would be easier to use a commercial pump laser instead of building one from scratch.

4.3.1 The 1030nm source

An Ekspla FF1000 Yb:YAG 80fs 30MHz 1030nm 1.5W commercial laser was used as the pump oscillator. Several nonlinear gain fibers were considered. Ultimately the NKT photonics SC-5-1040-PM photonic crystal fiber was chosen due to its beneficial dispersion characteristics. Photonic crystal fibers are unique in that their waveguiding is not solely from total internal reflection but also photonic bandgap guiding caused by a microstructed core [47]. Photonic crystal fibers have become popular in nonlinear optics due to the ability to tailor their dispersion by adjusting the size and gaps of the structured core [48, 49].

Following the procedure described in section 4.2.2, the dispersion curve published for the chosen NKT photonic crystal fiber was digitized and the following dispersion coefficients were extracted from the fit at the pump wavelength of 1030nm: $k_2 = 0.132 \times 10^6 \frac{\text{fs}^2}{\text{km}}$, $k_4 = -100.88 \times 10^6 \ \frac{\text{fs}^4}{\text{km}}$, and $k_6 = -839.7 \times 10^6 \ \frac{\text{fs}^6}{\text{km}}$. Using these parameters along with a gain length of 10cm, average power of 80mW, and the parameters from the Ekspla laser described above resulted in the gain profile shown in Figure 4.3. Assuming the longer wavelength is to be oscillated, the peak gain for the four-wave mixing process is shown to be around 1150nm. There are several caveats with this rather straightforward estimation of the gain curve. First, Eq. 4.3 shows that the gain can be significantly changed by adjusting the gain length and pump power. In general, a shorter length of gain fiber allows for a broader gain bandwidth and increasing pump power increases the phase mismatch (though this

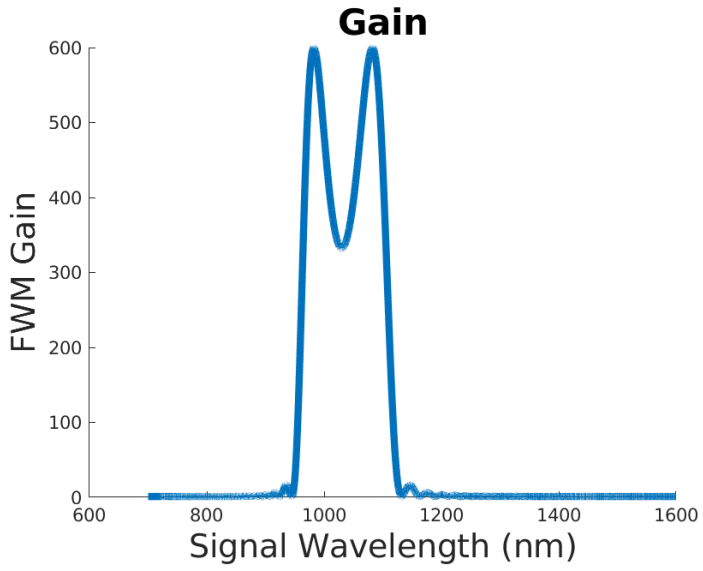

Figure 4.3: Four-wave mixing gain profile estimated from Eq. 4.3, using the dispersion coefficients from the NKT SC-5-1040-PM fiber, peak power of 164000 Watts, nonlinear coefficient of 11.1 $W^{-1}km^{-1}$, gain length of 10cm, and pump wavelength of 1030nm.

depends on if the pump wavelength is in the normal or anamolous portion of the dispersion curve of the gain fiber). More concerning is the sensitivity of the extracted dispersion coefficients to the specific dispersion curve used and the zero dispersion wavelength. Inconsistencies in the manufacturing fiber draw process leads to variations in the location of the zero dispersion wavelength along the fiber. This results in the dispersion of a specific fiber to possibly vary significantly from the published dispersion curve. This is all to say that without having a way to explicitly measure the dispersion of a specific length of fiber (an involved experiment in and of itself), the theoretical gain curve cannot be entirely trusted.

Nonetheless, the theoretical curve allows the ability to make a first guess and obtain fiber components that might work. Figure 4.4 shows the initial design for the bidirectional fiber optic parametric oscillator (BiFOPO). The Ekspla pump laser is first coupled from free-space into fiber where the 1030nm pulses are split by a 50/50 splitter into two different paths. The two pump pulses are then sent into counterpropagating directions in the bottom OPO loop by way of the wavelength division multiplexor (WDM). The WDM is a fiber bragg grating based component

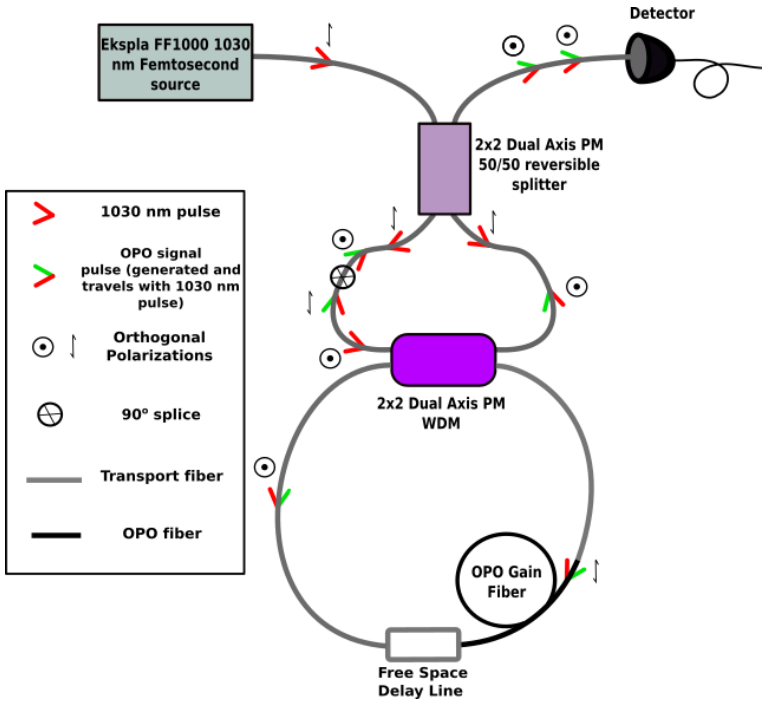

Figure 4.4: Initial design plan for the ring bidirectional fiber optic parametric oscillator. The transport fiber is a PANDA PM980 polarization maintaining fiber. The OPO gain fiber is the NKT SC-5-1040-PM polarization maintaining supercontinuum fiber. The Wavelength Division Multiplexor (WDM) reflects the 1030nm pump into the loop while transmitting most of the 1150nm OPO pulse power. It also acts as an output coupler by leaking a small amount of the OPO bakc out of the loop. Because of the symmetry of the design the lasing OPO pulses are automatically overlapped in time on the output detector for beat note detection. The placement of the 90 degree splice forced the counter-propagating pulses to be cross-polarized in the lasing loop while maintaining the same polarization on the output detector for interference.

that operates similarly to a dichroic mirror. In this case the WDM reflects the 1030nm pump and transmits the 1150nm OPO signal wavelength. Notice that in this configuration the WDM is also acting as an output coupler. To do this, it is designed to be a "bad" component such that it leaks a bit of the 1150nm signal into the reflection arm. This is done so that when the leaked OPO signal output (from both lasing directions) makes its way back up to the 50/50 splitter, the pulses will automatically be overlapped in time on the output detector for beat frequency detection. This removes the need for an external beatnote detection delay apparatus. The bottom loop is where the OPO gain fiber (chosen to be the NKT photonic crystal

fiber) causes the four-wave mixing conversion that leads to lasing after feedback through the WDM. Recall that the pump pulse must exactly overlap the generated OPO pulse every round-trip. The free-space delay line allows for the size of the loop to be adjusted with micron precision such that the repetition rate of the OPO pulses can be matched to that of the pump laser, allowing for successful synchronous pumping. Also of note is the fact that all fibers shown are polarization maintaining fibers. By making a 90 degree splice in one of the arms leading to the WDM, the counter-propagating OPO pulses are made to be cross-polarized in the loop. This reduces any stray scattering that may lead to injection locking while still allowing the pulses to be similarly polarized on the detector since the pulses travel the same path in opposite order.

There were several challenges to overcome with this design. First, loss in the cavity had to be managed. The Oz optics commercial ODL-650 free space delay line inherently added 12% loss (measured at 1030nm) due to the coupling to and from fiber, while the Haphit WDM included 27% insertion loss at the pump wavelength. While these seem like high losses, the high gain and long gain lengths that exist in fiber systems can easily make up for significant losses. The last form of loss to be dealt with was the splice loss. Because the gain fiber was a structured core photonic crystal fiber, splicing to step index fibers is a challenge. In order to achieve the least lossy splice, the core size was first decreased by splicing a section of PM780 fiber to the PM980 transport fiber. The PM780 fiber, with smaller core diameter than the PM980, was then spliced to the even smaller core PCF gain fiber. The PCF fiber required a custom splice recipe to be developed since our Fujikura FSM-45PM arc fusion splicer was not programmed to carry out such a splice automatically. An arc fusion splicer is a tool used to join two fibers. The fiber ends are placed between the two electrodes in the splicer. An electrical discharge then arcs between the electrodes, which briefly melts the silica fiber ends and allows them to be merged. By offsetting the arc location towards the side of the smaller core PCF fiber and using several long low-power arcs, the core of the PCF fiber could be slowly enlarged to decrease coupling loss (see Fig. 4.5). A splice loss of 14% was achieved by offsetting the arc

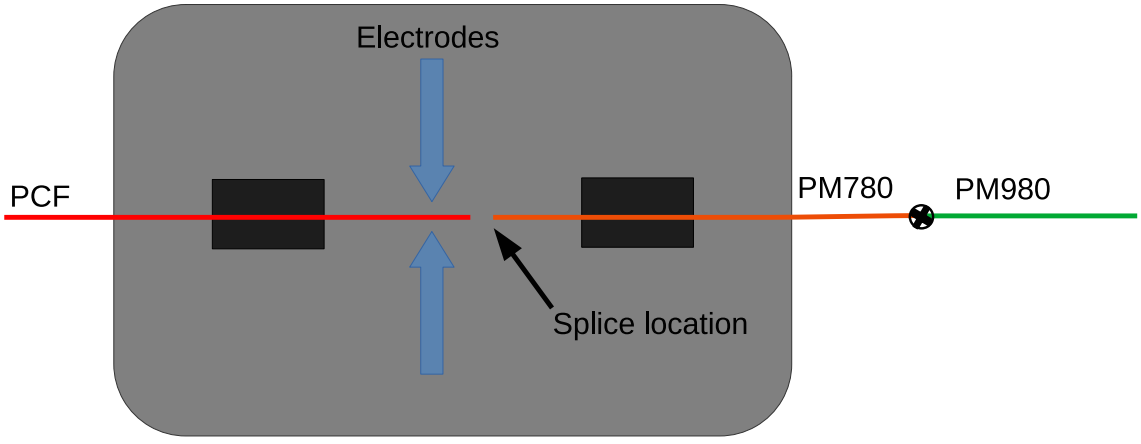

Figure 4.5: Diagram of the method used to splice the photonic crystal fiber (PCF) to the PM980 fiber. First the PM980 fiber was spliced to the PM780 which had a core size closer to the PCF. The PM780 was then spliced to the PCF by offsetting the electrodes from the splice location and repeating long, low power arcs.

location 40um from the center, and arcing around 10 times for 300ms at a power of 0 bits (Fujikura splicing units). By actively monitoring the loss through the splice after each arc, it is easy to find the ideal number of arcs for a specific offset and power.

Another challenge was achieving the synchronous pumping required for externally pumped OPO. Because the precise group delay for the different fibers and components used was not known, the repetition rate between the pump laser and OPO loop had to be matched experimentally. The setup for this measurement is shown in Fig. 4.6. If

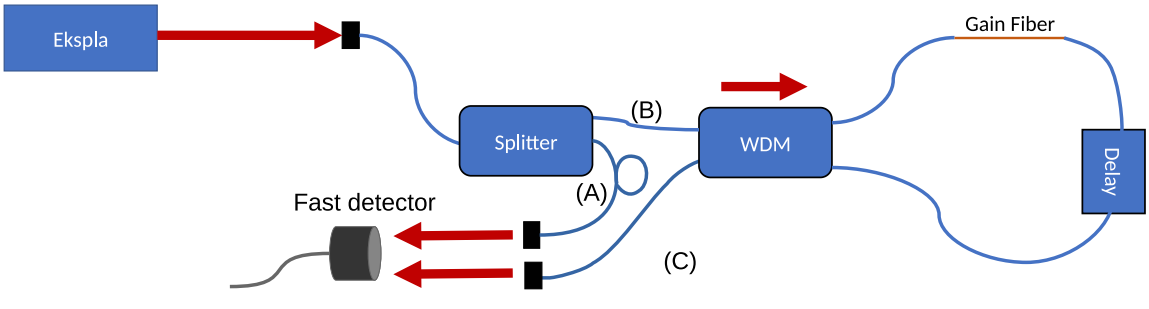

Figure 4.6: Measurement to ensure synchronous pumping. By ensuring the fiber lengths of (B) and (C) added up to the length of fiber (A), the repetition rate of the OPO loop could be matched to that of the Ekspla laser by ensuring the pulses overlapped in time on the fast detector.

the fiber lengths are set such that the lengths follow the relationship, $(A) = (B) + (C)$,

then it can be assumed that the repetition rate of the OPO loop matches that of the Ekspla pump when the two pulses are overlapped in time as measured by the fast detector. The fiber lengths were measured as accurately as possible with string, and the fast detector used had a rise time of 100ps. The OPO loop was built to initially have too much fiber. The minimum amount of fiber that could be cut off at a time in order for an acceptable fiber cleave to occur was about 1cm. So the fiber was cut back 1cm at a time, and the fiber ends were aligned in the splicer. Without actually splicing the fiber ends together, the Ekspla was turned on and the overlap of the two pulses was observed on a fast analog sampling scope. Once the pulses were aligned to within the error of the fiber length measurement, the fibers were spliced and evidence of four-wave mixing was searched for as the delay line was scanned. It was initially unknown how accurately the delay line had to be set for lasing to occur, so a labview program was written that scanned the delay line and measured a spectrum in steps of 0.1ps. If no evidence of OPO was found, then a minimal amount of fiber in the OPO loop was removed and the delay-line was scanned again. This was repeated until a four-wave mixing signal was found.

The four-wave mixing signal that was found is shown in Fig. 4.7. The amplitude normalized plot Fig. 4.7a shows what seems to be promising newly created wavelengths that are separate from the pump, however the unnormalized plot 4.7b tells a different story. While there is clearly some nonlinear interaction occuring, it is difficult to tell whether this is truly wave-mixing that can lead to lasing or just self-phase modulation. The output signal is measured after the WDM which means the signal is what is leaked out of the WDM and therefore could be affected by that transfer function. One thing that is certain is that this is not displaying OPO based lasing.

More pump power was attempted to be squeezed out of the system by removing fiber, re-attempting splices, and improving the Ekspla free-space coupling. Once the power had been maxed out and no lasing was observed, attention was moved to the quality of the pump source. Fig. 4.8 shows an autocorrelation of the commercial Ekspla being used as a pump. The side lobes are indicative of a highly chirped source. This is problematic because the OPO process is highly sensitive to the chirp of the

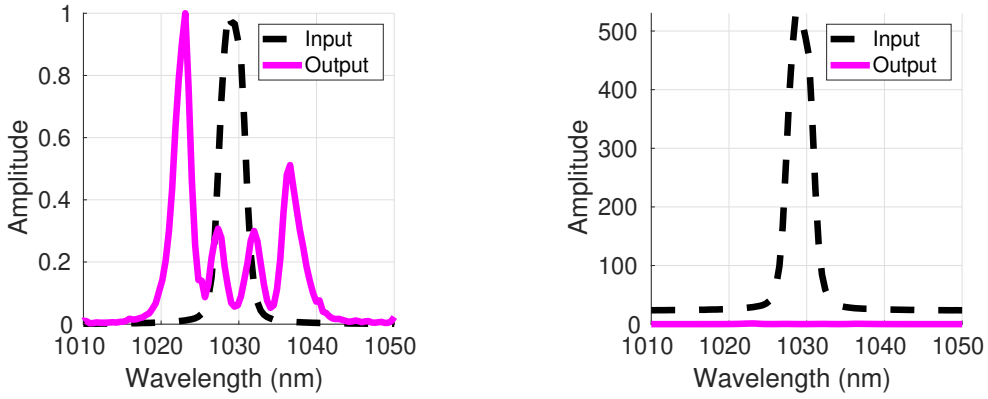

(a) (b)

Figure 4.7: (a) Normalized spectra showing the input pump (black dashed), and the output (solid magenta) showing newly generated wavelengths from nonlinear interaction. The plot in (b) is the same but without normalization showing that the newly generated wavelengths are extremely weak and thus may not be available to generate lasing. Note that the middle two peaks are an artifact from the pump not being fully filtered out of the measurement (they are simply the edge of the pump pulse and not actual peaks).

pump [33]. The chirp decreases the spectral intensity and creates an ambiguity in the pulse duration, which makes defining a peak pulse power difficult. An unknown pump power leads to an uncertainty in defining the four-wave mixing gain. This inability to set the specific fiber component wavelengths with certainty, high loss in the cavity, and inability to change the commercial pump characteristics led to the decision to pivot the plan. It was decided that a home-built pump would enable more flexibility and be better tailored for the task at hand.

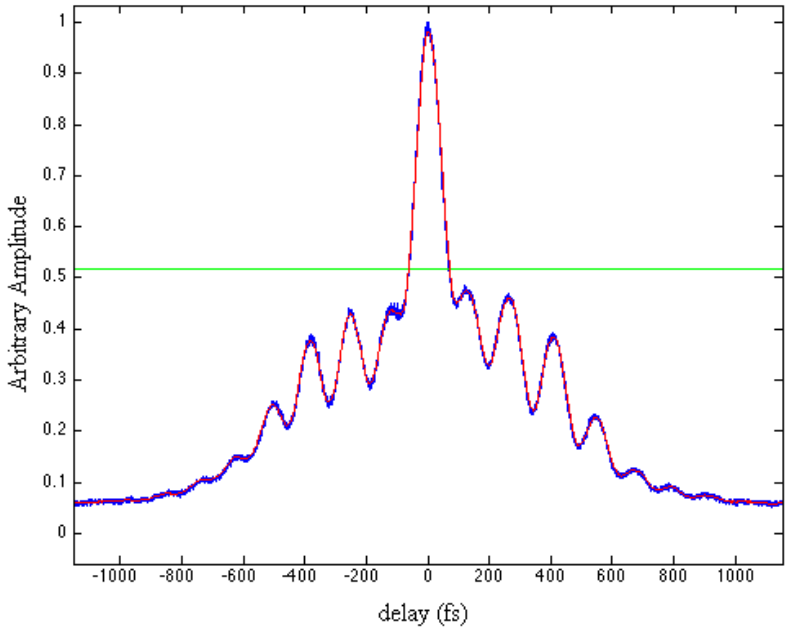

Figure 4.8: Background free autocorrelation of the Ekspla pump laser. The side lobes are indicative of a highly chirped pulse. The green horizontal line displays where the full width half maximumpulse width is calculated from, however, it is clear that a significant portion of this pulse's energy is located in the wings.

4.3.2 The 1550nm source

Since a home-built pump laser was to be constructed, changing the pump wavelength to 1550nm (Erbium based fiber laser) made practical sense. Due to the telecom industry operating mainly at 1550nm, stock commercial parts are widely available and inexpensive. Additionally, extensive research has been done into designing fiber lasers in this wavelength band. Specifically, solid core polarization maintaining highly nonlinear dispersion tailored fibers (HNLF) were available such that the photonic crystal fibers that were inducing high splice loss could be eliminated. The OFS optics HNLF-PM with elliptical core was chosen as the gain fiber due to availability, cost, and beneficial dispersion characteristics. Fig. 4.9 shows the dispersion curve (a), and the calculated pulse walk-off (b) for a guessed OPO pulse center wavelength of 1680nm. The calculation was carried out using the expression in [50] as derived in Appendix B. If the pump pulse is kept above 1ps, then the gain length can be as long

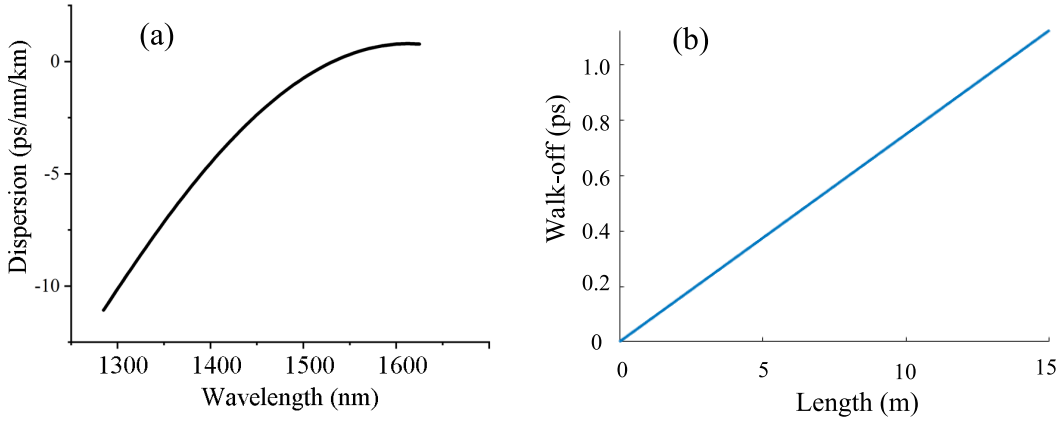

Figure 4.9: Dispersion curve the HNLF used as gain (a), and the corresponding OPO walk-off for a pulse centered at 1680nm (b).

as 10m which is a good sign for creating enough gain to lase in a highly lossy fiber laser.

Erbium fiber lasers can lase at either 1530nm or 1560nm, however, 1560nm is more desireable for mode-locking due to the larger bandwidth. Because the Erbium fiber is more absorbant at 1530nm than it is at 1560nm, 1560nm lasing can be forced by adding longer lengths of gain fiber. The saturable absorber used for mode-locking was composed of carbon nanotubes sandwiched between two FC/APC connectors as described in [4]. A 50/50 solution of distilled water and carbon nantubes is deposited on the connector ferrule (covering the fiber core), and then the water is allowed to evaporate leaving a thin layer of nanotubes. We have found that leaving the oscillator running continuously avoids the initial start-up shock imparted on the saturable absorber and has led to the laser running without maintenance for 19 months and counting.

The oscillator-amplifier chain developed to pump the OPO is shown in Fig. 4.10. Notice that the free-space delay line used to synchronize the OPO loop to the pump was included in the pump oscillator so that the loss that it imparts could be eliminated from the OPO loop. Two types of fiber were used in the oscillator-amplifier chain: standard negative dispersion Corning PM1550 PANDA transport fiber

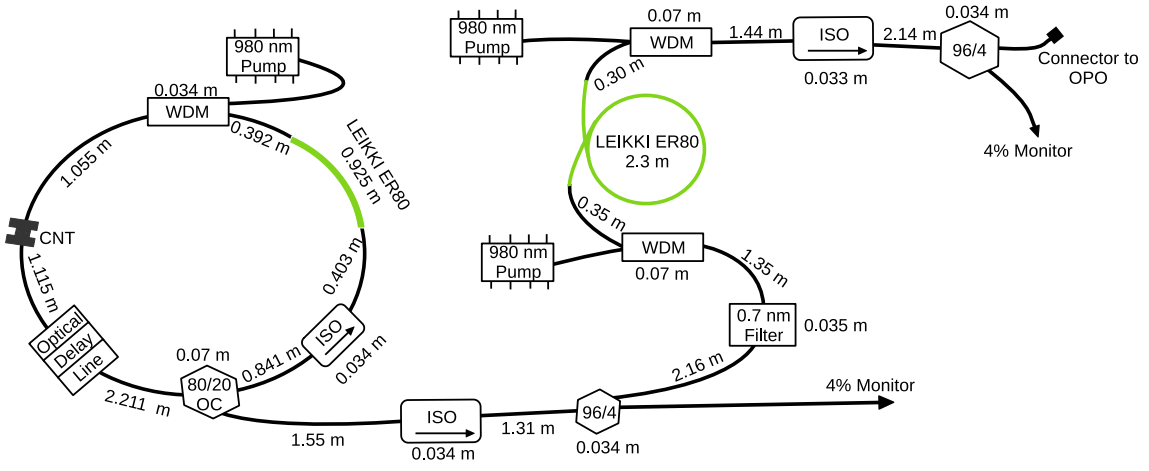

Figure 4.10: Erbium Oscillator-amplifier chain used to pump the OPO sensing loop. This system typically outputs 8ps, 17.7mW (average power) pulses at 29MHz. The components are labelled as follows: WDM = wavelength division multiplexor; ISO = isolator; CNT = carbon nanotube saturable absorber; OC = Output Coupler.

($dk/d\Omega = -22.3$ ps^2/km) and positive dispersion erbium-doped nLight LEIKKI ER80 ($dk/d\Omega = 28.06$ ps^2/km) gain fiber. The oscillator consisted of 615.5cm (including the length of the components) of PM1550 and 92.5cm of LEIKKI such that the total round trip dispersion was -0.11ps^2 (excluding the free space delay). The oscillator mode-locked when the 980nm pump diode was driven with 223mA of current which corresponded to around 130mW of 980nm pumping. This resulted in pulses spaced by around 34.7ns or a 28.75mHz rep rate, 307uW average power output, and a 1.4ps FWHM pulse duration. Fig. 4.11 shows the mode-locked spectrum with the cat's ears that are indicative of stable soliton mode-locking and an unchirped interferometric autocorrelation.

In order to avoid adding chirp from the amplifier and to apply broadening to the pulse in order to increase the walk-off length and facilitate synchronous pumping, a 0.7nm bandpass filter was inserted between the oscillator and amplifier. The bandpass filter also makes the final pulse duration mostly independent of pumping power in the amplifier. Fig. 4.12 shows the amplified pulse without (a) and with (b) the added filter. The linear amplifier is pumped from both directions. When the pump diodes are driven at their typical values of 686mA (LDI driver) and 600mA (Maiman driver),

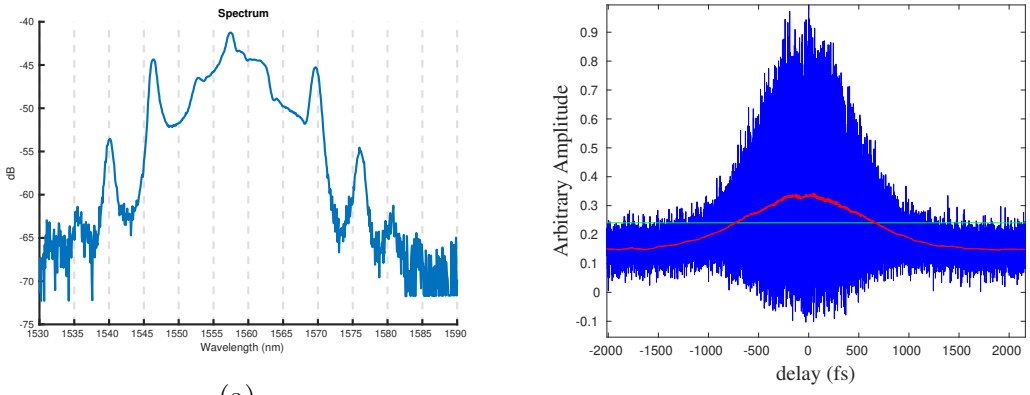

(a) (b)

Figure 4.11: Mode-locked spectrum (a) and autocorrelation (b) of the ring laser erbium oscillator used as pump to the ring IPI configuration. The cat's ears on the spectrum are indicative of stable soliton mode-locking. The interferometric autocorrelation (blue), which is slightly noisy due the electronic amplification necessary to detect the weak pulse, displays an unchirped pulse with FWHM of 1.4ps (green) when averaging down to the intensity autocorrelation (red).

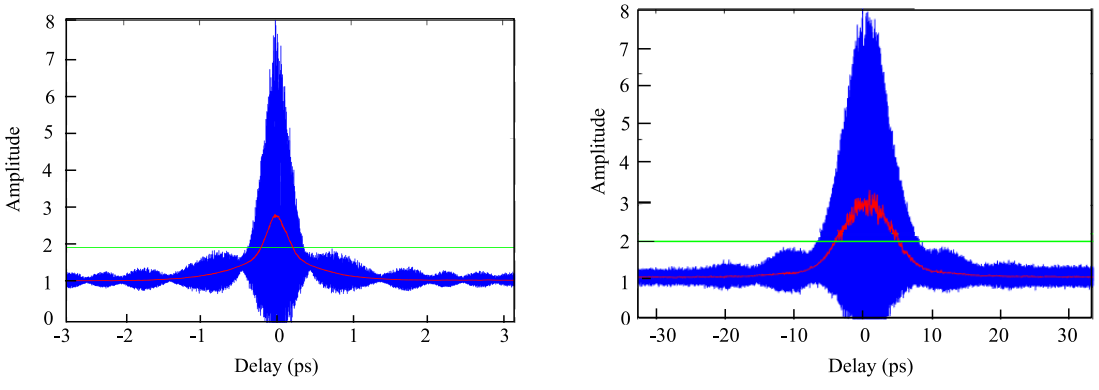

(a) (b)

Figure 4.12: Ring laser pump pulse after amplification without (a) and with (b) implementation of a 0.7 bandpass filter before the amplifier. The amplifier acts to reduce the chirp (seen as wings) and broaden the pulse in time from $<$ 1ps to 8ps FWHM. Without the filter the pulse chirp and duration are highly variable based on how hard the amplifier is pumped. When the filter is added pulse chirp and duration are independent of pumping.

the resultant pulse has an average power of 17.7mW. This pulse is then split almost identically (7.7mW and 7.9mW) into clockwise and counter-clockwise directions with

a 50/50 splitter to pump the OPO sensing loop through a WDM. Evidence of OPO is observed when the average pump power in a single direction reaches above 5mW. Fig. 4.13(a) shows a diagram of the OPO sensing loop, while (b) shows a typical spectrum with the pump at 1560nm, signal at 1470nm and the lasing idler at 1660nm. Which signal/idler pair is generated can be adjusted by changing the pump power

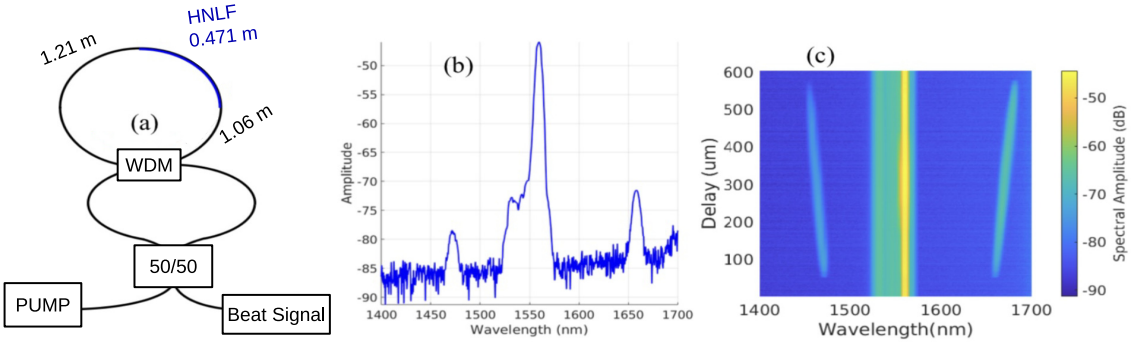

Figure 4.13: Diagram of the OPO sensing loop (a). (b) is a typical spectrum showing the pump (1560nm), signal (1470nm), and lasing idler (1660nm). What signal/idler pair are generated can be tuned by adjusting the pump delay line (c).

(changing the phase matching equation), or with the delay line (changing what part of the pump pulse sees feedback each round-trip). Figure 4.13(c) shows the tunibility of the OPO. Synchronism between the pump and OPO is maintained over a 500μm delay which allows a tunability of around 20nm on the signal and idler.

The system is designed such that the counter-propagating pulses traverse the same path in reverse order. This forces the pulses to be overlapped in time when they emerge from the beat note port shown in Fig. 4.13(a). This removes the requirement of a beat note detection delay line. Fig. 4.14 shows a beat signal measurement in time (a) and the corresponding RF spectrum (b). Because the sensor is at rest, this beat frequency is due to the Kerr nonlinearity causing the unequal intensity pulses to pick up a differential phase. The bandwidth of the RF spectrum is caused by instability in the laser. Because the OPO is highly sensitive to the characterics of the pump, the next step will be to stabilize the pump in order to reduce this bandwidth. Additionally, a variable power splitter will be used in place of the static 50/50 splitter currently in use so as to adjust the bias and more fully investigate the

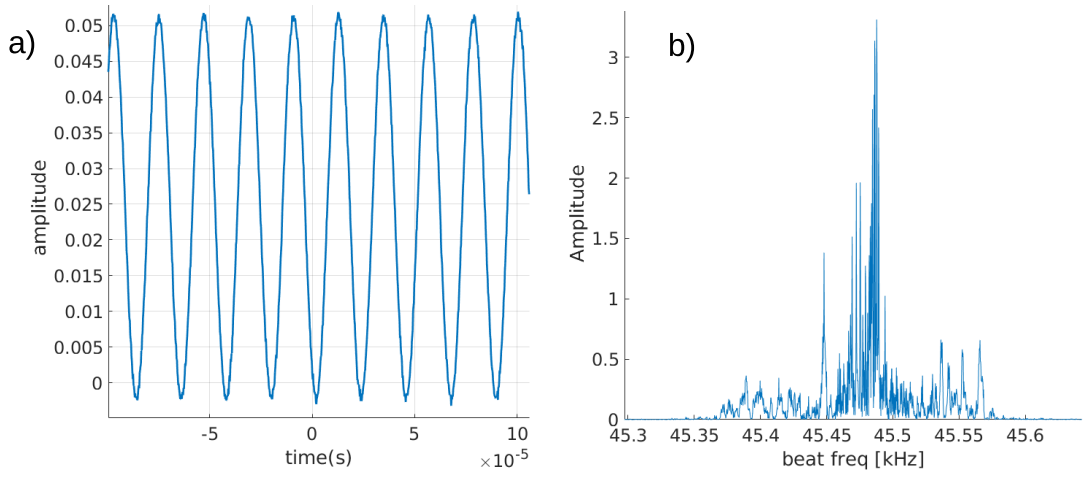

Figure 4.14: (a) Raw time data taken of the interference of the two counterpropagating OPO pulses. (b) the Fourier transform of the time signal showing the corresponding RF spectrum of the beat signal.

sensor's operation. The beat frequency currently can be seen to respond to external tapping or manual rotation of the sensor container.

4.4 Linear cavity configuration

The diversity of measurements capable with an IPI sensor are only available if the laser is configured with a linear cavity. Thus, another oscillator-amplifier chain pumping a linear OPO cavity had to be developed. A diagram of the second oscillator-amplifier chain is shown in Fig. 4.15. The main difference between this oscillator and the one developed for the ring OPO is the length of fiber. In order to synchronize the linear OPO cavity to the pump, the linear dimension (single pass) of the OPO cavity must be half the size of the pump ring. To allow for enough fiber between components such that fiber splices can comfortably be made in the OPO cavity, the oscillator had to be enlarged. To facilitate the expansion, a different type of erbium gain fiber was used (Fibercore DHB1500 erbium-doped bowtie PM fiber). This gain fiber has a higher GVD of 40 ps^2/km. The total round-trip dispersion should be slightly negative (around -0.1 ps^2) in order to enable stable soliton mode-locking. So, by using a gain fiber with higher positive dispersion, additional negative dispersion

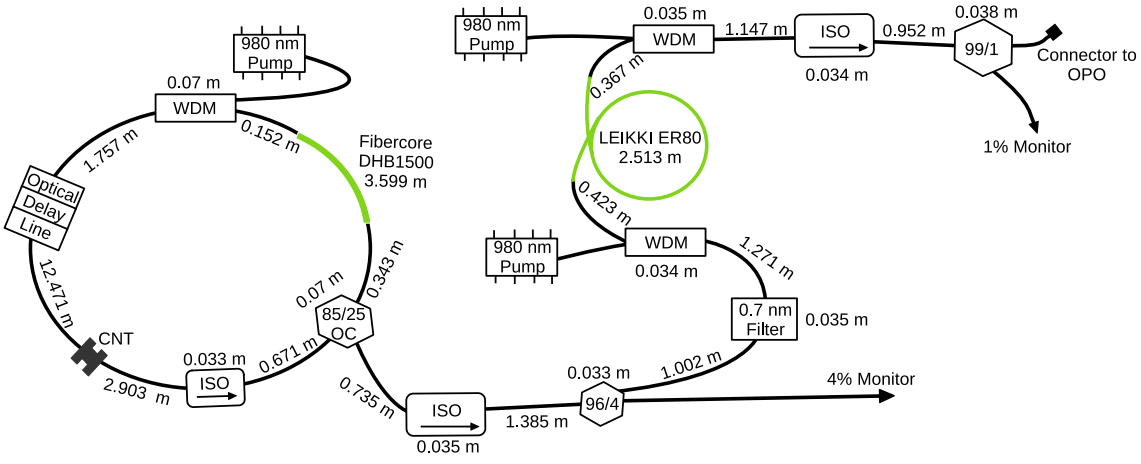

Figure 4.15: Erbium Oscillator-amplifier chain used to pump the linear OPO cavity. The components are labelled as follows: WDM = wavelength division multiplexor; ISO = isolator; CNT = carbon nanotube saturable absorber; OC = Output Coupler.

Corning PM1550 (-22 ps^2/km) transport fiber can be included. Interestingly, the laser mode-locked with a total dispersion of -0.262ps^2/km when the pump diode was driven with 65.3mA. The output spectrum was centered at 1621nm with a repetition rate of 9.267MHz (107.89ns period) and 2.2μW was measured at the 4% monitor port as seen in Fig. 4.16. As with the ring laser pump, this oscillator has been left running continuously to increase longevity.

The HNLF OPO gain fiber used in the ring IPI configuration had PM1550 fiber pigtails already spliced. This was not the case for the linear configuration. The Fujikura FSM-45PM arc fusion splicer did not have the capability to automatically align the HNLF elliptical core to the PANDA polarization rods of the PM1550 fiber. Thus, an active polarization alignment apparatus had to be build. Fig. 4.17 shows the experimental setup. Linearly polarized light was coupled from a 1550nm diode laser into the HNLF fiber. By monitoring the polarization state at the output of the HNLF with a home-built polarimeter (polarization cube rotation and power meter as described in [4]), the light input to the fiber could be made to align with one of the polarization axis of the elliptical core HNLF. Once the probe light was properly aligned, the other end of the HNLF was placed in the splicer along with the PM1550

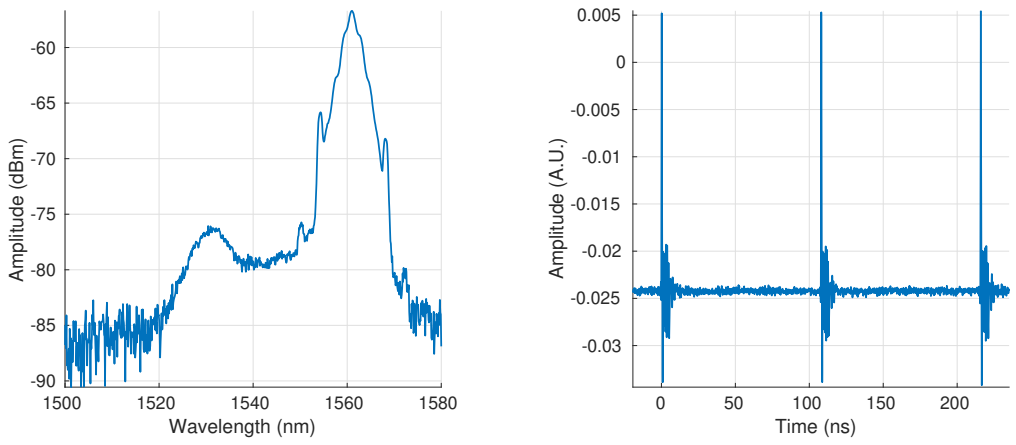

(a) (b)

Figure 4.16: Optical spectrum (a) and pulse train (b) of the pump oscillator for the linear OPO laser. The spectrum is centered at 1561nm and stable mode-locking is encountered when the diode is driven with a current of 65.3mA. The repetition rate is measured to be 9.267 MHz and 2.2μW is measured out of the 4% monitor such that it can be assumed that the oscillator outputs an average power of 55μW. Note that the autocorrelation for this pump is similar to that shown for the ring configuration pump, and thus has little to no chirp.

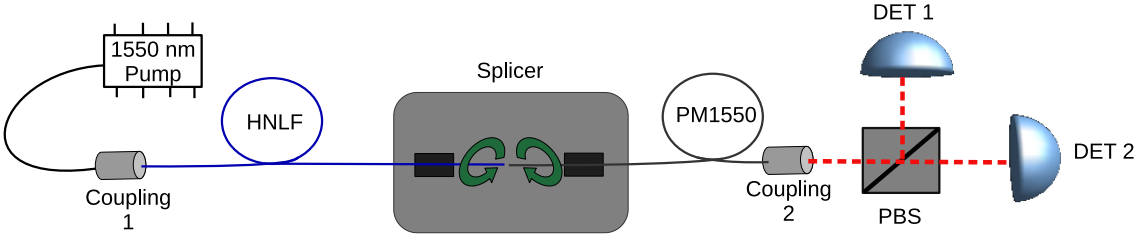

Figure 4.17: Active polarization alignment setup used to splice the HNLF elliptical core fiber to the PANDA PM1550 fiber. Coupling 1 must be set such that the linearly polarized 1550nm source is aligned to the HNLF elliptical core. Similarly, coupling 2 must be rotated such that the fast and slow axes are aligned to the two axes of the polarizing beam splitter (PBS). If the two couplings are set correctly, then the polarization axes are aligned when the largest difference between detector DET2 and DET1 is observed as the fiber tips are rotated in the fiber splicer.

fiber. The other end of the PM1550 fiber was spliced to a collimator with polarization axis aligned to a polarization beam splitter. By sending light through this system while slowly rotating the fiber ends in the splicer and monitoring the difference in power between the polarization beam splitter output, the polarization axes could be

accurately aligned to one another. A Thorlabs PDB210C balanced detector was used to measure the difference in power between the two polarization modes. Once the difference between the slow and fast axis intensities was greatest, the two fibers could be spliced together. Given the core size difference between the HNLF and PM1550 fiber, a similar splice recipe as that used for the PCF fiber was used. The arc location was offset 30μm to the side of the HNLF and a long (30000 ms), low power (-10 bit) arc was made. Shorter (1500ms), higher power (5 bit) rearcs were repeated (about 10 times) until the actively monitored power transmission reached a maximum. The method could then be repeated for the opposite end of the HNLF fiber. This method resulted in a 727cm length of HNLF with four splices (two for HNLF-to-PM1550 and two for splicing on FC/APC connectors) having 1.3dB loss. The polarization extinction ratio was measured to be 11.7dB through the 4 splices, however, this was limited by the exctinction ratio of the input pump laser [4].

The linear laser configuration was designed such that only a single length of HNLF was included to limit the number of lossy splices as seen in Fig. 4.18. This required using two 1x2 WDM's to pump the gain medium in counter-propagating directions after the 50/50 splitter. A 90 degree splice was made in one of the pump arms so as to cross-polarize the counter-propagating pulses into the slow and fast axes of the PM fiber. Since the round-trip time of the linear laser had to match that of the pump oscillator, the single pass length of the laser had to be half that of the oscillator ring. The interferometer arm (see the inset of Fig. 4.18) consisted of 3 inline collimators and a custom optically contacted lossless polarization beam splitter crystal as described in [4]. The collimators and beam splitters were aligned such that a single pass through the free-space coupling section added 1.3dB loss. Adding up the cavity losses of 2 inline mirrors (1dB each), 2 WDM's (0.5 dB each), gain fiber splices (1.3dB), and free-space coupling (1 dB) resulted in a round-trip estimated loss of 8.6dB (about 86% loss).

Since the two separate arms of the interferometer need to be the exact same

[4]The commercial pigtail splices made by OFS resulted in 1dB total loss and a polarization extinction ratio of 26.5dB

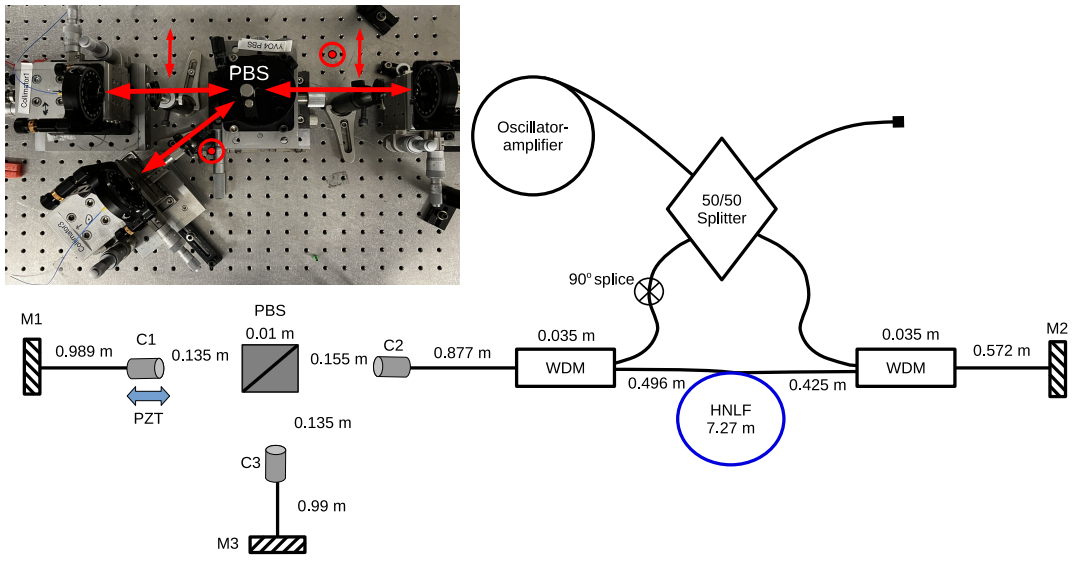

Figure 4.18: Diagram of the linear cavity OPO. The pump is split into counter-propagating directions and pumps the highly nonlinear gain fiber (HNLF) through the wavelength-divison multiplexors (WDMs) in reflection. A 90 degree splice is made in one of the pump arms so that the lasing pulses are cross polarized (one traversing the slow axis and the other the fast axis of the PM fiber). The inline mirrors (M1,M2,M3) retroreflect the light back into the fiber. The inset shows a photo of the free space section of the interferometer arm where the light is collimated into air (C2), sent into a the polarization beam splitter (PBS) which separates the cross-polarized pulses into separate arms which are then are coupled back into fiber (C2 and C3). The collimator C1 can be translated by a piezo-electric transducer (PZT) so as to impart the differential phase shift required of IPI.

length, a systematic way of aligning and coupling the light was required. First, the coupling between the fiber ends was maximized. In Fig. 4.18 coupler C2 and C1 were aligned without the PBS in place. By sending 1550nm light through the C2 coupler and defining the beam path with two irises, light could then be sent in the opposite direction (through C1) and roughly aligned. Once enough light was coupled into a fiber, fine adjustments could be made. The PBS was then put in place between the couplers and the light again aligned to the irises. The polarization alignment was ensured by sending light in either direction and rotating the couplers until maximum power was transmitted through the PBS. The cavity length translation stage had to be set such that coupling was not significantly changed as it was scanned in

order for synchronous pumping to be achieved (explained later). The third coupler (C3) was then aligned without touching the alignment of C2. Light with oppoosite polarization was sent through C2 and another iris was placed to define this reflection beam path. Alignment was done by sending light back through C3 and aligning to the irises. With this method 80-85% coupling was achieved. It should be mentioned that while it seems that using a single coupler with retroreflecting mirrors should be simpler to align, this was initially attempted (with all components mounted to Zerodur low thermal coefficient glass) and only 60% single pass coupling was achieved. It is thought that by using two matched couplers that slightly focus the light, better coupling can be achieved if the second coupler is placed the correct distance away to mode match.

Next synchronous pumping was achieved. Only the reflection cavity (C2-C3) was pumped initially. The length of fiber in the linear cavity was purposefully made to be too long, and the fiber was then cut back one splice at a time. After each splice, evidenc of OPO was searched for while the delay line in the oscillator was scanned. Once OPO was achieved in the reflection cavity, the opposite polarization cavity (C2-C1) was pumped. The same method was used here, however, none of the fiber lengths involved in the reflection cavity were changed (including the oscillator delay line). So only the fiber between C1 and M1 was shortened while the translation stage holding the C1 coupler was scanned when searching for OPO evidence.

Remarkably, the long length of gain fiber was able to overcome the high cavity losses and bidirectional, cross-polarized, OPO was observed when the two amplifier drivers were driven at 245mA and 267mA. This pumping led to 76μW average power measured at the 1% monitor port such that it can be assumed that 7.6mW was being directed to the 50/50 splitter. The output spectrum showing the signal, pump and idler of both polarizations lasing independently is shown in Fig. 4.19. This is the first observation of a cross-polarized, dual-correlated comb fiber laser implemented in a linear synchronously pumped OPO cavity.

Now that it has been proven that the linear configuration can be realized, work must be done to stabilize the cavity such that a beat signal can be extracted. To

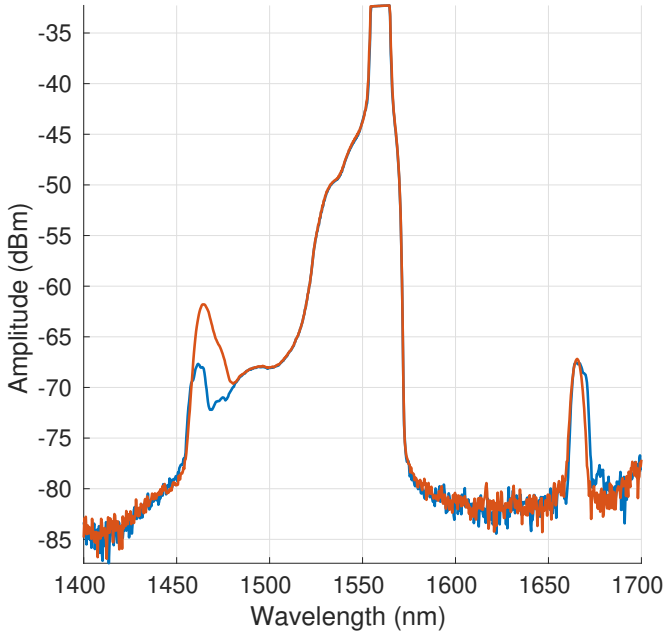

Figure 4.19: Output spectrum of the linear configuration laser showing the lasing OPO signal at 1665nm, pump at 1561nm, and non-lasing corresponding four-wave mixing signal at 1463nm. The two independently lasing cross-polarized pulses are plotted separately (red, blue).

describe the problem more concretely, consider a 1m long cavity (2m round-trip) that uses $\lambda = 1\mu$m light. If a mirror translates by $\Delta L = 1\mu$m (thermal expansion, vibrational noise, etc.), then the central resonant frequency will shift by,

$$\Delta\lambda = \frac{2}{N}\Delta L = 1\text{pm} \rightarrow \Delta\nu = 300\text{MHz}, \tag{4.21}$$

where the lasing mode number N was calculated to be 2×10^6. Since a typical beat frequency is expected to be in the kHz range, a MHz shift in lasing frequency will wash out any evidence of the beating. Engineering enhancements are now required to stabilize the cavity length to acceptable tolerances.

Chapter 5

Intracavity Phase Interferometry Enhancement

5.1 Introduction

As the world strives for more adventurous space missions, higher precision studies of fundamental physics and sleek wearable technology, the need for compact and energy efficient, but highly sensitive, measurement devices has never been greater. Thus, it is beneficial to understand the methods that are available to increase the sensitivity and resolution of a specific detection technique. With few exceptions [51–53] most reports based on intracavity phase sensing have been limited to cw lasers i.e. the gyroscope. In this context, a recent hot topic is a byproduct of the field of non-Hermitian quantum mechanics and the discovery of the Exceptional Point (EP) [54]. By placing a sensor at a specific location in parameter space (the EP), it has been shown that some devices can exhibit significantly increased sensitivity [17, 18]. Unfortunately, these enhancements generally come at the expense of increased noise [55, 56]. For the specific case of the laser gyroscope, the EP is equivalent to the dead band edge where noise and instability dominate [19, 20, 55, 56].

It has been shown that "slow light" media causes a reduction in sensitivity

to resonator path length changes, while "fast light" sensors result in a linewidth broadening that exactly cancels the added sensitivity benefit [57–59] [1]. Recently, the critical anomalous dispersion point spoken about in "fast light" lasers, and their corresponding parasitic noise, have been equated to the EP of non-Hermitian quantum mechanics [19, 20, 55]. By equating the two areas of study, the experimental work regarding the critical anomalous dispersion point can be reexamined in the context of EP theory. One can then conclude that the broadened linewidth is caused by coupling between modes as quantified by the Petermann excess noise factor. This multiplicative factor to the Schawlow-Townes linewidth describes a linewidth broadening that is generated by mode nonorthagonality resulting from mode coupling [60].

Section 5.2 below will introduce the concepts of non-Hermitian Quantum mechanics and section 5.3 will show that Exceptional Point enhancement causes added noise according to the Petermann excess noise factor. Section 5.4 will then show that by reducing the coupling between the modes by way of an ultrafast intracavity phase interferometry sensor, the linewidth broadening typically encountered by dispersion enhancement can be avoided.

5.2 Non-Hermitian Quantum Mechanics

One of the first postulates of quantum mechanics that students are taught is that all operators must be Hermitian. That is, if $\hat{A}$ is some operator, then $\hat{A} = \hat{A}^{\dagger}$, where $\dagger$ is the conjugate transpose. The reason for this restriction is simply that these operators correspond to physical observables which therefore must be real. It is a common linear algebra exercise to show that Hermitian matrices always have real eigenvalues.

Theorem 1. *All Hermitian operators have real eigenvalues*

[1] Slow light refers to light that has a group velocity, v_g, that is much slower than the speed of light in vacuum, c, ($v_g \ll c$). Fast light, then, corresponds to the situation of $v_g \gg c$.

Proof. If $|\psi\rangle$ is an eigenvector of the operator $\hat{A}$ with eigenvalue a then,

$$\begin{aligned} \hat{A}\,|\psi\rangle &= a\,|\psi\rangle \\ \langle\psi|\hat{A}|\psi\rangle &= \langle\psi|a|\psi\rangle \\ &= a\,\langle\psi|\psi\rangle\,. \end{aligned} \tag{5.1}$$

Similarly,

$$\begin{aligned} \langle\psi|\hat{A}|\psi\rangle^{\dagger} &= \langle\psi|a|\psi\rangle^{\dagger} \\ \langle\psi|\hat{A}^{\dagger}|\psi\rangle &= a^{*}\,\langle\psi|\psi\rangle\,. \end{aligned} \tag{5.2}$$

Since $\hat{A}$ is Hermitian, $\hat{A} = \hat{A}^{\dagger}$, which leads to the conclusion that (5.1)=(5.2). Thus, $a = a^{*}$, which is only true if a is real. □

Other useful properties of Hermitian operators include that they conserve probability through unitary transformations, $U = e^{i\hat{A}}$, and they force an orthonormal basis since their eigenvectors are orthogonal. These seem to be common sense requirements of any operator since any useful theorem should include observables (real eigenvalues), conserve energy (unitary transformations), and create a reasonable space to make calculations (orthogonal eigenvectors).

In 1988, however, Carl Bender showed that some non-Hermitian Hamiltonians (energy operators) can still result in real eigenvalues if they are invariant under parity and time inversion (referred to as $\mathcal{PT}$-symmetry) [54]. In fact, He went on to claim that $\mathcal{PT}$-symmetry is actually the broader requirement of operators i.e. that every Hermitian operator is $\mathcal{PT}$-symmetric.

To make this more concrete, consider the non-Hermitian Hamiltonian used by Bender,

$$\hat{H} = \hat{p}^2 + \hat{x}^2(i\hat{x}). \tag{5.3}$$

Inverting space (parity) changes the sign of the momentum and space operators such that the parity operator induces the change,

$$\hat{P}: \qquad \hat{p} \to -\hat{p} \qquad \text{and} \qquad \hat{x} \to -\hat{x}. \tag{5.4}$$

Inverting time leaves the space operator as is, but negates the imaginary unit, which also causes the momentum operator to flip sign so that the time inversion operator causes,

$$\hat{T}: \qquad \hat{p} \to -\hat{p} \qquad \text{and} \qquad i \to -i. \tag{5.5}$$

With this it is straightforward to see that the Hamiltonian of Eq. (5.3) is $\mathcal{PT}$-symmetric since,

$$\hat{P}\hat{T}\hat{H} = (-\hat{p})^2 + (-\hat{x})^2(-i)(-\hat{x}) = \hat{p}^2 + \hat{x}^2(i\hat{x}) = \hat{H}. \tag{5.6}$$

The Hamiltonian of Eq. (5.3) has been shown by Carl Bender to have purely real eigenvalues, which led to the conclusion that operator Hermiticity is a sufficient but not necessary requirement for quantum mechanical operators. This has birthed the field of Non-Hermitian quantum mechanics (NHQM). NHQM has been called an analytic continuation of Hermitian quantum mechanics as you can imagine that $\hat{H} = \hat{p}^2 + \hat{x}^2(i\hat{x})$ is just a continuation of the Hermitian harmonic oscillator Hamiltonian $\hat{H} = \hat{p}^2 + \hat{x}^2$ into the complex plane.

In order to show that **any** $\mathcal{PT}$-symmetric Hamiltonian has real eigenvalues, a few definitions must be made. First, inverting space and time twice should leave the system unchanged,

$$(\hat{P}\hat{T})^2 = 1. \tag{5.7}$$

Second, if a Hamiltonian is $\mathcal{PT}$-symmetric, then it must commute with the $\hat{P}\hat{T}$ operator,

$$[\hat{H}, \hat{P}\hat{T}] = 0. \tag{5.8}$$

Last, $\hat{H}$ and $\hat{P}\hat{T}$ operate in the same space. In other words, every eigenfunction of $\hat{H}$ is also an eigenfunction of $\hat{P}\hat{T}$,

$$\text{if} \qquad \hat{H}\left|\phi\right\rangle = E\left|\phi\right\rangle \qquad \text{then} \qquad \hat{P}\hat{T}\left|\phi\right\rangle = \lambda\left|\phi\right\rangle, \tag{5.9}$$

where E and λ are eigenvalues. This actually isn't a definition, but a postulate as it is not always satisfied. Another operator, $\hat{C}$, has since been defined to ensure this is

satisfied so that the necessary and sufficient condition of real eigenvalues is that the Hamiltonian commutes with the $\hat{P}\hat{T}\hat{C}$ operators [2]. If the system commutes with $\hat{C}$, then the state is termed to have, "unbroken symmetry", while the situation of the commutation relationship only being maintain with the $\hat{P}\hat{T}$ operators is referred to as having, "broken symmetry".

Theorem 2. *All Hamiltonians exhibiting unbroken $\mathcal{PT}$-symmetry have real eigenvalues.*

Proof. Unbroken $\mathcal{PT}$-symmetry means that Eq. (5.9) must be true. First it must be shown that the eigenvalue of the $\hat{P}\hat{T}$ operator, λ, is a pure phase.

$$\hat{P}\hat{T}\left|\psi\right\rangle = \lambda\left|\psi\right\rangle$$

Now multiply both sides by $\hat{P}\hat{T}$ and then take advantage of Eq. (5.7) twice.

$$\begin{aligned}(\hat{P}\hat{T})^2\left|\psi\right\rangle &= \hat{P}\hat{T}\lambda\left|\psi\right\rangle \\ \left|\psi\right\rangle &= \hat{P}\hat{T}\lambda\left|\psi\right\rangle \\ \left|\psi\right\rangle &= \hat{P}\hat{T}\lambda(\hat{P}\hat{T})^2\left|\psi\right\rangle \end{aligned} \tag{5.10}$$

Now because the $\hat{P}\hat{T}$ operator switches the sign of the imaginary unit, it is an antilinear operator. This means that $\hat{P}\hat{T}\lambda\hat{P}\hat{T} = \lambda^*$ and thus,

$$\left|\psi\right\rangle = \lambda^*\lambda\left|\psi\right\rangle. \tag{5.11}$$

Therefore $|\lambda|^2 = 1$ which is only true if $\lambda = e^{i\phi}$ i.e. a pure phase. Now since the Hamiltonian operates in the same space as the $\hat{P}\hat{T}$ operator (unbroken symmetry), this allows it to operate on the same eigenvector,

$$\begin{aligned}\hat{H}\left|\psi\right\rangle &= E\left|\psi\right\rangle \\ \hat{P}\hat{T}\hat{H}\left|\psi\right\rangle &= \hat{P}\hat{T}E\left|\psi\right\rangle \\ &= \hat{P}\hat{T}E(\hat{P}\hat{T})^2\left|\psi\right\rangle \end{aligned} \tag{5.12}$$

[2] Note that this $\hat{C}$ operator is not equivalent to the charge operator in particle physics but is denoted with the same symbol due to its similar properties

Taking advantage of the fact the $\hat{H}$ and $\hat{P}\hat{T}$ commute allows the left-hand-side to be rearranged and $\hat{P}\hat{T}$ to operate on $|\psi\rangle$ such that,

$$\begin{aligned} \hat{H}\hat{P}\hat{T}\,|\psi\rangle &= \hat{P}\hat{T}E(\hat{P}\hat{T})^2\,|\psi\rangle \\ \hat{H}\lambda\,|\psi\rangle &= \hat{P}\hat{T}E\hat{P}\hat{T}\lambda\,|\psi\rangle \\ \lambda E\,|\psi\rangle &= E^*\lambda\,|\psi\rangle \end{aligned} \tag{5.13}$$

Considering the fact that λ is a phase means that $E = E^*$ i.e. the eigenvalues are real. □

An important observable difference between Hermitian and non-Hermitian systems appears near singularities. A Hermitian singularity is called a diabolical point (DP), where the eigenvalues are degenerate but the eigenvectors remain orthogonal. Non-Hermitian singularities, on the other hand, are termed exceptional points (EPs) and result in a coalescing of both the eigenvalues and eigenvectors. The eigenvectors are not orthogonal and therefore no longer span the space, but split into the complex plane. One area where this new quantum formalism is being employed is in laser systems since they are inherently non-Hermitian due to gain/loss dynamics. The coalescing of the eigenvalues and eigenvectors at the EP has led to many newly observed laser phenomena due to the ability to remove certain allowed modes. [61–63].

Laser sensor research is one specific field that has attempted to benefit from this new formalism [16, 18, 22]. Typically, laser sensors operate at a diabolical point such that the quantity to be measured lifts the system out of the singularity linearly. If a laser sensor could be placed at an exceptional point instead, the same quantity to be measured would lift the system out of the singularity nonlinearly. This means that at low detunings, the response of the EP sensor would be greatly enhanced over the DP sensor.

In order to make this discussion more concrete, let us take a specific example of the laser gyroscope. Chapter 3.4 showed that a mode-locked laser can be represented as a 2-level quantum system [14]. This makes the transition to representing a laser system with the language of NHQM straightforward. Consider a single cavity mode-locked

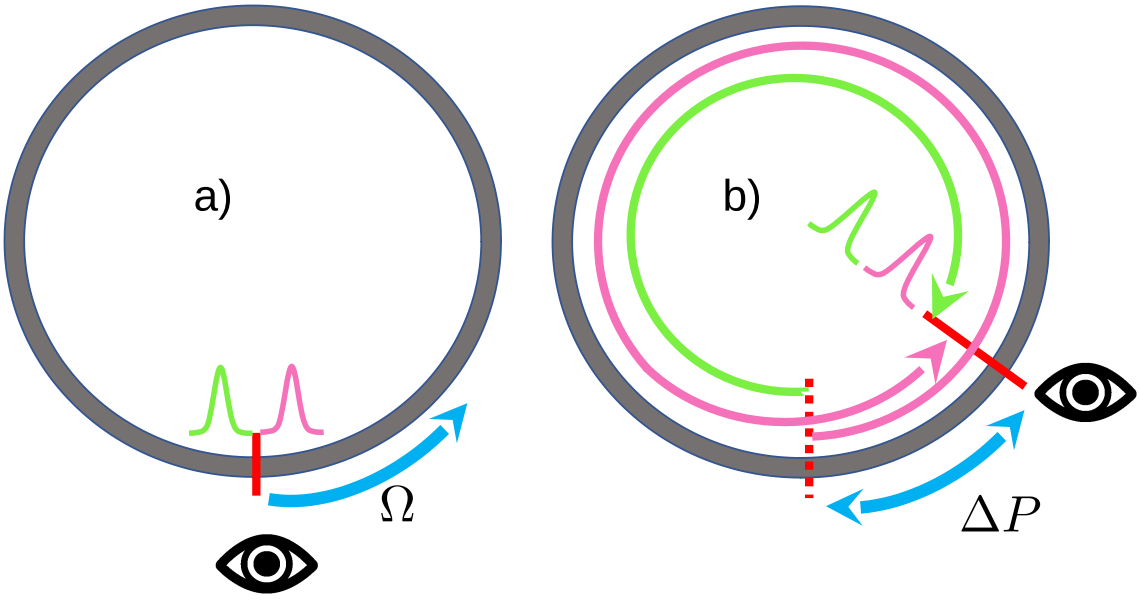

Figure 5.1: Idealized laser gyroscope. Two electric fields (green, pink) counter-propagate in a ring cavity (a). Because the ring is rotating at an angular frequency, Ω, the two fields encounter two different effective cavity round-trip lengths (b). This cavity length difference ΔP results in the two fields lasing at slightly detuned frequencies and thus create a beat note when interferred on a detector.

laser gyroscope as seen in Fig. 5.1. There are two counterpropogating electric fields, E_1 and E_2 (green and pink). As the gyroscope is rotated, one pulse will travel a longer effective optical path such that when the fields are interfered in time on the detector, $|E_1 + E_2|^2$, a beat frequency will be observed.

The counterpropogating electric fields can be represented as $\tilde{E}_{1,2}(t) = \tilde{\mathcal{E}}_{1,2}(t)e^{i\omega t}$ where $\tilde{\mathcal{E}}(t)$ is the Gaussian pulse amplitude and $\omega = (\omega_1 + \omega_2)/2$ is the rotating frame average frequency. The coupled-mode equations for the electric field amplitudes of an idealized gyroscope (no coupling between counterpropogating electric fields and equal constant gain in each field) are then,

$$\dot{\tilde{\mathcal{E}}}_1(t) = -i\frac{\Delta}{2}\tilde{\mathcal{E}}_1(t) \tag{5.14}$$

$$\dot{\tilde{\mathcal{E}}}_2(t) = i\frac{\Delta}{2}\tilde{\mathcal{E}}_2(t), \tag{5.15}$$

where the detuning is defined as $\Delta = \omega_2 - \omega_1$. From this a Schrödinger-like equation

can be contructed. Recall the form of the Schrödinger equation,

$$i\frac{\partial}{\partial t}\left|\psi\right\rangle = \hat{H}\left|\psi\right\rangle, \tag{5.16}$$

where for a two-level system we have $|\psi\rangle = (\psi_1, \psi_2)$. Our amplitudes will then be a weighted linear combination of the eigenstates such that,

$$\tilde{\mathcal{E}}_1 = a_1\psi_1 + b_1\psi_2 \tag{5.17}$$

$$\tilde{\mathcal{E}}_2 = a_2\psi_1 + b_2\psi_2. \tag{5.18}$$

Converting the coupled-mode Eqs. 5.14 and 5.15 into a matrix equation and rearranging into the form of Eq. 5.16 leads to,

$$\hat{H} = \begin{pmatrix} \Delta/2 & 0 \\ 0 & -\Delta/2. \end{pmatrix} \tag{5.19}$$

Notice that $\hat{H}$ is Hermitian and by using the third Pauli matrix, $\sigma_3 = \begin{pmatrix} 1 & 0 \\ 0 & -1 \end{pmatrix}$, it is easy to see that the eigenstates are $|1\rangle = (1,0) = \psi_1$ and $|2\rangle = (0,1) = \psi_2$ with eigenvalues, $\lambda_{1,2} = \pm\Delta/2$. This means the two allowed modes in this gyroscope are,

$$\psi_{1,2} = \tilde{\mathcal{E}}_{1,2} = \mathcal{E}_{1,2}e^{\pm\frac{i\Delta}{2}t}. \tag{5.20}$$

Notice the singularity at $\Delta = 0$. Here the eigenvalues become 0, but the eigenstates remain unchanged. This is the definition of a DP. When the two fields are interfered in time, the signal the detector sees is,

$$\begin{aligned} |E_1 + E_2|^2 &= \frac{1}{4}\left(|\tilde{\mathcal{E}}_1|^2 + |\tilde{\mathcal{E}}_2|^2 + \tilde{\mathcal{E}}_1\tilde{\mathcal{E}}_2^* + \tilde{\mathcal{E}}_1^*\tilde{\mathcal{E}}_2\right) \\ &= \frac{1}{4}\left(\mathcal{E}_1^2 + \mathcal{E}_2^2 + 2\mathcal{E}_1\mathcal{E}_2e^{-i\Delta t}\right), \end{aligned} \tag{5.21}$$

which means the beat frequency is Δ. The DP is at $\Delta = 0$ with the beat frequency increasing linearly with Δ as seen by the red curve in Fig. 5.2.

In order to observe an EP, we must add coupling into the coupled-mode equations,

$$\dot{\tilde{\mathcal{E}}}_1(t) = -i\frac{\Delta}{2}\tilde{\mathcal{E}}_1(t) + S\tilde{\mathcal{E}}_2(t) \tag{5.22}$$

$$\dot{\tilde{\mathcal{E}}}_2(t) = i\frac{\Delta}{2}\tilde{\mathcal{E}}_2(t) + S\tilde{\mathcal{E}}_1(t). \tag{5.23}$$

Notice that the coupling coefficient is non-conservative. In this case,

$$\hat{H} = \begin{pmatrix} \Delta/2 & iS \\ iS & -\Delta/2 \end{pmatrix}, \tag{5.24}$$

which is non-Hermitian owing to the off-diagonals. It is, however, $\mathcal{PT}$-symmetric since inverting space and time gives the exact same system. The eigenvectors are,

$$|1\rangle = \begin{bmatrix} \frac{1}{iS}\left(\sqrt{(\Delta/2)^2 - S^2} - \Delta/2\right) \\ 1 \end{bmatrix} \tag{5.25}$$

$$|2\rangle = \begin{bmatrix} \frac{1}{iS}\left(-\sqrt{(\Delta/2)^2 - S^2} - \Delta/2\right) \\ 1 \end{bmatrix}, \tag{5.26}$$

with eigenvalues $\lambda_{1,2} = \pm\sqrt{(\Delta/2)^2 - S^2}$. The important part to notice here is that there is a singularity at $\Delta/2 = S$. At this point there is a coalescing of both eigenvectors and eigenvalues,

$$|1\rangle = |2\rangle = \begin{bmatrix} -\frac{1}{iS}\frac{\Delta}{2} \\ 1 \end{bmatrix} \tag{5.27}$$

$$\lambda_1 = \lambda_2 = 0. \tag{5.28}$$

This is the location of the EP. Notice that if Δ decreases from this point, the system splits into the complex plane. This is an example of broken $\mathcal{PT}$-symmetry. If Δ increases past the EP the system enters an unbroken-symmetry regime and the beat frequency increases from 0 with a square-root dependence (see Fig. 5.2 where the solid blue curve is the real part and the dashed blue is the imaginary part). Those familiar with gyroscope response curves may notice that this curve looks eerily similar to what is termed the deadband or lock-in region. This similarity has been shown to be an equivalence [20]. This square-root response curve is what excites those in the sensing world as it shows enhanced sensitivity (increased slope). In fact, if one were to place a system exactly at the EP, the sensitivity would theoretically be infinite since any small perturbation would lift the system out of the degeneracy. However,

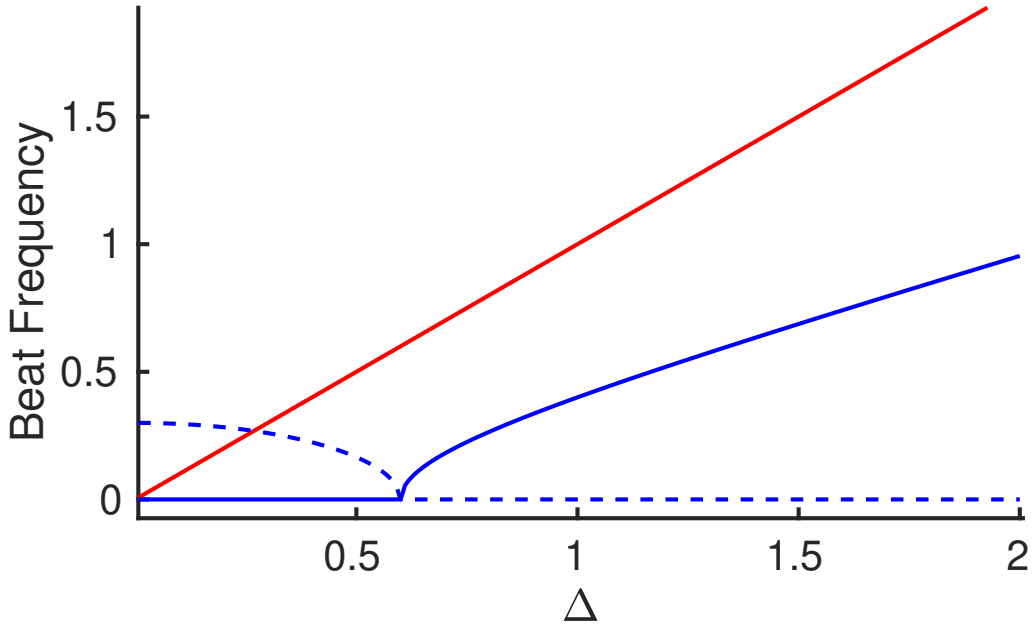

Figure 5.2: Two-level system beat frequency response curve showing a Diabolical Point at $\Delta = 0$ (red) and an Exceptional Point degeneracy at $\Delta = 2S = 0.6$ (blue) degeneracy. Also note that the $\mathcal{PT}$-symmetric system splits into the imaginary plan below the singularity at the Exceptional Point (dashed blue). The DP (red curve) can be interpreted as a gyroscope without a coupling caused dead band, while the EP (blue curve) is a typical gyroscope with dead band response.

the experimental feasibility remains suspect as some studies have shown that the enhancement is overcome by noise and instability [55, 56].

5.3 Exceptional Point enhancement

While the increased slope of the sensor response curve near the Exceptional Point seems to indicate that it would be desireable to operate a laser sensor in this regime (solid blue curve in Fig. 5.2), it has been shown that parasitic noise acts to counteract the benefit [55, 56]. The Petermann factor, K_p, characterizes the linewidth broadening that occurs around the EP and is given by [60, 64],

$$K_p = \frac{1}{1 - |\langle v_+ | v_- \rangle|^2}, \tag{5.29}$$

where $|v_\pm\rangle$ are the two eigenmodes of the system that must be normalized to $\langle v_\pm|v_\pm\rangle = 1$ for the Petermann factor to take the simple form seen in Eq. (5.29) [65]. Clearly the Petermann factor increases as the modes become nonorthogonal $\langle v_+|v_-\rangle > 0$ near the EP.

To see this, we start with the laser model described in Chapter 3.4 where the laser sensor can be characterized by the coupled-mode system of Eq. (3.63),

$$\begin{pmatrix} \dot{\tilde{\mathcal{E}}}_1 \\ \dot{\tilde{\mathcal{E}}}_2 \end{pmatrix} = \begin{bmatrix} -i\Delta\varphi/2 & s \\ s & i\Delta\varphi/2 \end{bmatrix} \begin{pmatrix} \tilde{\mathcal{E}}_1 \\ \tilde{\mathcal{E}}_2 \end{pmatrix}. \tag{5.30}$$

which has the analytic solution,

$$\begin{aligned} \tilde{\mathcal{E}}_1(t) &= c_+ v_+^{(1)} e^{i\lambda_+ t} + c_- v_-^{(1)} e^{i\lambda_- t} \\ \tilde{\mathcal{E}}_2(t) &= c_+ v_+^{(2)} e^{i\lambda_+ t} + c_- v_-^{(2)} e^{i\lambda_- t}. \end{aligned} \tag{5.31}$$

The eigenvalues are,

$$\lambda_\pm = \pm \frac{\sqrt{\Delta\varphi^2 - 4s^2}}{2}, \tag{5.32}$$

and eigenvectors,

$$v_\pm = \mu_\pm \begin{bmatrix} 2s \\ i\Delta\varphi \pm i\sqrt{\Delta\varphi^2 - 4s^2} \end{bmatrix}, \tag{5.33}$$

where $\mu_\pm$ is the normalization factor. If the system is just outside of the dead band edge (or EP) such that $\Delta\varphi^2 > 4s^2$, then, to ensure that the normalization $\langle v_\pm|v_\pm\rangle = 1$ holds, we have to add the normalization factor of,

$$\mu_\pm = \frac{1}{\sqrt{2\left(\Delta\varphi^2 \pm \Delta\sqrt{\Delta\varphi^2 - 4s^2}\right)}}. \tag{5.34}$$

The inner product is then,

$$\begin{aligned} \langle v_+|v_-\rangle &= \mu_+\mu_- \begin{bmatrix} 2s & -i\Delta\varphi - i\sqrt{\Delta\varphi^2 - 4s^2} \end{bmatrix} \begin{bmatrix} 2s \\ i\Delta\varphi - i\sqrt{\Delta\varphi^2 - 4s^2} \end{bmatrix} \\ &= \frac{2s}{\Delta\varphi}. \end{aligned} \tag{5.35}$$

Plugging this into Eq. (5.29) shows explicitly that the Petermann factor diverges as the system approaches the dead band edge at $\Delta\varphi = 2s$:

$$K_p = \frac{1}{1 - \frac{4s^2}{\Delta\varphi^2}}. \tag{5.36}$$

There is another degeneracy, termed the 'gain difference Exceptional Point' in the language of [20], that occurs when gain and conservative coupling is included in the model (see for instance [16]). This EP has been shown to be equivalent to the critical anomalous dispersion point of 'fast light' lasers where the Petermann factor noise exactly cancels the additional sensitivity enhancement [55, 57–59]. A point rarely made in the literature is that this EP is actually not a degeneracy in the beat frequency, but in the absolute optical frequency. This is important as the measurement of the absolute frequency is harder to make and plagued by more classical noise than the beat frequency measurement. To prove this fact mathematically, the coupled-mode system must be updated by replacing the non-conservative coupling with the conservative coupling of, $\kappa_1 = \kappa = -\kappa_2^*$, and including saturable gain,

$$\alpha_i = \frac{\alpha_0}{1 + W_i/W_s} - \beta_i, \tag{5.37}$$

where α_0 is the small signal gain factor per round-trip, $W_i = (\int |\mathcal{E}_i|^2 dt)/2\eta$ is the pulse energy density, W_s is the saturation energy density, η is the characteristic impedance of the medium, and β_i is the linear loss per round-trip for each field. Thus, the coupled-mode equations become:

$$\begin{pmatrix} \dot{\tilde{\mathcal{E}}}_1 \\ \dot{\tilde{\mathcal{E}}}_2 \end{pmatrix} = \begin{bmatrix} \alpha_1 - i\Delta\varphi/2 & \kappa \\ -\kappa^* & \alpha_2 + i\Delta\varphi/2 \end{bmatrix} \begin{pmatrix} \tilde{\mathcal{E}}_1 \\ \tilde{\mathcal{E}}_2 \end{pmatrix}. \tag{5.38}$$

In this case the eigenvalues are,

$$\lambda_\pm = i\frac{\alpha_1 + \alpha_2}{2} \pm \frac{\chi}{2}, \tag{5.39}$$

where,

$$\chi = \sqrt{4|\kappa|^2 - [(\alpha_1 - \alpha_2) - i\Delta\varphi]^2}. \tag{5.40}$$

The final solutions are again a linear combination of the eigenvalues and eigenvectors according to Eq. (5.31). The gain difference Exceptional Point occurs when the gain difference offsets the conservative coupling such that $(\alpha_1 - \alpha_2 - i\Delta\varphi)^2 = 4|\kappa|^2$. This can be observed by setting $\alpha_1 = k$, $\alpha_2 = -k$. The eigenvalue then reduces to,

$$\begin{aligned}\lambda_\pm &= \pm\frac{\chi}{2},\\ \chi &= \sqrt{-i2k\Delta\varphi - \Delta\varphi^2}.\end{aligned}$$

Since the Exceptional Point occurs at $\Delta\varphi = 0$, it can be assumed that $\Delta\varphi$ is small, such that,

$$\begin{aligned}\lambda_\pm &= \pm\frac{\chi}{2} = \pm\frac{1}{2}\sqrt{-2i\kappa\Delta\varphi - \Delta\varphi^2}\\ &\approx \pm\sqrt{\frac{\kappa\Delta\varphi}{2}}\sqrt{-i} = \pm\frac{1}{2}\sqrt{\kappa\Delta\varphi}(1-i).\end{aligned} \tag{5.41}$$

Plugging this into Eq.(5.31) leads to,

$$\begin{aligned}\tilde{\mathcal{E}}_1 &= A_1 v_+^{(1)} e^{it\sqrt{\kappa\Delta\varphi}/2 - t\sqrt{\kappa\Delta\varphi}/2} + A_2 v_-^{(1)} e^{it\sqrt{\kappa\Delta\varphi}/2 + t\sqrt{\kappa\Delta\varphi}/2}\\ \tilde{\mathcal{E}}_2 &= A_1 v_+^{(2)} e^{it\sqrt{\kappa\Delta\varphi}/2 - t\sqrt{\kappa\Delta\varphi}/2} + A_2 v_-^{(2)} e^{it\sqrt{\kappa\Delta\varphi}/2 + t\sqrt{\kappa\Delta\varphi}/2}.\end{aligned} \tag{5.42}$$

The saturable gain in the lasing cavity will act such that gain and decay terms are eliminated, leaving,

$$\begin{aligned}\tilde{\mathcal{E}}_1 &= \left(A_1\epsilon_+^1 + A_2\epsilon_-^1\right) e^{it\sqrt{\kappa\Delta\varphi}/2}\\ \tilde{\mathcal{E}}_2 &= \left(A_1\epsilon_+^2 + A_2\epsilon_-^2\right) e^{it\sqrt{\kappa\Delta\varphi}/2}.\end{aligned} \tag{5.43}$$

This shows algebraically that under the circumstances of operating near this Exceptional Point, the two counterpropagating electric fields oscillate at the same frequency.

Numerical verification can be found by solving the system of coupled differential equations, Eq. (5.38), for a conservative coupling $\kappa = 0.05$, saturable gain using $\alpha_0 = 0.1$, $W_s = 1$, $\beta_1 = 0$, $\alpha_2 = -\kappa$, and $\Delta\varphi = 2\pi * 0.1$. The results are presented in Fig. 5.3 which shows the two fields oscillating with the same optical frequency. Initial cw fields of amplitude 1 were used, and the real fields are plotted as a function of time. Assuming a cavity $\tau_p = 1$ ns, the displayed period is 20 ns which corresponds

to a frequency of 0.05 GHz. This does not agree with the predicted frequency of $\frac{1}{4\pi\tau_p}\sqrt{\kappa\Delta\varphi} = 0.014$ GHz because, as stated in [20], the relationship $\alpha_1 - \alpha_2 = 2\kappa$ isn't maintained for $\Delta\varphi > 0$. In this case the gain in the first resonator saturates to $\alpha_1 = 0.00068$, while the second resonator maintains the constant $\alpha_2 = -\kappa$. Plugging these values into Eq. (5.39) and taking the real part (since the imaginary part leads to gain or loss) results in the expected value of, $Re(\lambda_\pm)/(2\pi\tau_p) = 0.05$.

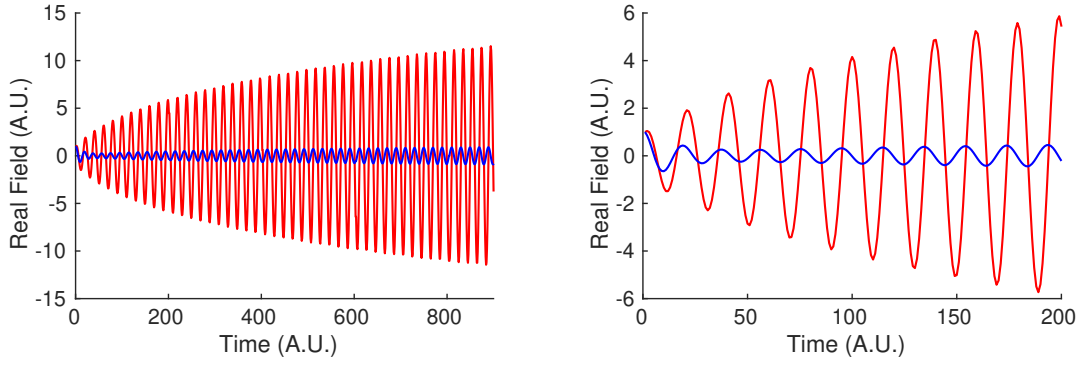

(a) (b)

Figure 5.3: Evolution of the two fields (red, blue) near the "Gain Difference Exceptional Point". Eq. (5.38) was solved using initial cw fields of amplitude 1 and $\kappa = 0.05$, a saturable gain with $\alpha_0 = 0.1$, $W_s = 1$, $\beta_1 = 0$, $\alpha_2 = -\kappa$ in Eq. (5.37), and $\Delta\varphi = 2\pi * 0.1$. Figure 5.3b is a zoomed in plot of 5.3a showing that the two fields have the same optical frequency, and therefore there is no measureable beat frequency when the two fields are interfered.

It is also of note that there exists a phase shift between the fields in Fig. 5.3. This arises from the coupling phase as explained in [66]. In this case, the coupling phase arises becuase $\kappa_1 = 0.05e^{i\pi}$ so that $\kappa_2 = -0.05e^{i0}$.

While no beat frequency can be extracted from this system, the absolute frequency of each of the fields still corresponds to the applied perturbation, $\Delta\varphi$. Thus, there are ways that this could be used as a detector as described in [19]. However, because the modes by definition are non-orthogonal in the area surrounding this Exceptional Point, the issue of added noise remains. Another point of concern is that a lasing cavity requires a saturable gain which means that maintaining the two relationships, $(\alpha_1 - \alpha_2)^2 = 4|\kappa|^2$, and $\alpha_1 + \alpha_2 = 0$, that are required to place the system at the

Exceptional Point becomes a challenge. Forcing the gain terms to be constants of $\alpha_1 = k = -\alpha_2$ results in the real electric fields tending to positive and negative infinity. This is also the case when one chooses the saturable terms,

$$\alpha_{\pm} = \frac{\alpha_0}{1 + W_i/W_s} \pm \kappa. \tag{5.44}$$

The only way to maintain steady-state lasing seems to be to choose a saturable gain term in one resonator and a constant loss of κ in the other,

$$\alpha_1 = \frac{\alpha_0}{1 + W_i/W_s} \tag{5.45}$$

$$\alpha_2 = -\kappa. \tag{5.46}$$

However, as $\Delta\varphi$ is increased, the energy is unequally focused into the first resonator such that α_1 decreases. This means, then, that the only time that the EP relationship is maintained is at $\Delta\varphi = 0$.

5.4 Resonant dispersion

Recalling the model of section 3.2.4, it was shown that the electric field can be built up in frequency one round-trip at a time according to (ignoring coupling for now):

$$\tilde{\mathcal{A}}_{\pm} = \tilde{\mathcal{A}}_{\pm,x} e^{-i\tau_p(\pm\Delta\varphi/2 + \Delta\Omega)}. \tag{5.47}$$

Summarizing the different applied detuning variables used thus far $(\Delta, \Delta\varphi)$, the ultimate frequency mode splitting, δ_0, imparted to the IPI frequency combs in a laser cavity of length, L, and phase delay, τ_p, is represented by,

$$\delta_0 = \frac{\Delta}{2\pi L} = \frac{\Delta\varphi}{2\pi\tau_p}. \tag{5.48}$$

If an additional dispersive element is inserted into the cavity with a *periodic* transfer function of $\tilde{h} = e^{-i\psi(\Delta\Omega)}$, then the round-trip is represented as:

$$\tilde{\mathcal{A}}_{\pm,x+1} = \tilde{\mathcal{A}}_{\pm,x} e^{-i[\pm(\Delta\varphi/2)\tau_p + \tau_p\Delta\Omega + \psi(\Delta\Omega)]}. \tag{5.49}$$

Using a Taylor expansion limited to first order $\psi(\Delta\Omega) \approx \psi_0 + \Delta\Omega\, \partial\psi/\partial\Delta\Omega|_0$, and ignoring the global phase factor ψ_0 since it affects all teeth on each comb equally results in:

$$\tilde{\mathcal{A}}_{\pm,x+1} = \tilde{\mathcal{A}}_{\pm,x} e^{-i\left[\pm(\Delta\varphi/2)\tau_p + \left(\tau_p + \frac{\partial\psi}{\partial\Delta\Omega}\Big|_0\right)\Delta\Omega\right]}. \tag{5.50}$$

By comparing Eq. (5.47) and Eq. (5.50), it is clear that the effect of adding an intracavity dispersive element is to modify the phase round-trip time as $\tau_p \Rightarrow \tau_p + \partial\psi/\partial\Delta\Omega|_0$. Inserting this into Eq. (5.48) results in a modified mode splitting of,

$$\delta = \frac{\Delta\varphi}{2\pi(\tau_p + \frac{\partial\psi}{\partial\Delta\Omega}\Big|_0)} = \frac{\frac{\Delta\varphi}{2\pi\tau_p}}{1 + \frac{1}{\tau_p}\frac{\partial\psi}{\partial\Delta\Omega}\Big|_0} = \frac{\delta_0}{1 + \frac{1}{\tau_p}\frac{\partial\psi}{\partial\Delta\Omega}\Big|_0}. \tag{5.51}$$

Clearly if there exists negative (anomalous) resonant group-velocity dispersion in the laser cavity such that, $\partial\psi/\partial\Delta\Omega|_0 < 0$, then the mode shift is enhanced. A mode splitting enhancement alone is not sufficient to prove a viable sensor improvement method. As described in Section 5.3, noise and instability prohibit the readout of mode splitting enhancement that may be present. In other words, it must be shown that the physical readout signal seen by the IPI detector, $D_b(\Delta\Omega)$ from Eq. 3.86, is not broadened so much that the beat frequency, $\Delta\nu$, can't be extracted.

Figure 5.4 shows the enhanced (solid) and non-enhanced (dashed) sensor response curve (red, left) and beat signal bandwidth (blue, right). The simulation was carried out by using Eq. (5.50) to solve for the enhanced response electric fields in place of Eq. (5.47) in the frequency domain model described in section 3.2.4. Fig. 5.4 plots the average beat frequency as a function of mode splitting (red, left axis) which is calculated similarly to how it would be measured in the lab as the center of gravity (first moment) of the beat signal spectrum,

$$\Delta\nu = \frac{1}{2\pi}\frac{\int_{-\infty}^{\infty}\Delta\Omega D_b(\Delta\Omega)d\Delta\Omega}{\int_{-\infty}^{\infty}D_b(\Delta\Omega)d\Delta\Omega}. \tag{5.52}$$

Enhancement in the sensitivity of the average beat frequency to the mode splitting is clearly shown as an increase in slope. The beat signal bandwidth is plotted in Fig. 5.4 (blue, right axis) as represented by the square root of the second moment of the beat

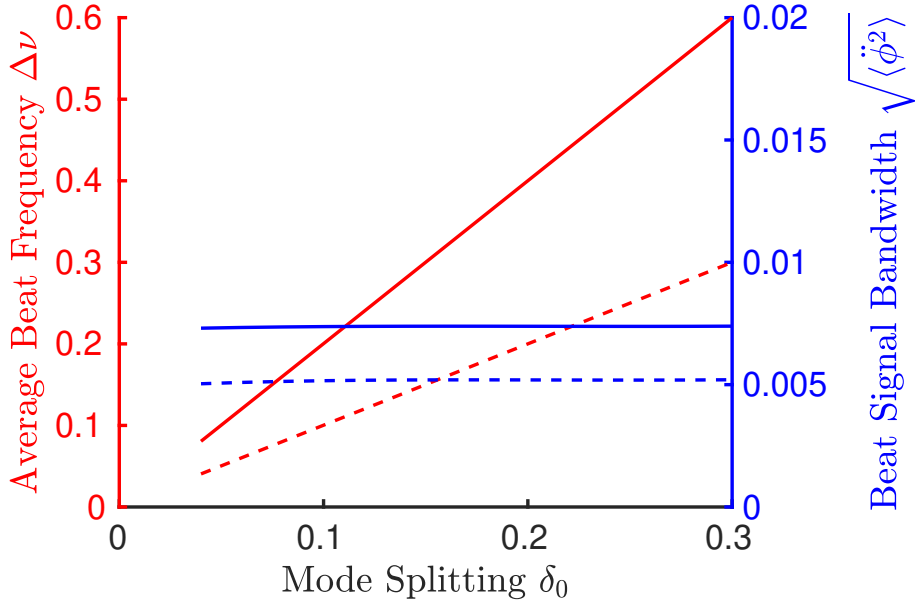

Figure 5.4: Enhanced (solid) and non-enhanced (dashed) sensor response curves. The average beat frequency (left axis, red) shows Eq. (5.52) plotted as function of the applied mode-splitting. The result of using the enhancement factor of $\partial\psi/\partial\Delta\Omega|_0 = -0.5$ acts to increase the sensitivity response (observed as the slope of the average beat frequency curve), without causing the noise to diverge as characterized by the beat signal bandwidth, Eq. (5.53) (right axis, blue). 150 round-trips were used in these calculations, without coupling, and gain parameters of $\alpha_0 = 1$, $\gamma = 0.05$, and $W_s = 1$.

signal,

$$\langle\ddot{\phi}^2\rangle = \frac{\int_{-\infty}^{\infty}(\Delta\Omega - 2\pi\Delta\nu)^2 D_b(\Delta\Omega)d\Delta\Omega}{\int_{-\infty}^{\infty} D_b(\Delta\Omega)d\Delta\Omega}. \tag{5.53}$$

The flat curves imply that the noise does not diverge like the EP enhancement since the coupling has been removed, $s = 0$. This calculation was carried out using $\tau_p = 1$, with 150 round-trips, gain parameters of $\alpha_0 = 1$, $\gamma = 0.05$, and $W_s = 1$, and an enhancement factor of $\partial\psi/\partial\Delta\Omega|_0 = -0.5$.

The enhancement described here is achieved by operating in the dispersive region of an absorbing resonance. This can be achieved experimentally by using an intracavity Gires-Tournois interferometer, a loop interferometer in a fiber laser, or using an active medium [67–69] .

Chapter 6

Genetic Algorithm

6.1 Introduction to Genetic Algorithms

As machine learning and deep neural networks have exploded in the computer science disciplines it was only a matter of time until their benefits were applied to optics. Artificial intelligence has been applied to optical design [70], initialized the development of so called "smart lasers" [71–73], and greatly improved reconstruction processes including ultrafast diagnostics [74], and imaging and super resolution [75–77], to name a few. The genetic algorithm (GA) developed here is an extremely versatile software tool that has found use throughout this research for reconstruction of ultrafast pulse phases, and cavity design. It has been developed in such a way that it can easily be catered to any individual future problem.

At the heart of machine learning is a minimization function. The computer needs a method to move from less correct to more correct solutions. A GA is an error minimization function that is frequently implemented in machine learning algorithms due to its ability to search large parameter spaces without falling into local minima [2, 78, 79].

The GA is a stochastic method that searches a parameter space similarly to how evolutionary biology optimizes organisms to an environment. An initial population

of solutions (solutions are termed chromosomes referring to the algorithm's biological roots) is first created. The most correct chromosomes are then allowed to mate and generate offspring which randomly include mutations. There are various methods with which to mate the chromosomes. As will be described in detail later, Binomial crossover is the mating method chosen here. It involves filling each element (or "gene") of a child chromosome with the corresponding element from one of two parents. Which parent offers its value to the child is randomly chosen for each element in the chromosome. In this way, subsequent generations of chromosomes drift closer to the optimum solution while the random mutations avoid local minima. These processes are known as:

- **Selection** - Choose which chromosomes in the population are the most correct and select them for mating. A fitness function quantifies how correct a solution is compared to the others.
- **Crossover** - Mate two chromosomes out of the selection pool to create offspring that have characteristics of both parents.
- **Mutation** - Mutations are randomly added to the genes of the offspring based on a user defined mutation rate.

GA's are separated into different types based on how each of these steps are implemented. The specific implementation developed for this dissertation is a differential evolution genetic algorithm (DEGA). The novelty of the DEGA lies in the fact that mutation and crossover depend on a differential function that is related to the variance in the population. This means that as the population coalesces to the ideal solution, the effective mutation rate decreases allowing for a faster convergence.

This specific DEGA was employed for two different use cases: an ultrafast diagnostic phase retrieval algorithm, and a thermal lensing reconstruction measurement. The implementation and functionality of the DEGA will be described below without going into detail about the specific use cases as they are not relevant to this dissertation.

6.2 Ultrafast diagnostic reconstruction

Cascaded nonlinearity inside a spectrometer (CaNIS) is an ultrafast diagnostic method that involves sending light to be analyzed through a nonlinear crystal, spectrometer and then a second nonlinear crystal [2]. Interference caused by the cascaded nonlinearity imprints the orginial pulse's phase onto the final measured signal. A reconstruction algorithm can then iteratively guess for a phase function that recreates the measured interference pattern. It has been shown that a DEGA performs quicker and more accurately than the ubiquitous Nelder-Mead (downhill simplex) algorithm when applied to d-scan phase reconstruction [74], thus it was decided that such an algorithm be implemented for CaNIS.

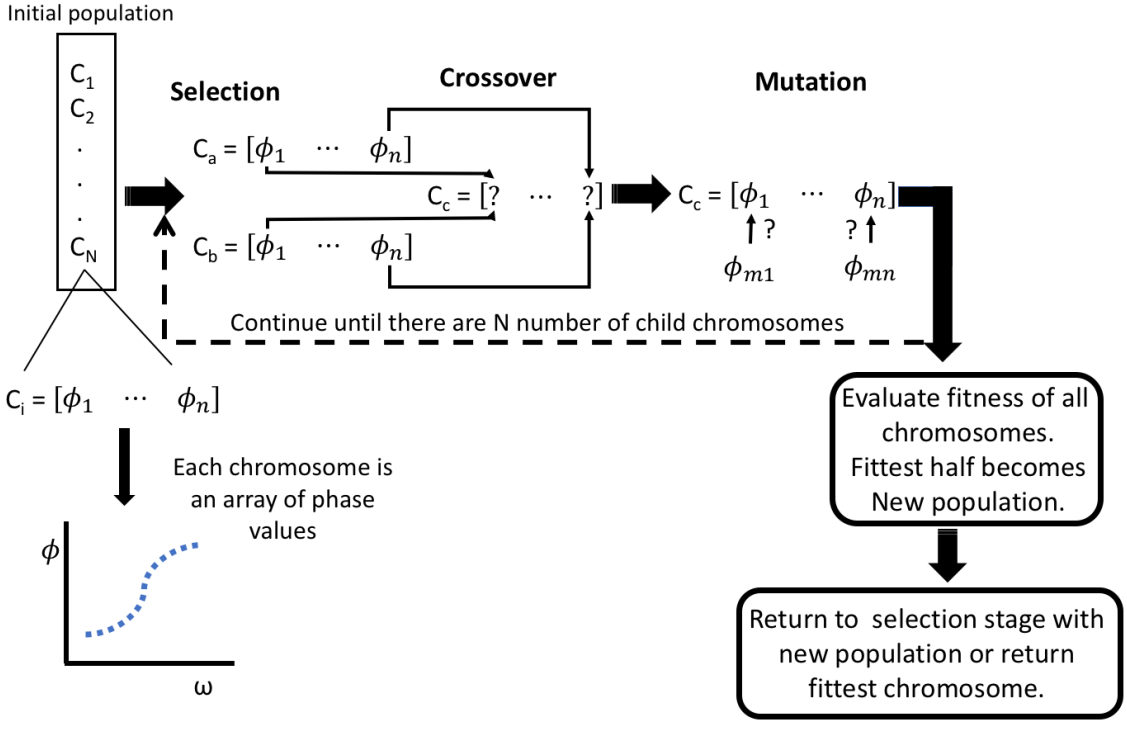

Figure 6.1: The three steps to a genetic algorithm are selection, crossover, and mutation. How these steps are implemented differs depending on the specific implementation. The differential evolution genetic algorithm used for this paper combines the crossover and mutation steps by using a differential mutation function, Eq. 6.1, to generate one of the parents used for crossover.

The DEGA developed for CaNIS reconstructs a phase value for every point in the

spectrum instead of searching for Taylor series coefficients like what is usually done in the Nelder-Mead algorithm. This allows the program the ability to reconstruct highly exotic phases. Fig. 6.1 shows the steps that are involved in the program which are described in detail below.

Initialization: A random number generator is used to generate an initial population of solutions/chromosomes. The number of chromosomes in a population, N, is defined by the user. Optimization of N is required since while a small population results in a lower probability of the correct chromosome occurring in a single population, a large population requires more time to calculate the next generation. Each chromosome is a $1\times n$ array with each element/gene being a phase value in the range $[-\pi, \pi]$, where n is the number of points used to decompose the measured spectra.

Step 1: Three chromosomes (C_a, C_b, C_c) are randomly chosen from the population. The chromosomes are then sorted in decreasing fitness such that C_a is the most accurate solution. The sorted chromosomes are then combined to create a mutation chromosome (MC) according to:

$$C_{\mathrm{MC}} = C_a + \beta(C_b - C_c), \tag{6.1}$$

where β is a random number on the interval $[0, 1]$. Notice that the MC is a high-fitness solution, C_a, modulated by the difference between two lower-fitness solutions, $C_b - C_c$. The β is included to randomize how strongly each element is modulated by that difference (β can be thought of as a variable mutation rate). If the population has a low variance, as should happen in later iterations of the algorithm, then the modulation term will be small because $C_b \approx C_c$. This means that the MC will not be much different from C_a, and the algorithm will quickly converge i.e. every chromosome in the population will essentially be the same.

Step 2: Two parents are required to develop a child chromosome for the next generation. The MC will be used as the first parent, so a second parent chromosome must be chosen randomly from the population. No limits were placed on the second parent so it is possible that the second parent could be one of the chromosomes used to create the MC.

Step 3: The child chromosome is created from the two parents using a process termed

Binomial Crossover, explained here: For each element in the child chromosome, a random number is generated on the interval $[0, 1]$. If the random number is less than a user defined crossover rate, then that element in the child chromosome is filled with the value in the corresponding element in the MC. Otherwise the element is filled from the corresponding element in the other parent chromosome. Once the offspring array is filled, a new MC is created using newly chosen ϕ_a, ϕ_b, ϕ_c, and β, and the process repeats until there are N number of offspring. At this point there will be 2N total chromosomes in memory (N from the original population plus N additional offspring)

Step 4: The fitness values of all 2N chromosomes are calculated and only the fittest half is kept for the next generation (which maintains the population size of N). The algorithm then repeats until a fitness tolerance or the maximum number of generations is reached at which point the chromosome with the highest fitness is returned.

Fig. 6.2 shows the result of a simulated DEGA reconstruction where the pulse had no second order (group-velocity) dispersion. This reconstruction is noteworthy because the Nelder-Nead method failed to accurately reconstruct the phase of such a pulse. The solid pink line shows the simulated phase and the circles are the successful DEGA reconstruction.

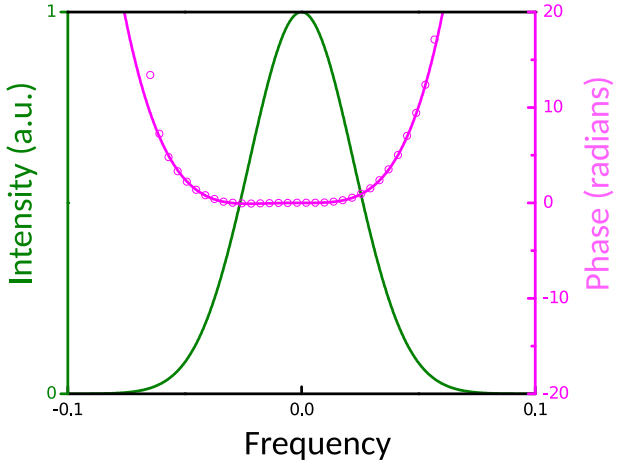

Figure 6.2: Simulated phase with no group-velocity dispersion (solid pink), and the DEGA phase reconstruction (pink circles).

6.3 Thermal lensing reconstruction

As optical powers of laser systems increase, so too do nonlinear effects. One common nonlinear effect is that of self-focusing. When light impinges on a nonlinear medium The light itself affects the index of that medium as $\Delta n = n_2 I$, where n_2 is the nonlinear index, and I is the light intensity. This means that a phase gradient proportional to the spatial beam profile will be imprinted on the material as the light propagates. If the spatial beam profile is Gaussian, the material picks up a Gaussian phase and a kerr lens is produced. A slower effect is caused by a temperature gradient in the material. Because the index of refraction also changes with temperature, a beam that is more intense in the middle than the outside (like a Gaussian beam) can induce a thermal lens by diferentially heating the material. These rogue lenses have to be accounted for in the design of high power amplifiers in order to establish stable cavities.

Many times theoretical knowledge of the power, thermal conductivity and nonlinear parameters that exist in a specific laser system cannot be fully known. Therefore, the most effective way of determining how strong a nonlinear lens will ultimately be is to experimentally measure the induced focal length under the operating criteria. In our case a Ti:Sapph nonlinear crystal to be used as the gain material for a regenerative amplifier was pumped with a 100 Watt Q-switched Nd:YAG frequency-doubled (532nm) Lee laser. The lens induced by this intense pumping needed to be known in order to design the amplifier cavity. Towards that end, an experiment was devised to measure just that.

While the crystal was being pumped by the Lee laser creating the artifical lens, a second (HeNe) laser with known spatial profile was sent through the crystal to probe the lens. By measuring the beam profile a known distance from the lens the parameters of the lens could be backed out. A sketch of the experimental design is shown in Fig. 6.3.

In order to back out the lens transfer function, the probe HeNe beam needed to be fully characterized. By measuring the HeNe beam profile at 2 locations in space, the

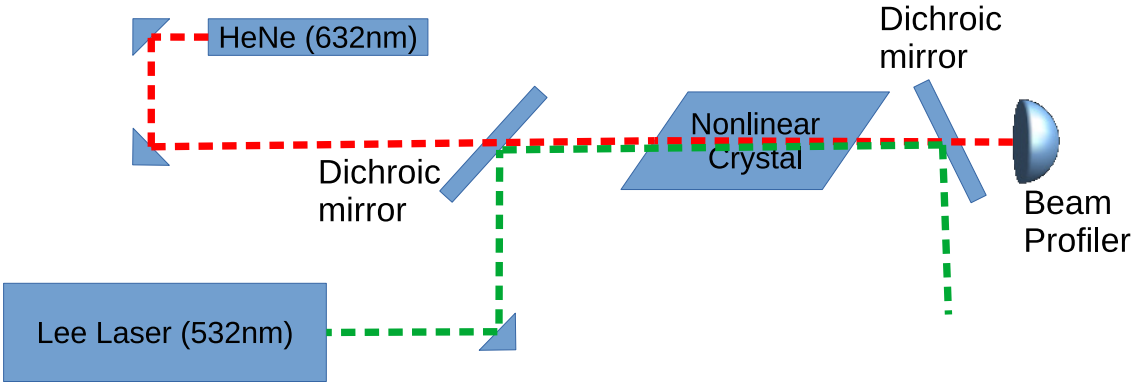

Figure 6.3: Experimental design to measure the thermal lens induced in the nonlinear crystal by the Lee Laser. By profiling the HeNe beam after traveling through the nonlinear crystal, the unknown properties of the thermal lens induced in the crystal can be deduced if the initial HeNe beam characteristics are known.

position and size of the beam waist could be calculated. This was first done using the Gaussian q-parameter, and then confirmed with the genetic algorithm reconstruction.

The complex q-parameter is an easy way to propagate the Gaussian envelope through space. It is defined as $q(z) = z + i\rho_0$ where z is the distance from the beam minimum waist and $\rho_0 = \pi w_0^2/\lambda$ is the Rayleigh length (w_0 being the minimum waist radius) [1]. The q-parameter is more often written as,

$$\frac{1}{q(z)} = \frac{1}{R(z)} - i\frac{1}{\rho(z)}, \tag{6.2}$$

where $R(z)$ is the radius of curvature of the Gaussian beam at position z, and,

$$\rho(z) = \pi w(z)^2/\lambda, \tag{6.3}$$

is related to the Rayleigh range in that $\rho(z = 0) = \rho(z_0) = \rho_0$. It can be shown that the beam radius at position z is defined as [80, 81] [2],

$$w(z) = w_0\sqrt{1 + \left(\frac{z}{\rho_0}\right)^2}, \tag{6.4}$$

[1] the sign of this equation is dependent on the choice of phase convention. This form assumes the convention of $\exp\{-i(kz - \omega t)\}$.

[2] In practice the beam diameter is also referred to as the spot size but these terms can be defined in slightly different ways. I will be explicit in my writing as to whether I am referring to the minimum beam diameter, $2w_0$, or the beam diameter at a specific location, $2w(z)$.

which by plugging Eq. 6.4 into Eq. 6.3 implies that,

$$\rho(z) = \rho_0 \left[1 + \left(\frac{z}{\rho_0} \right)^2 \right]. \tag{6.5}$$

In order to characterize the HeNe beam, the location of the minimum beam waist and the Rayleigh range must be extracted. This can be done knowing only the beam radius at two different locations in space, $w(z_1) = w_1$, $w(z_2) = w_2$ and the distance between those measurements, $\Delta z = z_2 - z_1$ [3]. Solving Eq. (6.5) for z, subtracting $z_2 - z_1$, and solving for ρ_0 leads to an expression for the rayleigh range in terms of the measurements,

$$\rho_0 = \frac{(\rho_1 + \rho_2)\Delta z^2 \pm \sqrt{\rho_1 \rho_2 \Delta z^4 - \Delta z^6}}{(\rho_1 - \rho_2)^2 + 4\Delta z^2}. \tag{6.6}$$

The exact location of the minimum beam waist can then be found in relation to the location of the initial measurement of ρ_1,

$$z_1 = \rho_0 \sqrt{\frac{\rho_1}{\rho_0} - 1} = \rho_0 \sqrt{\frac{w_1^2}{w_0^2} - 1}, \tag{6.7}$$

where z_1 is then the distance from the measurement location of w_1 to the minimum beam waist location. To discern which of the $\pm$ terms is the correct solution in Eq. (6.6), both values are tried in Eq. (6.7) and the most reasonable solution is chosen. The HeNe laser used for the experiment was measured to have $w_1 = 0.636$mm, $w_2 = 1.175$, and $\Delta z = 1,235$mm which led to a calculated minimum waist size of $w_0 = 0.4$mm that was 997.3mm behind the first measurement. This resulted in the effective minimum beam waist being 6.2cm behind the output opening of the HeNe outer casing.

This conclusion was confirmed by the GA which operated by guessing different values for the minimum beam waist and location, and then compared those guesses to the measured values by propagating the guessed beam forward in space according to the q-parameter propagation defined below. Fig. 6.4 shows the beam profile measurement at different places in space along the HeNe beam path (right) and the corresponding GA reconstruction at those spatial positions (left). The GA assumed

[3] Another experimental way to characterize the beam would be to take several waist measurements along the beam path and fit Eq. (6.4) to that data.

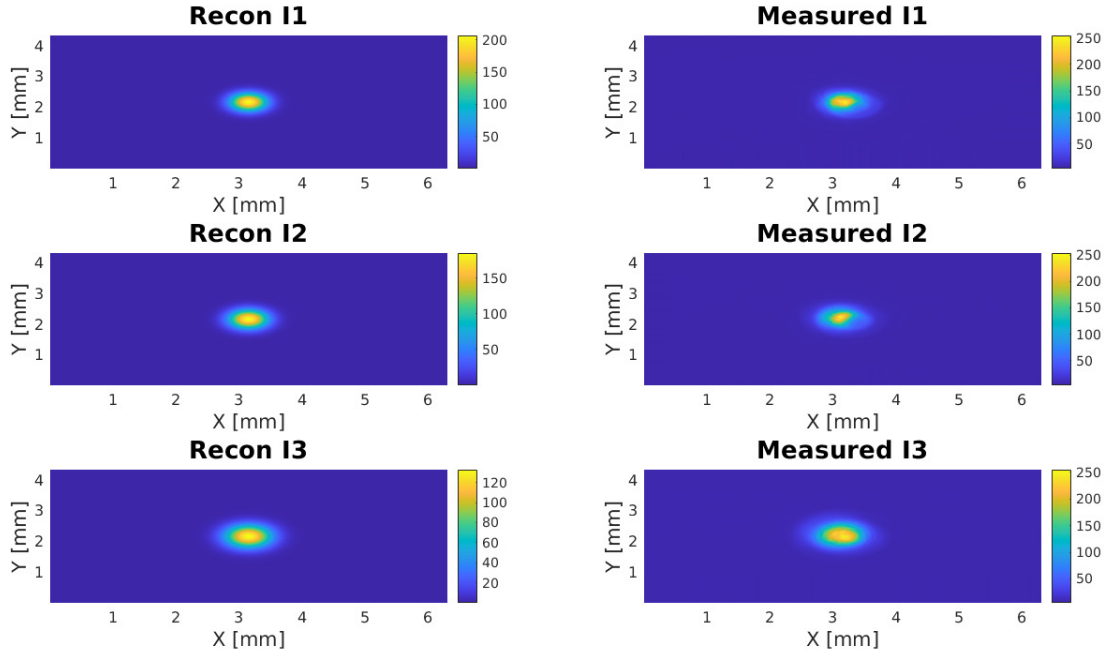

Figure 6.4: The Genetic Algorithm successfully found values for the minimum beam waist size and location that accurately reconstructed the HeNe spatial beam profile at three different locations in space. The left plots above show the GA reconstructions while the right plots show the corresponding measurements. Note that the x and y axes are set by the dimensions of the sensor used to profile the beam.

a perfect guassian at the minimum beam waist location and propagated that forward in space using the q-parameter ABCD matrix method.

The q-parameter is used to propagate a Gaussian beam through an optical system by applying the system's transfer ABCD matrix as,

$$\frac{1}{q_2} = \frac{(1/q_1)D + C}{(1/q_1)B + A}, \tag{6.8}$$

where q_2 defines the new gausian beam after propagating the q_1 beam through the system defined by the ABCD transfer matrix. Starting from the minimum beam waist of the HeNe laser characterized above, the ABCD matrix describing the air, thermal lens, then air propagation the beam encounters before being measured by the beam profiler is (see Fig. 6.5),

$$\begin{bmatrix} 1 - \frac{d_2}{f} & d_1 + d_2 - \frac{d_1 d_2}{f} \\ -\frac{1}{f} & 1 - \frac{d_1}{f}, \end{bmatrix} \tag{6.9}$$

where d_1 is the known distance from the minimum beam waist to the thermal lens, d_2 is the known distance from the thermal lens to the final measurement location, and f is the thermal lens focal length to be solved.

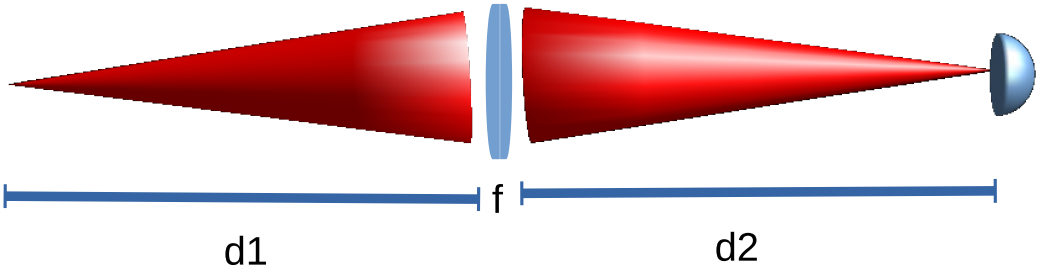

Figure 6.5: Propagation defined by the ABCD matrix of Eq. (6.9). This effective propagation models the experimental situation show in Fig. (6.3), where the nonlinear lens is represented by a thin lens.

There is now enough information to make an estimation of the thermal lens focal length. Since the radius of curvature is infinity at the beam waist, $q_1 = i\rho_0$. This q_1 can then be propagated through the system according to Eq. (6.9) using the measured $d_{1,2}$ values, and a guessed f. The final beam waist measured after the thermal lens is used to calculate ρ_2 which can be compared to the imaginary part of the q-parameter propagated through the simulated ABCD matrix lens with guessed focal length.

There are several ways of carrying out the calculation described above. As described, the genetic algorithm is no different than a simple minimization function that chooses an f that minimizes the error between the measured and calculated ρ_2. Because the radius of curvature that corresponds to the final measured q-parameter is difficult to measure, information is lost and it is not clear whether just the beam waist is sufficient to fully characterize the thermal lens. Additionally, the thermal lens has been treated as an ideal thin lens. Abberations and other beam shaping effects can't be accounted for in the simple minimization model defined above. Where the genetic algorithm may be better than a minimization function would be in a full 2D reconstruction of the phase transfer function of the lens. Instead of assuming a thin lens phase, the genetic algorithm can reconstruct a phase value for every pixel of measured amplitude. An alternative and less computationally heavy method would

be assuming a polynomial lens phase that the GA then solves for coefficients. For example, Fig. 6.6 shows the result of allowing the GA to reconstruct the coefficients, a, b, c, for the spherical phase of $-(a + bx^2 + cy^2)$.

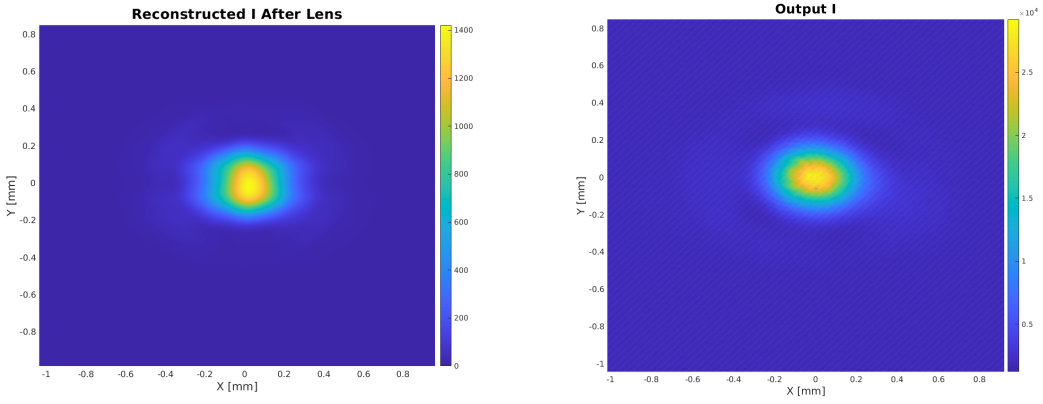

Figure 6.6: (a) shows the GA reconstruction of the measured spatial beam profile (b). The GA guessed coefficients for a perfect spherical lens phase.

This is carried out by again starting from the beam minimum waist with q-parameter, q_1, which is propagated to a measurement location *before* the thermal lens. This allows a phase to be applied to a measured amplitude before the lens. This 2D matrix of amplitudes and phases representing the beam can then be propagated to the lens, where the guessed lens transfer function is applied and then propagated to the final measurement location where the error between measured and reconstructed amplitudes can be calculated as the goodness of fit.

For the experimental measurement considered here the simple thin lens phase was sufficient to calculate the thermal lens focal point which rendered the GA unnecessary. It remains an open question whether there are cases where a GA could be used to fully characterize exotic lenses where the q-parameter method fails.

Chapter 7

Conclusion

The work summarized in this dissertation sets the stage for exciting future experiments. The first step is to achieve a beat response curve for the ring laser. Both a rotation table to physically rotate the sensor, and a variable intensity splitter to be used to adjust the kerr phase difference between the counter-propagating pulses are being developed currently. This will allow characterization of the bias beat frequency, and dead band (if one exists). Cross polarizing the counter-propagating pulses can be done to remove the lock-in if present. Additionally, full stabilization of the pump should reduce the beat frequency bandwidth down to the quantum limit. Amplitude stabilization by way of a feedback to the amplifier diodes was attempted without a significant improvement on the beat signal bandwidth, so cavity length stabilization of the pump is a next step. Once stabilization is successful, studies into the fundamental noise of the device can be conducted. A confirmation of the theoretical prediction that the noise is independent of detuning in the case of IPI can be made. Additionally, an experimental confirmation of the exceptional point induced noise broadening, similar to [56] can be achieved by placing the sensor at an exceptional point and observing the noise. Enhancement studies are another interesting prospect. Quantum squeezing and intracavity dispersion tailoring are both attractive options for further study. Since the conservative coupling beat response curve predicted here has never been observed experimentally, that would be another interesting topic to explore.

Predicting further into the future, since solid state devices are a much more realistic option for real world implementation, achieving IPI in an integrated device is the natural next progression. Clearly, IPI has a bright future in the sensing community with a lot more exciting research to come.

Appendix A

Different forms of the coupled-mode equations

The following is a similar derivation to that shown in Section 3.2, however, additional notational forms are included. The hope is that this can be used as a future reference to avoid confusion when comparing the various forms used in the literature.

Engineers typically take the phase to be $e^{+i\omega t}$, such that the electric field Ansatz takes the form of,

$$E = \frac{1}{2}\tilde{\mathcal{E}}(t,z)e^{i\omega t}. \tag{A.1}$$

Both sides of Eq. 3.29 can be multiplied by $\frac{1}{2}e^{i\omega t}$ to achieve,

$$\frac{1}{2}e^{i\omega t}\frac{\partial\tilde{\mathcal{E}}}{\partial t} = \frac{\beta}{2}E. \tag{A.2}$$

By way of the chain rule,

$$\frac{\partial E}{\partial t} = \frac{1}{2}e^{i\omega t}\frac{\partial\tilde{\mathcal{E}}}{\partial t} + i\omega E, \tag{A.3}$$

so that Eq. A.2 becomes,

$$\boxed{\frac{\partial E}{\partial t} = \frac{\beta}{2}E + i\omega E.} \tag{A.4}$$

Theoretical physicists typically take the phase to be $e^{-i\omega t}$ such that the Ansatz is,

$$E = \frac{1}{2}\tilde{\mathcal{E}}(t,z)e^{-i\omega t}. \tag{A.5}$$

Following the same argument as the previous subsection leads to Eq. 3.29 becoming,

$$\boxed{\frac{\partial E}{\partial t} = \frac{\beta}{2}E - i\omega E.} \tag{A.6}$$

The equations above are true for lone electric fields, however, to consider a two-level coupled-mode system we require equations that include coupling between two fields. This step is straight forward due to our choice to convert back to the full optical field. Though, depending on the choice of phase convention (engineering or physics), frame of reference, and whether the coupled-mode equations (CMEs) are in the form of the Schrödinger equation or not, different equivalent forms can be produced. We take a moment here to derive the 3 most common sets of equations so as to avoid confusion when looking at different papers.

Engineering fields oscillating at a cavity resonance frequency

Engineering notation of Eq. A.4 will be used as the starting point. The slowly varying amplitudes will be observed at their respective cavity resonant frequencies such that the Ansatz takes the form of,

$$E_{1,2} = \frac{1}{2}\tilde{\mathcal{A}}_{1,2}e^{i\omega_{1,2}t}. \tag{A.7}$$

In order to create a coupled-mode equation, we will introduce coupling between two optical fields with a simple complex constant, $K_{1,2}$. Where K_1 is coupling of the second electric field, E_2, into the first electric field, E_1, and K_2 is the opposite. Additionally, since we are considering a laser system, the propogation constant is replaced with a saturable gain term such that,

$$\frac{\beta_{1,2}}{2} = \alpha_{1,2} = \frac{\hat{\alpha}_{1,2}}{1 + \beta I_{1,2} + \gamma I_{2,1}} - \alpha_L. \tag{A.8}$$

The coupled-mode equations are then

$$\frac{\partial E_1}{\partial t} = (\alpha_1 + i\omega_1)E_1 + K_1 E_2 \tag{A.9}$$

$$\frac{\partial E_2}{\partial t} = (\alpha_2 + i\omega_2)E_2 + K_2 E_1. \tag{A.10}$$

To account for experimental realities the coupling constant is split into conservative, $\tilde{\kappa}$, and non-conservative, s, parts such that,

$$K_{1,2} = s_{1,2} + \tilde{\kappa}_{1,2}. \tag{A.11}$$

Conservative coupling means that $\tilde{\kappa}_1 = -\tilde{\kappa}_2^* = \tilde{\kappa}$ (this is a limiting case as shown in section 3.3). Plugging the Ansatz into Eq. A.10 with these changes and rearranging leads to the coupled-mode equations for the slowly varying amplitude,

$$\boxed{\begin{aligned}\frac{\partial \tilde{\mathcal{A}}_1}{\partial t} &= \alpha_1 \tilde{\mathcal{A}}_1 + (s + \tilde{\kappa})\tilde{\mathcal{A}}_2 e^{i\Delta t} \\ \frac{\partial \tilde{\mathcal{A}}_2}{\partial t} &= \alpha_2 \tilde{\mathcal{A}}_2 + (s - \tilde{\kappa}^*)\tilde{\mathcal{A}}_1 e^{-i\Delta t}.\end{aligned}} \tag{A.12}$$

Note that to arrive at the final form of Eq. A.12 the detuning has been defined as $\Delta = \omega_2 - \omega_1$. Also it has been assumed that $s_1 = s_2 = s$. The beating of these two signals in the lab frame will be,

$$\begin{aligned} D_b(t) = |E_1 + E_2|^2 &= |E_1|^2 + |E_2|^2 + E_1 E_2^* + E_1^* E_2 \\ &= \frac{1}{4}\left(|\tilde{\mathcal{A}}_1|^2 + |\tilde{\mathcal{A}}_2|^2 + \tilde{\mathcal{A}}_1 \tilde{\mathcal{A}}_2^* e^{-i\Delta t} + \tilde{\mathcal{A}}_1^* \tilde{\mathcal{A}}_2 e^{i\Delta t}\right). \end{aligned} \tag{A.13}$$

Eq. A.12 has no closed form solution since the Hamiltonian of that system does not commute with itself at different points in time. To obtain an analytic solution one must change basis as is done below.

Engineering fields oscillating at an average frequency

Another way to approach the problem is to observe the slowly varying amplitudes from a reference frame that oscillates at an average frequency. Many know this form as changing to the rotating frame. In this case the Ansatz takes the form of,

$$E_{1,2} = \frac{1}{2}\tilde{\mathcal{E}}_{1,2} e^{i\omega_a t}, \tag{A.14}$$

where $\omega_a = (\omega_1 + \omega_2)/2$. To derive the CMEs for the slowly varying amplitudes in this case, we can either derive them directly from Eq. 3.29, or begin from Eq. A.4 with the understanding that, due to the way it was derived, the ω in that equation is the corresponding cavity resonant frequency. This means that after including the coupling and gain,

$$\begin{aligned} \frac{\partial E_1}{\partial t} &= \alpha_1 E_1 + i\omega_1 E_1 + (s + \tilde{\kappa}) E_2 \\ \frac{\partial E_2}{\partial t} &= \alpha_2 E_2 + i\omega_2 E_2 + (s - \tilde{\kappa}^*) E_1. \end{aligned} \tag{A.15}$$

Plugging Eq. A.14 into Eq. A.15 results in a slowly varying amplitude CME of,

$$\boxed{\begin{aligned} \frac{\partial \tilde{\mathcal{E}}_1}{\partial t} &= \alpha_1 \tilde{\mathcal{E}}_1 - i\frac{\Delta}{2}\tilde{\mathcal{E}}_1 + (s + \tilde{\kappa})\tilde{\mathcal{E}}_2 \\ \frac{\partial \tilde{\mathcal{E}}_2}{\partial t} &= \alpha_2 \tilde{\mathcal{E}}_2 + i\frac{\Delta}{2}\tilde{\mathcal{E}}_2 + (s - \tilde{\kappa}^*)\tilde{\mathcal{E}}_1. \end{aligned}} \tag{A.16}$$

Note that $\Delta = 2(\omega_2 - \omega_a) = 2(\omega_a - \omega_1) = \omega_2 - \omega_1$ is the exact same as before since we have defined $\omega_a = (\omega_1 + \omega_2)/2$. In this case, the lab frame beat signal is calculated to be,

$$D_b(t) = |E_1 + E_2|^2 = \frac{1}{4}\left(|\tilde{\mathcal{E}}_1|^2 + |\tilde{\mathcal{E}}_2|^2 + \tilde{\mathcal{E}}_1\tilde{\mathcal{E}}_2^* + \tilde{\mathcal{E}}_1^*\tilde{\mathcal{E}}_2\right). \tag{A.17}$$

Eq. A.16 can be solved analytically by casting it into a matrix equation,

$$\begin{pmatrix} \dot{\tilde{\mathcal{E}}}_1 \\ \dot{\tilde{\mathcal{E}}}_2 \end{pmatrix} = \begin{bmatrix} \alpha_1 - i\Delta/2 & (s + \tilde{\kappa}) \\ (s - \tilde{\kappa}^*) & \alpha_2 + i\Delta/2 \end{bmatrix} \begin{pmatrix} \tilde{\mathcal{E}}_1 \\ \tilde{\mathcal{E}}_2 \end{pmatrix}, \tag{A.18}$$

which has a characteristic equation of the form,

$$\begin{vmatrix} \alpha_1 - i\Delta/2 - i\lambda & (s + \tilde{\kappa}) \\ (s - \tilde{\kappa}^*) & \alpha_2 + i\Delta/2 - i\lambda \end{vmatrix} = 0, \tag{A.19}$$

and eigenvalues of,

$$\lambda_\pm = -i\frac{\alpha_1 + \alpha_2}{2} \pm \frac{\zeta}{2}. \tag{A.20}$$

where $\zeta = \sqrt{4|\tilde{\kappa}|^2 - (\alpha_1 - \alpha_2 - i\Delta)^2 - 4s^2 - 4s(\tilde{\kappa} - \tilde{\kappa}^*)}$. Recalling that to find the eigenvectors we plug the eigenvalue back into the eigenvalue equation,

$$\boldsymbol{H}\,|v_\pm\rangle = \lambda_\pm\,|v_\pm\rangle \tag{A.21}$$

$$\boldsymbol{H} - \lambda_{\pm} |v_{\pm}\rangle = 0, \tag{A.22}$$

this leads to,

$$\begin{pmatrix} \alpha_1 - i\Delta/2 - i\lambda_{\pm} & s + \tilde{\kappa} \\ s - \tilde{\kappa}^* & \alpha_2 + i\Delta/2 - i\lambda_{\pm} \end{pmatrix} \begin{pmatrix} v_{1\pm} \\ v_{2\pm} \end{pmatrix} = 0. \tag{A.23}$$

The eigenvectors are then,

$$|v_{\pm}\rangle = \begin{bmatrix} 1 \\ \frac{\alpha_2 - \alpha_1 + i\Delta \pm i\zeta}{2(s+\tilde{\kappa})} \end{bmatrix} \tag{A.24}$$

which means that the two circulating electric fields take the form of,

$$\tilde{\mathcal{E}}_1(t) = c_+ e^{i\lambda_+ t} + c_- e^{i\lambda_- t} \tag{A.25}$$

$$\tilde{\mathcal{E}}_2(t) = c_+ \left(\frac{\alpha_2 - \alpha_1 + i\Delta + i\zeta}{2(s+\tilde{\kappa})} \right) e^{i\lambda_+ t} + c_- \left(\frac{\alpha_2 - \alpha_1 + i\Delta - i\zeta}{2(s+\tilde{\kappa})} \right) e^{i\lambda_- t}. \tag{A.26}$$

Using the initial conditions $\tilde{\mathcal{E}}_{1,2}(0)$ allows us to solve for the coefficients,

$$c_- = \frac{i}{2\zeta} \left[2(s+\tilde{\kappa})\tilde{\mathcal{E}}_2(0) - (\alpha_2 - \alpha_1 + i\Delta + i\zeta)\tilde{\mathcal{E}}_1(0) \right] \tag{A.27}$$

$$c_+ = \mathcal{E}_1(0) - c_-. \tag{A.28}$$

The equivalence between these amplitudes and the cavity resonant frequency amplitudes of the previous section are,

$$\begin{aligned} \tilde{\mathcal{A}}_1 &= \tilde{\mathcal{E}}_1 e^{i(\Delta/2)t} \\ \tilde{\mathcal{A}}_2 &= \tilde{\mathcal{E}}_2 e^{-i(\Delta/2)t}. \end{aligned} \tag{A.29}$$

Physics fields oscillating at an average frequency with Schrödinger notation

When applying quantum mechanical methods to this two-level system it is useful to map it into the same syntax used by that field. This means we will use the physics phase convention with the fields oscillating at the average frequency,

$$E_{1,2} = \frac{1}{2} \tilde{\psi}_{1,2} e^{-i\omega_a t}. \tag{A.30}$$

Because the Schrödinger equation is of the form $i\dot{\Psi} = H\Psi$, we must multiply Eq. A.6 by the imaginary unit on both sides to achieve (after including gain and coupling),

$$\begin{aligned} i\frac{\partial E_1}{\partial t} &= i\alpha_1 E_1 + \omega_1 E_1 + iK_1 E_2 \\ i\frac{\partial E_2}{\partial t} &= i\alpha_2 E_2 + \omega_2 E_2 + iK_2 E_1. \end{aligned} \tag{A.31}$$

Most of the papers that use this notation only consider conservative coupling such that $s = 0$. Due to the addition of the imaginary unit in front of the coupling constant the conservative coupling relation changes a bit such that $K_1 = K_2^* = \tilde{\kappa}_0 = i\tilde{\kappa}$. Plugging in the Ansatz results in,

$$\boxed{\begin{aligned} i\frac{\partial \tilde{\psi}_1}{\partial t} &= i\alpha_1 \tilde{\psi}_1 - \frac{\Delta}{2}\tilde{\psi}_1 + i\tilde{\kappa}_0 \tilde{\psi}_2 \\ i\frac{\partial \tilde{\psi}_2}{\partial t} &= i\alpha_2 \tilde{\psi}_2 + \frac{\Delta}{2}\tilde{\psi}_2 + i\tilde{\kappa}_0^* \tilde{\psi}_1. \end{aligned}} \tag{A.32}$$

Appendix B

Walk-off calculation

The group delay, $\Delta\tau$, between two pulses with different central frequencies (ω_1, ω_2) that travel through a length of fiber, L, is defined,

$$\Delta\tau = \frac{L}{v_g(\omega_1)} - \frac{L}{v_g(\omega_2)}, \tag{B.1}$$

where v_g is the group velocity curve of the specific fiber under consideration. Recall that the first derivative of the effective mode propagation constant, k, is related to the group velocity according to,

$$\frac{dk}{d\Omega} = \frac{1}{v_g}. \tag{B.2}$$

This allows the group delay to be rewritten,

$$\Delta\tau = L\left(\frac{dk}{d\Omega}\Big|_{\omega_1} - \frac{dk}{d\Omega}\Big|_{\omega_2}\right) \approx L\frac{d^2k}{d\Omega^2}\Big|_{\omega_1}\Delta\Omega = LD(\lambda_1)\Delta\lambda, \tag{B.3}$$

where the $\approx$ is a simple calculus tangent line approximation with, $\Delta\Omega = \omega_2 - \omega_1$, and the final equality is the definition of the fiber Dispersion parameter, D. A power series expansion of $\Delta\lambda$ can be made such that,

$$\frac{\Delta\tau}{L} = D(\lambda_1)\Delta\lambda + \frac{1}{2}\frac{dD}{d\lambda}\Big|_{\lambda_1}\Delta\lambda^2 + \frac{1}{6}\frac{d^2D}{d\lambda^2}\Big|_{\lambda_1}\Delta\lambda^3. \tag{B.4}$$

Assuming the expansion wavelength, λ_1, is the zero dispersion wavelength of the chosen fiber such that $D(\lambda_1) = 0$, simplifies the group delay difference to,

$$\Delta\tau = \left(\frac{1}{2}\frac{dD}{d\lambda}\Delta\lambda^2 + \frac{1}{6}\frac{d^2D}{d\lambda^2}\Delta\lambda^3\right)L, \tag{B.5}$$

which is exactly the expression given in [50]. This allows the walk-off between a pump pulse, assumed to be near the zero dispersion wavelength, and a parametric pulse a distance $\Delta\lambda$ away from the pump to be estimated using only the dispersion slope and slope derivative evaluated at the zero dispersion wavelength.

Appendix C

Genetic Algorithm Code

This Genetic Algorithm was written in such a way that it could be tailored easily to different problems. When applying this minimization function to a specific problem, most of the work will go into defining the fitness function (fitFun), which tells the genetic algorithm how to rank the population of chromosomes from best to worst. Note that in the code below "data" is an array that is simply passed to fitFun and so is specific to each implementation.

```
1  function [ globalMaxChrm, globalMaxFit ] = genA(fitFun, data, ...
       chrmSize, popSize, numGens, crossRate, domains)
2  %Genetic Algorithm
3  %Luke Horstman
4  %01/26/2018
5  %   1) Generate Population
6  %   2) Evaluate Fitness
7  %   3) Crossover (mating)
8  %   4) Mutate
9  %   5) Repeat
10
11 %chrmSize:  Number of genes in a chromosome
12 %popSize:   Number of chromosomes in a generation
```

```
13 %numGens:   Number of generations to iterate through
16 %crossRate: Crossover Rate (between 0-1)
17 %fitFun:    Fitness Function (must be a function handle)
18 %           Note the function must accept an array as input ...
      which will have
19 %           as many elements as chrmSize
20 %data:      Data for fitness function
21 %domains:   range of values phase can take goes from -domains ...
      to +domains
22
23 %% Generate Population
24 %generate population with random number between 0-1
25 %Each row of matrix is a different chromosome
26 pop = 2*rand(popSize,chrmSize)-1;
27 %adjust each gene so that they fall within their domain
28 pop = domains*pop;
29 %initialize maxes
30 currentMaxFit = 0;
31 currentMaxChrm = zeros(1,chrmSize);
32 globalMaxFit = 0;
33 globalMaxChrm = zeros(1,chrmSize);
34
35 %% Begin Iterating Through Generations
36 for i = 1:numGens
37     % there is no nextpop on first iteration
38     if i ~= 1
39         pop = nextPop;
40     end
41
42     %Evaluate Fitness of every chromosome
43     fitness = zeros(popSize,1);
44     for j = 1:size(pop,1)
45         fitness(j) = fitFun(pop(j,:), data);
```

```
46      end
49      % sort population based on fitness
50      [sortFit,fitIndex] = sort(fitness,'descend');
51      pop = pop(fitIndex,:);
52      %trim least fit chromosomes to population is correct size
53      pop = pop(1:popSize,:);
54
55      %% Display Diagnostic Data Of This Gen
56      currentMaxFit = sortFit(1);
57      currentMaxChrm = pop(1,:);
58      fprintf('Generation %d\tMax Fitness: ...
           %.4f\n',i,currentMaxFit);
59
60      if(currentMaxFit > globalMaxFit)
61          globalMaxFit = currentMaxFit;
62          globalMaxChrm = currentMaxChrm;
63      end
64
65      %% Esmerando Mutation and Crossover
66      % Best of Random Differential Evolution
67      % select 3 random members of population and sort based on ...
           fitness
68      % do this for every chromosome in population
69      childPop = zeros(popSize,chrmSize);
70      for j = 1:popSize
71          %ensure that chosen doners are not the same as each other
72          randMems = zeros(1,3);
73          while length(randMems) ≠ length(unique(randMems))
74          randMems = randi(popSize,[1,3]);
75          end
76          %sort donors based on fitness
77          [¬,fitIndices] = sort(fitness(randMems),'descend');
78          sortRandMems = randMems(fitIndices);
```

```
79          mem1 = pop(sortRandMems(1),:);
82          mem2 = pop(sortRandMems(2),:);
83          mem3 = pop(sortRandMems(3),:);
84          %create mutation chromosome from random members
85          mute = mem1 + rand(1,chrmSize).*(mem2-mem3);
86
87          %choose random parent
88          parent = pop(randi(popSize),:);
89          %create offspring by binomial crossover of parent and ...
               mutation
90          child = zeros(1,chrmSize);
91          for k = 1:chrmSize
92              if rand < crossRate
93                  child(k) = mute(k);
94              else
95                  child(k) = parent(k);
96              end
97          end
98          childPop(j,:) = child;
99      end
100
101     %add all children to population
102     nextPop = [pop;childPop];
103
104 end
105
106 end
```

References

[1] M. Navarro, O. Chalus, and Jean-Claude Diels. Mode-locked ring lasers for backscattering measurement of mirror. *Optics Letters*, 31:2864–2866, 2006. x, 18

[2] Ning Hsu, Luke Horstman, and Jean-Claude Diels. Pulse characterization by cascading nonlinearity inside a spectrometer (CaNIS). In Bahram Jalali, Daniel R. Solli, and Günter Steinmeyer, editors, *Real-time Measurements, Rogue Phenomena, and Single-Shot Applications III*, volume 10517, pages 45 – 56. International Society for Optics and Photonics, SPIE, 2018. 1, 89, 91

[3] Ning Hsu. *Ultrashort Pulses and Frequency Combs: Characterizations, Manipulations, and Applications*. PhD thesis, The University of New Mexico, Albuquerque, New Mexico, 2020.

[4] Hanieh Afkhamiardakani. *Generation of Correlated Dual Frequency Combs With PM Fiber Lasers for High-Precision Metrology*. PhD thesis, The University of New Mexico, Albuquerque, New Mexico, 2020. 44, 59, 64, 66

[5] James Hendrie. *Tailored Frequency Comb Structures and Their Sensing Applictions*. PhD thesis, The University of New Mexico, Albuquerque, New Mexico, 2019. 1

[6] R. J. Jones, J. C. Diels, J. Jasapara, and W. Rudolph. Stabilization of the frequency, phase, and repetition rate of an ultra-short pulse train to a Fabry-Perot reference cavity. *Optics Comm.*, 175:409–418, 2000. 3, 7

[7] Ronald N. Bracewell. *The Fourier transform and its applications*. McGraw-Hill electrical and electronic engineering series. McGraw-Hill, 3rd edition, 1999. 4

[8] Joseph W. Goodman. *Introduction to Fourier optics*. McGraw-Hill Electrical and Computer Engineering. McGraw-Hill, 1996. 4

[9] Ladan Arissian and Jean-Claude Diels. Investigation of carrier to envelope phase and repetition rate — fingerprints of mode-locked laser cavities. *Journal of Physics B: At. Mol. Opt. Phys*, 42:183001, 2009. 7

[10] L. Arissian and J.-C. Diels. Intracavity phase interferometry: frequency comb sensors inside a laser cavity. *Laser Photonics Rev*, 8:799–826, 2014. 9

[11] F. Aronowitz and R. J. Collins. Lock-in and intensity-phase interaction in the ring laser. *J. Appl. Phys.*, 41:130–141, 1970. 10

[12] W. W. Chow, J. Gea-Banacloche, L. M. Pedrotti, V. E. Sanders, W. Schleich, and M. O. Scully. The ring laser gyro. *Rev. Mod. Phys.*, 57:61–104, Jan 1985. 18

[13] R. J. C. Spreeuw, R. Centeno Neelen, N. J. van Druten, E. R. Eliel, and J. P. Woerdman. Mode-coupling in a He-Ne laser with backscattering. *Physical Review A*, 42(7):4315–4324, October 1990. 10, 28

[14] Andreas Schmitt-Sody, Ladan Arissian, Andreas Velten, Jean-Claude Diels, and Dave Smith. Rabi cycling of two pulses in a mode-locked ring laser cavity with electro-optical control. *Physical Review A*, 78:063802, 2008. 11, 76

[15] Heming Wang, Yu-Hung Lai, Zhiquan Yuan, Myoung-Gyun Suh, and Kerry Vahala. Petermann-factor sensitivity limit near an exceptional point in a brillouin ring laser gyroscope. *Nature Communications*, 11(1):1610, Mar 2020. 14

[16] J. Ren, H. Hodaei, G. Harari, A. U. Hassan, W. Chow, M. Soltani, D. Christodoulides, and M. Khajavikhan. Ultrasensitive micro-scale parity-time-symmetric ring laser gyroscope. *Opt. Lett.*, 42(8):1556–1559, Apr 2017. 28, 76, 82

[17] Ramy El-Ganainy, Konstantinos G. Makris, Mercedeh Khajavikhan, Ziad H. Musslimani, Stefan Rotter, and Demetrios N. Christodoulides. Non-hermitian physics and pt symmetry. *Nature Physics*, 14(1):11–19, Jan 2018. 71

[18] Jan Wiersig. Review of exceptional point-based sensors. *Photon. Res.*, 8(9):1457–1467, Sep 2020. 28, 71, 76

[19] David D. Smith, Hongrok Chang, Luke Horstman, and Jean-Claude Diels. Parity-time-symmetry-breaking gyroscopes: lasing without gain and subthreshold regimes. *Opt. Express*, 27(23):34169–34191, Nov 2019. 28, 71, 72, 84

[20] Luke Horstman, Ning Hsu, James Hendrie, David Smith, and Jean-Claude Diels. Exceptional points and the ring laser gyroscope. *Photon. Res.*, 8(3):252–256, Mar 2020. 22, 28, 71, 72, 79, 82, 84

[21] Bo Peng, Sahin Kaya Ozdemir, Fuchuan Lei, Faraz Monifi, Mariagiovanna Gianfreda, Gui Lu Long, Shanhui Fan, Franco Nori, Carl M. Bender, and Lan Yang. Parity-time-symmetric whispering-gallery microcavities. *Nature Physics*, 10(5), 2014.

[22] Mohammad P. Hokmabadi, Alexander Schumer, Demetrios N. Christodoulides, and Mercedeh Khajavikhan. Non-hermitian ring laser gyroscopes with enhanced sagnac sensitivity. *Nature*, 576(7785):70–74, Dec 2019. 14, 76

[23] J.-C. Diels and Wolfgang Rudolph. *Ultrashort laser pulse phenomena*. Elsevier, ISBN 0-12-215492-4; second edition, Boston, 2006. 28, 36

[24] A. Yariv. Universal relations for coupling of optical power between microresonators and dielectric waveguides. *Electronics Letters*, 36:321–322(1), February 2000. 28

[25] Xuan Mao, Guo-Qing Qin, Hong Yang, Hao Zhang, Min Wang, and Gui-Lu Long. Enhanced sensitivity of optical gyroscope in a mechanical parity-time-symmetric system based on exceptional point. *New Journal of Physics*, 22(9):093009, sep 2020. 28

[26] B.E.A. Saleh and M.C. Teich. Chapter 7 - photonics-crystal optics. In *Fundamentals of Photonics (Second Edition)*, Wiley Series in Pure and Applied Optics, pages 243–288. Wiley, second edition edition, 2007. 30

[27] M. G. Sagnac. L'éther lumineux démontré par l'effet du vent relatif d'éther dans un interféromètre en rotation uniforme. *Comptes Rendus*, 157:708–710, 1913. 43

[28] M. G. Sagnac. Sur la preuve de la réalité de l'éther lumineux démontré par l'expérience de l'interférographe tournant. *Comptes Rendus*, 157:1410–1413b, 1913. 43

[29] Vittorio M. N. Passaro, Antonello Cuccovillo, Lorenzo Vaiani, Martino De Carlo, and Carlo Edoardo Campanella. Gyroscope technology and applications: A review in the industrial perspective. *Sensors*, 17(10), 2017. 43

[30] Matthew J. Bohn, Jean-Claude Diels, and R. K. Jain. Measuring intracavity phase changes using double pulses in a linear cavity. *Optics Lett.*, 22:642–644, 1997. 44

[31] K. O. Hill, D. C. Johnson, B. S. Kawasaki, and R. I. MacDonald. cw three-wave mixing in single-mode optical fibers. *Journal of Applied Physics*, 49(10):5098–5106, 1978. 45

[32] Govind P. Agrawal. Chapter 10 - four-wave mixing. In Govind P. Agrawal, editor, *Nonlinear Fiber Optics (Fourth Edition)*, Optics and Photonics, pages 368–423. Academic Press, San Diego, fourth edition edition, 2006. 46

[33] Michel E. Marhic. *Fiber Optical Parametric Amplifiers, Oscillators and Related Devices*. Cambridge University Press, 2008. 49, 50, 57

[34] Robert W. Boyd. Chapter 2 - wave-equation description of nonlinear optical interactions. In Robert W. Boyd, editor, *Nonlinear Optics (Third Edition)*, pages 69–133. Academic Press, Burlington, third edition edition, 2008. 46

[35] N. Shibata, R. Braun, and R. Waarts. Phase-mismatch dependence of efficiency of wave generation through four-wave mixing in a single-mode optical fiber. *IEEE Journal of Quantum Electronics*, 23(7):1205–1210, 1987. 49

[36] K. Inoue. Four-wave mixing in an optical fiber in the zero-dispersion wavelength region. *Journal of Lightwave Technology*, 10(11):1553–1561, 1992. 49

[37] S. J. Jung, J. Y. Lee, and D. Y. Kim. Novel phase-matching condition for a four wave mixing experiment in an optical fiber. *Opt. Express*, 14(1):35–43, Jan 2006. 49

[38] J. Hansryd, P.A. Andrekson, M. Westlund, Jie Li, and P.-O. Hedekvist. Fiber-based optical parametric amplifiers and their applications. *IEEE Journal of Selected Topics in Quantum Electronics*, 8(3):506–520, 2002. 49

[39] M. Marhic. *Fiber Optical Parametric Amplifiers, Oscillators and Related Devices*. Cambridge University Press, New York, NY, 2008. 50

[40] G. K. L. Wong, S. G. Murdoch, R. Leonhardt, J. D. Harvey, and V. Marie. High-conversion-efficiency widely-tunable all-fiber optical parametric oscillator. *Opt. Express*, 15(6):2947–2952, Mar 2007.

[41] Yue Zhou, Bill P. P. Kuo, Kim K. Y. Cheung, Sigang Yang, P. C. Chui, and Kenneth K. Y. Wong. Wide-band generation of picosecond pulse using fiber optical parametric amplifier and oscillator. *IEEE Journal of Quantum Electronics*, 45(11):1350–1356, 2009.

[42] Yue Zhou, Kim K. Y. Cheung, Sigang Yang, P. C. Chui, and Kenneth K. Y. Wong. Widely tunable picosecond optical parametric oscillator using highly nonlinear fiber. *Opt. Lett.*, 34(7):989–991, Apr 2009.

[43] Darwin K. Serkland and Prem Kumar. Tunable fiber-optic parametric oscillator. *Opt. Lett.*, 24(2):92–94, Jan 1999.

[44] Yujun Deng, Qiang Lin, Fei Lu, Govind P. Agrawal, and Wayne H. Knox. Broadly tunable femtosecond parametric oscillator using a photonic crystal fiber. *Opt. Lett.*, 30(10):1234–1236, May 2005. 50

[45] Andreas Velten, Andreas Schmitt-Sody, and Jean-Claude Diels. Precise intracavity phase measurement in an optical parametric oscillator with two pulses per cavity round-trip. *Optics Letters*, 35:1181–1183, 2010. 51

[46] R. Gowda, N. Nguyen, J.-C. Diels, R. Norwood, N. Peyghambarian, and K. Kieu. All-fiber bidirectional optical parametric oscillator for precision sensing. *Optics Letters*, 40:2033–2036, 2015. 51

[47] Jes Broeng, Thomas Søndergaard, Stig E Barkou, Pablo M Barbeito, and Anders Bjarklev. Waveguidance by the photonic bandgap effect in optical fibres. *Journal of Optics A: Pure and Applied Optics*, 1(4):477–482, jan 1999. 51

[48] W. H. Reeves, D. V. Skryabin, F. Biancalana, J. C. Knight, P. St. J. Russell, F. G. Omenetto, A. Efimov, and A. J. Taylor. Transformation and control of ultra-short pulses in dispersion-engineered photonic crystal fibres. *Nature*, 424(6948):511, 2003. 51

[49] WJ Wadsworth, N Joly, JC Knight, TA Birks, F Biancalana, and PSJ Russell. Supercontinuum and four-wave mixing with q-switched pulses in endlessly single-mode photonic crystal fibres. *OPTICS EXPRESS*, 12(2):299 – 309, 2004. 51

[50] Masaaki Hirano, Tetsuya Nakanishi, and Takashi Sasaki. Highly nonlinear fiber with reduced dispersion slope and efficient wavelength conversion with sub-ps walk-off. In *OFC/NFOEC 2008 - 2008 Conference on Optical Fiber Communication/National Fiber Optic Engineers Conference*, pages 1–3, 2008. 58, 110

[51] Alexander A Krylov, Dmitry S Chernykh, and Elena D Obraztsova. Colliding-pulse hybridly mode-locked erbium-doped all-fiber soliton gyrolaser. *Laser Physics*, 28:015103, 2018. 71

[52] A.Zavadilová, D. Vyhlidal, V. Kubecek, and J. Sulc. Subharmonic synchronously intracavity pumped picosecond optical parametric oscillator for intracavity phase interferometry. *Laser Physics Letters*, 11:125403–125409, 2014.

[53] Shermineh Rostami, J.-C. Diels, and L. Arissian. Polarization evolution of ultrashort pulses in air. *Optics Express*, 23:3299–3307, 2015. 71

[54] Carl M. Bender and Stefan Boettcher. Real spectra in non-hermitian hamiltonians having p-$t$symmetry. *Phys. Rev. Lett.*, 80:5243–5246, Jun 1998. 71, 73

[55] David D. Smith and Hongrok Chang. Excess noise: why exceptional points do not increase sensor precision. arXiv 2005.12213, 2020. 71, 72, 80, 82

[56] Heming Wang, Yu-Hung Lai, Zhiquan Yuan, Myoung-Gyun Suh, and Kerry Vahala. Petermann-factor sensitivity limit near an exceptional point in a brillouin ring laser gyroscopet. *Nature Communications*, 11:1610–1615, 2020. 71, 80, 101

[57] G. S. Pati, M. Salit, K. Salit, and M. S. Shahriar. Demonstration of a tunable-bandwidth white-light interferometer using anomalous dispersion in atomic vapor. *Phys. Rev. Lett.*, 99:133601, Sep 2007. 72, 82

[58] M. Salit, G. S. Pati, K. Salit, and M. S. Shahriar. Fast-light for astrophysics: super-sensitive gyroscopes and gravitational wave detectors. *Journal of Modern Optics*, 54(16-17):2425–2440, 2007.

[59] M. S. Shahriar, G. S. Pati, R. Tripathi, V. Gopal, M. Messall, and K. Salit. Ultrahigh enhancement in absolute and relative rotation sensing using fast and slow light. *Physical review A*, 75:053807, 2007. 72, 82

[60] K. Petermann. Calculated spontaneous emission factor for double-heterostructure injection lasers with gain-induced waveguiding. *IEEE Journal of Quantum Electronics*, 15(7):566–570, 1979. 72, 80

[61] Tamar Goldzak, Alexei A. Mailybaev, and Nimrod Moiseyev. Light stops at exceptional points. *Phys. Rev. Lett.*, 120:013901, Jan 2018. 76

[62] Ramy El-Ganainy, Konstantinos G. Makris, Mercedeh Khajavikhan, Ziad H. Musslimani, Stefan Rotter, and Demetrios N. Christodoulides. Non-hermitian physics and pt symmetry. *Nature Physics*, 14:11, Jan 2018. Review Article.

[63] Johanna Miller. Exceptional points make for exceptional sensors. *Physics Today*, 70:23, 2017. 76

[64] W. A. Hamel and J. P. Woerdman. Observation of enhanced fundamental linewidth of a laser due to nonorthogonality of its longitudinal eigenmodes. *Phys. Rev. Lett.*, 64:1506–1509, Mar 1990. 80

[65] G.H.C. New. The origin of excess noise. *Journal of Modern Optics*, 42(4):799–810, 1995. 81

[66] J.-C. Diels and I. C. McMichael. Influence of wavefront conjugated coupling in the operation of a laser gyro. *Opt. Lett.*, 6:219–221, 1981. 84

[67] Jean-Claude Diels, Luke Horstman, Ning Hsu, and James Hendrie. Limits of resolution for sensors based on correlated frequency combst. In *CLEO: 2021*, volume 11700, page STu2A.7, San Jose, CA, 2021. Optical Society of America. 87

[68] A. Van Engen, Scott Diddams, and T. S. Clement. Dispersion measurements of water using white light interferometry. *Appl. Opt.*, 37:5679–5686, 1998.

[69] James Hendrie, Matthias Lenzner, Hanieh Akhamiardakani, Jean-Claude Diels, and Ladan Arissian. Impact of resonant dispersion on the sensitivity of intracavity phase interferometry and laser gyros. *Optics Express*, 24:30402–304010, 2016. 87

[70] Tong Yang, Dewen Cheng, and Yongtian Wang. Direct generation of starting points for freeform off-axis three-mirror imaging system design using neural network based deep-learning. *Opt. Express*, 27(12):17228–17238, Jun 2019. 89

[71] J. Nathan Kutz and Steven L. Brunton. Machine learning for self-tuning optical systems. In *Nonlinear Optics (NLO)*, page NTh1A.1. Optical Society of America, 2019. 89

[72] R. I. Woodward and E. J. R. Kelleher. Towards 'smart lasers': self-optimisation of an ultrafast pulse source using a genetic algorithm. *Scientific Reports*, 6(1):37616, Nov 2016.

[73] R. I. Woodward and E. J. R. Kelleher. Genetic algorithm-based control of birefringent filtering for self-tuning, self-pulsing fiber lasers. *Opt. Lett.*, 42(15):2952–2955, Aug 2017. 89

[74] Esmerando Escoto, Ayhan Tajalli, Tamas Nagy, and Günter Steinmeyer. Advanced phase retrieval for dispersion scan: a comparative study. *J. Opt. Soc. Am. B*, 35(1):8–19, Jan 2018. 89, 91

[75] Reuben A. Farrugia and Christine Guillemot. Light field super-resolution using a low-rank prior and deep convolutional neural networks. *IEEE Transactions on Pattern Analysis and Machine Intelligence*, 42(5):1162–1175, 2020. 89

[76] Baurzhan Muminov and Luat T. Vuong. Fourier optical preprocessing in lieu of deep learning. *Optica*, 7(9):1079–1088, Sep 2020.

[77] Wenxiao Wang, Fan Ye, Hao Shen, Nicholas A. Moringo, Chayan Dutta, Jacob T. Robinson, and Christy F. Landes. Generalized method to design phase masks for 3d super-resolution microscopy. *Opt. Express*, 27(3):3799–3816, Feb 2019. 89

[78] Melanie Mitchell. *An Introduction to Genetic Algorithms*. MIT Press, Cambridge, MA, USA, 1996. 89

[79] Rainer Storn and Kenneth Price. Differential evolution – a simple and efficient heuristic for global optimization over continuous spaces. *Journal of Global Optimization*, 11(4):341–359, Dec 1997. 89

[80] B.E.A. Saleh and M.C. Teich. Chapter 3 - beam optics. In *Fundamentals of Photonics (Second Edition)*, Wiley Series in Pure and Applied Optics, pages 74–101. Wiley, second edition edition, 2007. 95

[81] F. L. Pedrotti, L. S. Pedrotti, and L M. Pedrotti. *Introduction to Optics*. Pearson Prentice Hall, New Jersey, 2007. 95